Spyridon Korkos

Ion Beam Shaping of Embedded Metallic Nanoparticles for Photonic Applications

UNIVERSITY OF JYVÄSKYLÄ

FACULTY OF MATHEMATICS
AND SCIENCE

Spyridon Korkos

Ion Beam Shaping of Embedded Metallic Nanoparticles for Photonic Applications

Esitetään Jyväskylän yliopiston matemaattis-luonnontieteellisen tiedekunnan suostumuksella
julkisesti tarkastettavaksi yliopiston Ylistönrinteen auditoriossa FYS1
maaliskuun 31. päivänä 2023 kello 12.

Academic dissertation to be publicly discussed, by permission of
the Faculty of Mathematics and Science of the University of Jyväskylä,
in Ylistönrinne, auditorium FYS1, on March 31, 2023, at 12 o'clock.

JYVÄSKYLÄN YLIOPISTO
UNIVERSITY OF JYVÄSKYLÄ

JYVÄSKYLÄ 2023

Editors
Ilari Maasilta
Department of Physics, University of Jyväskylä
Päivi Vuorio
Open Science Centre, University of Jyväskylä

ABSTRACT

The swift heavy ion irradiation of metallic nanoparticles buried inside a material can result in perfectly aligned nanorods. Within this nanofabrication process, the shape, size, and orientation of the nanoparticles can be controlled in order to tune their optical properties and build nanoscale optical devices. Towards this scope, the metallic nanoparticles and their surrounding material play the most important role. Earlier studies have only shown that initially spherical metallic nanoparticles can transform to nanorods/nanowires, and gold in silica has been the most studied system. This study focused on the impact of matrix material properties and the nanoparticles geometric characteristics on the elongation. For this reason, we used thin Si_3N_4 TEM windows grids as substrates in order to track changes in the same nanoparticle prior and after the irradiation. Except for spherical nanoparticles, nanorods were irradiated as well and different material matrices and deposition techniques were used. By exploiting the differences in SiO_2 properties made by two different deposition techniques, we showed that nanoparticles elongate more while embedded in ALD SiO_2 than in PECVD SiO_2. In addition, the investigation of embedded nanorods in SiO_2 showed that they can be re-oriented to align along the ion beam direction depending on their initial size and ion fluence. The same procedure was followed for spherical nanoparticles embedded in ALD Al_2O_3 resulting in elongated nanoparticles with comparable ratio as in ALD SiO_2. Lastly, the optical characterization of the elongated nanoparticles showed two characteristic localized surface plasmon modes (longitudinal and transverse) confirming the potential use of the nanoparticle/matrix system for photonic applications.

Keywords: swift heavy ion irradiation, TEM windows grids, nanoparticles, SiO_2, Al_2O_3, ALD, PECVD, localized surface plasmon modes.

TIIVISTELMÄ (ABSTRACT IN FINNISH)

Korkos, Spyridon
Upotettujen metalli nanohiukkasten ionisuihku muotoilu fotonisiin sovelluksiin

Säteilytettäessä materiaalin sisään hautautuneita metallisia nanopartikkeleita nopeilla raskasioneilla voidaan synnyttää täydellisesti samansuuntaisia nanosauvoja. Tässä nanovalmistusprosessissa nanopartikkeleiden muodolla, koolla ja suuntauksella voidaan säätää niiden optisia ominaisuuksia, ja näitä rakenteita voidaan hyödyntää nanomittakaavan optisissa laitteissa. Optisia ominaisuuksia räätälöitäessä metalliset nanopartikkelit ja niitä ympäröivä materiaali ovat tärkeimmässä roolissa. Aiemmin on osoitettu, että alun perin pallomaiset metalliset nanopartikkelit voivat muuttua nanosauvoiksi/nanolangoiksi, ja kultananopartikkelit piidioksidissa on ollut tutkituin yhdistelmä.

Tässä tutkimuksessa keskityttiin tutkimaan matriisimateriaalin ominaisuuksien ja nanopartikkeleiden muodon vaikutuksia raskasionipommituksen aiheuttamassa venymisessä. Tästä syystä käytimme ohuita itsekantavia piinitridikalvoja substraatteina, ja seurasimme saman nanopartikkelin muodonmuutoksia ennen ja jälkeen säteilytyksen. Pallomaisten nanopartikkeleiden lisäksi säteilytettiin myös nanosauvoja haudattuina eri materiaalimatriiseihin. Havaitsimme esimerkiksi sen että materiaalin lisäksi myös piidioksidin kasvatusmenetelmä vaikuttaa nanopartikkeleiden venymiseen. Nanosauvat voitiin myös suunnata uudelleen raskasionipommituksen avulla.

Pallomaisten nanopartikkeleiden havaittiin venyvän yhtä paljon atomikerroskasvatettuun alumiinioksidiin haudattuna kuin samalla menetelmällä kasvatettuun piidioksidiin haudattuna. Venyneiden nanorakenteiden optinen karakterisointi paljasti kaksi ominaista pintaplasmonimoodia (pitkittäis- ja poikittaissuuntainen), ja tämän havainnon perusteella näitä rakenteita voidaan periaatteessa hyödyntää fotonisissa sovelluksissa.

Avainsanat: raskasionisäteilytys, nanopartikkelit, SiO_2, Al_2O_3, ALD, PECVD, pintaplasmonit

Author   Spyridon Korkos
                  Department of Physics
                  University of Jyväskylä
                  Finland

Supervisors   Professor Timo Sajavaara
                  Department of Physics
                  University of Jyväskylä
                  Finland

                  University Lecturer Kai Arstila
                  Department of Physics
                  University of Jyväskylä
                  Finland

Reviewers   Professor Patrick Kluth
                  Research School of Physics
                  Australian National University
                  Australia

                  Assistant Professor Richard Wilhelm
                  Institute of Applied Physics
                  TU Wien
                  Austria

Opponent   Professor Daniel Primetzhofer
                  Department of Physics and Astronomy
                  Uppsala University
                  Sweden

PREFACE

The work presented in this thesis has been carried out from 2018 to 2022 at the Department of Physics at the University of Jyväskylä. First of all, I would like to thank my primary supervisor Professor Timo Sajavaara who gave me the opportunity to continue my studies to the doctoral level. Even if he was not interfered much with the experiments performed during this study, his help was valuable editing the publications. Apart from his supervision, I gained a great knowledge from teaching me many about ion beam analysis and especially ToF-ERDA.

Secondly, I would like to thank my second supervisor University lecturer Kai Arstila who introduced and guided me in the field of heavy ion interaction with matter. His mentoring and assistance during the experiments were really important in order to be able myself after he left to continue the research on my own. In addition, I want to thank Dr. Sami Kinnunen who assisted me with the ALD depositions, necessary for my research. Except for our collaboration, we spent really good time having lunch and discussing many things outside academia. I also want to thank the other members of our group Dr Mikko Laitinen, Dr Jaakko Julin, Mr Mikko Kivekas, and Mr Akbar Hossain, with whom we had delightful scientific discussions during group meetings. Furthermore, I would like to thank Dr Kosti Tapio who helped me with the plasmonic characterization during the experiments as well as Associate Professor Jussi Toppari who supervised these experiments and was member of my follow-up group. Lastly, I want to thank laboratory technician Petri Papponen from the Department of Biological and Environmental Sciences for showing me the use of TEM.

I have to acknowledge the Academy of Finland for providing the funding for the NANOIS project (No. 309730). I am thankful to my pre-examiners Professor Patrick Kluth and Associate Professor Richard Wilhelm for their valuable comments about my thesis. I also would like to express my gratitude to Professor Daniel Primetzhofer for accepting to be the opponent in my defense.

Moreover, I would like to thank my collaborators from University of Helsinki: Dr Ville Jantunen who was in charge of the simulations performed during this project and with whom we had many interesting talks how we are going to connect the experimental results with the simulated and advance the research, Dr Aleksi Leino who assisted with the simulations, Professor Flyura Djurabekova and Professor Kai Nordlund, who supervised the project and especially the simulations, and Dr Kenichiro Mizohata who helped with the irradiations performed at Helsinki Accelerator laboratory.

This thesis would be difficult to be accomplished without the support of my Greek friends in Jyväskylä: Myriam, Stratos, Stelios, Natalia, Dimitris, and Aggeliki. I believe that I spent a wonderful time with them trying to forget a little our work and relax, especially during the hard times of pandemia. Finally, it would be impossible to achieve so many things without the support and love of my parents, Aristotelis and Katerina, my sister Maria, and my brother Panagiotis. They always encouraged me to try harder and have confidence in my life.

Jyväskylä, March 2023,

Spyridon Korkos

LIST OF INCLUDED ARTICLES

PI   Spyridon Korkos, Ville Jantunen, Kai Arstila, Timo Sajavaara, Aleksi Leino, Kai Nordlund & Flyura Djurabekova *Nanorod orientation control by swift heavy ion irradiation*. Applied Physics Letters **120** 171602 (2022).

PII   Spyridon Korkos, Kenichiro Mizohata, Sami Kinnunen, Timo Sajavaara & Kai Arstila *Size dependent swift heavy ion induced Au nanoparticle elongation in SiO$_2$ matrix*. Journal of Applied Physics **132** 045901 (2022).

PIII   Spyridon Korkos, Kai Arstila, Kosti Tapio, Sami Kinnunen, J. Jussi Toppari & Timo Sajavaara *Elongation and plasmonic activity of embedded metal nanoparticles following heavy ion irradiation*. RSC Advances **13** 5851-5858 (2023).

Author's contribution

In PI publication, Spyridon Korkos planned and performed most of the experiments, and wrote the experimental part of the original draft, Ville Jantunen planned and performed the simulations, and wrote the simulations part of the original draft, Kai Arstila planned and performed part of the experiments, and supervised the work, Timo Sajavaara supervised the work and edited the manuscript, Aleksi Leino assisted in the simulations and edited the manuscript, Kai Nordlund supervised the work and edited the manuscript, and Flyura Djurabekova supervised the work and edited the manuscript.

In PII publication, Spyridon Korkos planned and performed the experiments, analyzed the experimental results, and wrote the original draft, Kenichiro Mizohata assisted in the irradiations, Sami Kinnunen assisted in the ALD depositions, Timo Sajavaara supervised the work and edited the manuscript, and Kai Arstila planned the experiments, assisted in the irradiations and supervised the work.

In PIII, Spyridon Korkos planned and performed the experiments, analyzed the experimental results, and wrote the original draft, Kai Arstila planned and performed the experiments, Tapio Kosti performed the optical measurements and simulations, analyzed the results, and wrote the relevant part in the original draft, Sami Kinnunen assisted with the ALD depositions and the measuremets with ellipsometer, J. Jussi Toppari edited the manuscript, and Timo Sajavaara supervised the work and edited the manuscript.

LIST OF ACRONYMS

ALD	Atomic Layer Deposition
APTES	(3-aminopropyl)-triethoxysilane
BG	Background
BPP	Bulk Plasmon Polariton
CCD	Charge-Coupled Device
DC	Dark Current
DNG	Double Negative
DPS	Double Positive
EAM	Embedded Atom Model
EELS	Electron Energy Loss Spectroscopy
FDTD	Finite Difference Time Domain
FIB	Focused Ion Beam
GFIS	Gas Field Ion Source
GPC	Growth Per Cycle
HIM	Helium Ion Microscopy
iTS	inelastic Thermal Spike
LED	Light-Emmitting Diode
LSP	Localized Surface Plasmon
LSPR	Localized Surface Plasmon Resonance
MD	Molecular Dynamics
NA	Numerical Aperture
PECVD	Plasma-Enhanced Chemical Vapor Deposition
RF	Radio Frequency
R.I.	Refractive Index
RIE	Reactive Ion Etching
SEM	Scanning Electron Microscopy
SNG	Single Negative
SNOM	Scanning Near-field Optical Microscopy
SPP	Surface Plasmon Polariton
TEM	Transmission Electron Microscopy
TMA	trimethylaluminium
ToF-ERDA	Time-of-Flight Elastic Recoil Detection Analysis

XRR X-ray Reflectivity

ZBL Ziegler-Biersack-Littmark

CONTENTS

1 INTRODUCTION

In the field of nanotechnology, the increasing need for producing nanostrutures with complex shapes, which is difficult with standard nanofabrication techniques (colloidal chemistry, electron beam lithography, ion implantation), led to the search for new experimental techniques. The discovery that highly energetic ions can modify the shape of metallic nanoparticles inside amorphous matrices [1] attracted great attention towards this direction [2–12]. According to this research, the passage of "swift heavy" ions (≥ 1 MeV/u) through spherical metallic nanoparticles embedded in amorphous materials caused their transformation to perfectly aligned nanorods along the ion beam direction.

The basic mechanism behind this phenomenon, which is still under debate, is that the "swift heavy" ions make the surrounding matrix above, below and around the nanoparticle underdense [13–16] and at the same picosecond timescale, the nanoparticle melts. The combination of these two effects makes the molten metal flow into the underdense matrix resulting in the elongation. This process has been called ion beam shaping.

Ion beam shaping has been mainly applied to spherical metallic nanoparticles, of different elements, embedded in dielectric materials, such as amorphous SiO_2, amorphous Si_3N_4 and sapphire (crystalline Al_2O_3). The experiments are complemented by Molecular Dynamics (MD) simulations [14] of the irradiated nanoparticle-matrix system as it is essential to understand better the mechanism behind this phenomenon. In the MD studies of elongation, the energy deposition from the ions to the matrix is modelled with inelastic thermal spike (iTS) model [17]. Except for energies divided by atomic mass close or bigger than 1 MeV/u, the elongation to occur requires electronic stopping force bigger than 2 keV/nm [6]. Generally, the degree of elongation depends on the irradiation conditions such as ion type and energy loss, flux [5], and fluence.

Nowadays, the research aims to the irradiation of different nanostructures shapes, in addition to nanospheres, in order to create new nanostructures morphologies. Such nanostructures, including nanorods, nanoplatelets, and nanotriangles, can be produced either via chemical methods or via nanolithography techniques, like electron beam lithography and direct ion milling. Moreover, the

fabrication of the matrix in which nanostructures are embedded is an important step. Due to the matrix underdensification requirement, the matrix material properties should play a key role during the irradiation process. Mainly, Plasma-Enhanced Chemical Vapor Deposition (PECVD), thermal growth and sputtering have been applied, but there has not been direct comparison about the impact of different deposition techniques on the ion beam shaping. Atomic layer deposition (ALD) [18, 19] can be an alternative technique to produce films with high quality (uniform and conformal) and precise thickness. So, it is worth to investigate the difference in ion beam shaping arising from the deposition technique of the matrix. ALD, as well, allows to deposit films that have not been yet used in connection with ion beam shaping, such as amorphous Al_2O_3, TiO_2 and ZnO.

To gain deeper understanding, ion beam shaping is a process that should be followed in every step: samples fabrication, imaging of the nanostructures before the irradiation, samples irradiation and imaging of the nanostructures after the irradiation. The only available imaging technique for nanostructures embedded inside a material is Transmission Electron Microscopy (TEM). This has been mainly achieved by preparing the samples in cross-sectional geometry by Focused Ion beam (FIB) technique, called TEM-lamella. The disadvantage of this technique is that it is basically impossible to image the same nanostructure before and after the irradiation. This is a problem when the nanostructures are not well separated between each other. Then assumptions need to be made if an elongated nanostructure comes from a single one or several particles merged together. This fact implied the use of thin Si_3N_4 TEM windows grids as substrate. By means of this approach, nanostructures of different size and shape can be fabricated on the same sample and can be identified after the irradiation.

Moreover, it is well known that the embedded metallic nanostructures exhibit the so-called localized surface plasmon (LSP) modes which are considered as collective oscillation of metal's conduction electrons confined within the volume of the nanostructure. These modes have resonance frequency (LSPR) showing up a strong scattering and absorption peak [20]. Additionally, at the resonance, the electric field near the nanostructure is enhanced by the near-field of the plasmonic excitation. Generally, the LSPR frequency depends strongly on the material, the shape of the nanostructures, and the surrounding material. Noble metals, like gold and silver, have significant plasmonic activity [21]. The shape affects the distribution of the electric near fields, yielding the highest confinement and the enhancement at the sharpest corners of the nanostructures. As a result, the elongated nanostructures can act as "nanoantennas".

In this study, firstly, I confirmed the elongation of gold spherical nanoparticles embedded in SiO_2 using thin Si_3N_4 TEM windows grids as a substrate and made a comparison between nanoparticles embedded in PECVD SiO_2 and ALD SiO_2. Next, samples with gold nanorods made either by chemical methods or by direct neon milling and embedded inside SiO_2 were irradiated and the irradiation effects on nanorods were investigated. The same procedures were extended, as well, to gold and silver nanoparticles embedded in other materials, such as amorphous ALD Al_2O_3 and amorphous ALD TiO_2. The experimental

results were accompanied with simulations in order to explain theoretically the irradiation effects on embedded nanostructures.

Finally, the plasmonic characterization of the irradiated nanostructures was done with dark field scattering microscopic spectroscopy. Placing the end of an optical fiber on a dark field image plane of the microscope is a way to guide the light only from a chosen area to the spectrometer. By this optical fiber coupling, spectra of individual nanostructures can be characterized.

2 RADIATION INTERACTION WITH MATTER

Radiation interaction with matter is a wide field in physics which includes many phenomena. These phenomena can vary depending on charge, type, and energy of the particles which interact with matter [22]. If particles have charge (electrons, ions) or not (neutrons, photons) affects greatly how an incoming particle interacts with the target material. In the first kind, the charged particles interact through the Coulomb force with the particles present in any medium through which they pass. In the second kind, for instance photons travel through matter until they undergo a catastrophic interaction with a single collision. In all cases, the interaction refers to whole or partial transfer of energy of the incident radiation to electrons or nuclei of atoms inside a material, or to charged particle products of nuclear reactions.

When charged particles penetrate through the matter, they lose energy. It is described by the stopping force given by equation (1):

$$S = -dE/dx, \tag{1}$$

which gives the energy transfer per pathlength of a particle along its trajectory. The nature of interaction between the particle and the target can be divided into electronic stopping, which originates from the excitation and ionization of the target electrons, and nuclear stopping which originates from the atomic collisions with the target atom nuclei. In addition, there can be nuclear reactions between the projectile particle and target atoms. The distance that a particle travels through the material until it stops, which is called range, can reveal information about the interaction. Since energy loss is a statistical process, there is an energy distribution of the charged particles. The width of this energy distribution is a measure of energy straggling. The same occurs for the range since charged particles are also subject to range straggling, defined as the fluctuation in pathlength for individual particles of the same initial energy.

On the other hand, when photons interact with matter, there is no incremental energy loss, but attenuation of the beam of particles. Attenuation is an exponential function of the path length through the medium. Each particle is individually removed from the incoming beam by the interaction. If N_o particles

were initially hitting the target material, then after penetrating some distance x inside the material, the number of particles in the beam are reduced to:

$$N(x) = N_0 e^{-\mu x}. \tag{2}$$

The quantity μ is known as the linear attenuation coefficient which measures how rapidly the initial particles are removed from the beam.

In the next paragraphs, there will be more analytical description of ion, photon, and electron interaction with matter. In each case, emphasis will be given to phenomena relevant to this study.

2.1 Ion interaction with matter

When an ion penetrates the matter, it interacts mainly either with the electrons or the nuclei of the target atoms. Also, nuclear reactions from the interaction of the projectile ion and target atoms may occur when the ions have sufficient energy to overcome the Coulomb barrier. At the low energy regime (<1 MeV for heavy ions), the ions mainly interact with the nuclei of target atoms via elastic collisions. As a result, nuclear energy losses are dominant in this energy range. Two processes take advantage of these interactions in order to be held: ion implantation and surface sputtering. In the first one, the incident ions penetrate and remain inside the target normally near the surface, while in the second, the ions knock out the atoms from the surface of the target.

The behaviour of the collided particles can be described in terms of elastic scattering between two particles. According to the laws of conversation of energy and momentum, and assuming that the target atom is stationary, following equations are valid:

$$E_o = \frac{1}{2}M_1 u_0^2 = \frac{1}{2}M_1 u_1^2 + \frac{1}{2}M_2 u_2^2, \tag{3}$$

$$M_1 u_0 = M_1 u_1 cos\phi + M_2 u_2 cos\theta, \tag{4}$$

$$0 = M_1 u_1 sin\phi - M_2 u_2 sin\theta, \tag{5}$$

where M_1 and M_2 are masses of the incident and the target particles, u_0 is the velocity of the initial projectile particle, u_1 and u_2 are the velocities of the scattered incident particle and the recoiled target particle, respectively, and ϕ and θ their corresponding scattering angles (Figure 1).

The energies of the scattered projectile particle and the recoiled target particle can be deduced from the previous equations as E_1 and E_2, respectively. They are connected with the initial energy via the kinematic factors K and Λ:

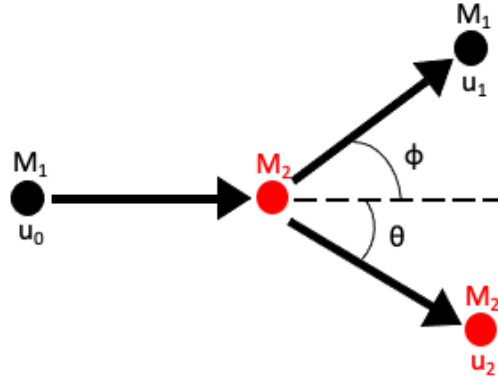$$E_1 = KE_0 = \frac{M_1 cos\phi \pm \sqrt{M_2^2 - M_1^2 sin^2\phi}}{M_1 + M_2} E_0, \tag{6}$$

FIGURE 1   Classical two particles scattering process.

$$E_2 = \Lambda E_0 = \frac{4M_1 M_2 cos^2\theta}{(M_1 + M_2)^2} E_0. \tag{7}$$

Even for energies much higher than 1 MeV, the incident ion projectile keeps interacting via elastic collisions with the target atoms resulting in the scattering of the two colliding particles. However, at such high energies, the ions mainly interact inelastically with the electrons in the target material and the electronic energy loss dominates.

In case that their energy divided by the mass of their atomic nucleus is close to or higher than 1 MeV/u and they are carbon or heavier, the projectile ions continue to interact with the electrons of the target atoms inelastically and are referred as swift heavy ions (SHI). Ion tracks are formed in the material as the residual damage along the ion trajectory. As the swift heavy ion penetrates the material, it interacts with valence and core electrons knocking them out from the atoms. These electrons have high kinetic energy (in the range of keV) and are known as delta electrons. The delta electrons can ionize further the atoms along the path of the ion. As a result, the ongoing collisions produce more high energy electrons (electron collision cascade) leaving holes in inner shells of the atoms (Auger transition). The movement of the energetic electrons creates a charge region along the ion path with inner region populated by valence band holes and energetic electrons in the outer region [23, 24].

Subsequently, the energetic electrons transfer energy to the lattice by electron-phonon coupling leading to a rapid increase in temperature within a few nm of the ion trajectory and exceeding the melting temperature of the material (thermal expansion), which depends on the ion mass, energy, and the material. This process is called a thermal spike [17]. After cooling down the material, a trail is left as a result of local structural modification, the so called ion track, having a cylindrical shape. This process happens really fast, at a picosecond timescale. The evolution of thermal spikes depends strongly on lattice and electron specific heat and the electron-phonon coupling strength. In particular, the ion track can be consisted of an underdense core surrounded by an overdense shell in a few amorphous materials, such as SiO_2 [13], Si_3N_4 [25], and Al_2O_3 [26], which core-shell structure depends strongly on the ion mass and energy as well.

The formation of the ion track with underdense core surrounding by an

overdense shell inside a material by SHI irradiation (Figure 2) leads to the question what will happen when nanoparticles are embedded into this host matrix. The passage of the energetic ion creates an ion track above, below, and around the NP [14]. When the energy is transferred to the electrons of the nanoparticle, the energy diffuses rapidly outward to the surface. As the energy reaches the metal/matrix boundary and is transferred to the electrons of the surrounding matrix, the temperature increases at the boundary due to the stronger electron-phonon coupling of the surrounding dielectric matrix. However, the surrounding matrix prevents the energy diffusion because of the lower thermal conductivity. Consequently, the electronic energy is transformed to heat and diffuses back towards the center of the nanoparticle resulting in full or partial melting [7, 15, 16]. Finally, the molten metal flows into the track resulting in elongation after cooling and recrystallization. This process is called ion beam shaping.
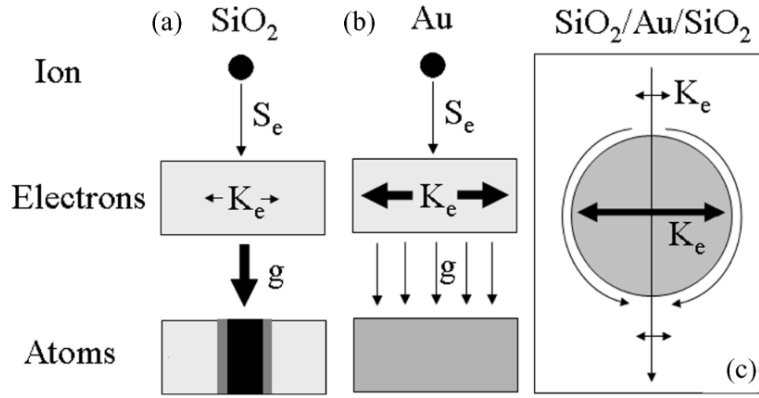

FIGURE 2   Schematic representation for SHI interaction for (a) bulk silica, (b) bulk gold, and (c) gold NPs confined within a SiO_2 matrix. Reprinted with permission from [7], Copyright 2012, American Physical Society.

2.1.1 Ion beam shaping: From simulations to experiments

A tremendous work has been implied to the understanding of the ion beam shaping process and simulations techniques have had significant contribution. The combination of inelastic Thermal Spike (iTS) model [27, 28] with Molecular Dynamics (MD) has been accepted as the most efficient approach to study the mechanism. The iTS model refers to the interaction between the electronic and atomic subsystem of a material after the passage of the ion. These interactions are described by two coupled heat diffusion equations, one for the electrons (e) and one for the atomic lattice (a):

$$C_e \frac{\partial T_e}{\partial t} = \nabla(k_e \nabla T_e) - G(T_e - T_a) + A(r_\perp(v)) \tag{8}$$

$$C_a \frac{\partial T_a}{\partial t} = \nabla(k_a \nabla T_a) + G(T_e - T_a), \tag{9}$$

where C_e, C_a are the heat capacities, k_e, k_a the heat conductivities and T_e, T_a the temperatures of the electronic and atomic subsystems, respectively, G_e the electron-phonon coupling strength, and $A(r_\perp(v))$ the initial temperature distribution of energy after heating. The electron-phonon coupling strength can be calculated by the equation

$$G_e = \frac{k_e(T_e)}{\lambda^2}, \tag{10}$$

where λ is the electron mean free path. The initial temperature distribution of energy have been proposed from Waligorski et al [29] as a function of the electronic energy loss. By solving these two equations, ion track diameter can be defined by the molten cylindrical region, where the lattice exceeds the melting point of the material. In the case where metallic nanoparticles are embedded inside the matrix, then the same coupled heat equations are applied. In total four equations should be solved in order to simulate the evolution of the embedded nanoparticle under the SHI irradiation.

Molecular Dynamics is referred to the motion of the atoms because of the acting force by their neighbors. This acting force is written as

$$F_i = m_i a_i = -\nabla V(r_i), \tag{11}$$

where m_i and a_i are the mass and acceleration of each atom, and V the potential energy. The potential energy or otherwise interatomic potential is the most important parameter during calculations. Depending on the different species of atoms interacting with each other, different approaches can be applied, including Watanabe-Samela [30, 31], embedded atom model (EAM) [32, 33], and Ziegler-Biersack-Littmark (ZBL) [34]. In order to combine iTS calculations with MD, we should find a way to redistribute the energy from the ion impacts to the atoms as kinetic energy. This is achieved by introducing a cylinder (with diameter left as a free parameter or equal to the corresponding experimental track diameter) through which the atoms obtain the kinetic energy [35, 36]. After energy deposition, Berendsen thermostat [37] should be applied in order to dampen the oscillations from pressure wave and to emulate cooling provided by bulk material.

In order to simulate the nanoparticle-matrix system [38], a box of FCC metal (typically Au) is created from which the desired nanoparticle shape (sphere, rod, disk, etc) is cut. Then, a cell of the amorphous matrix (typically SiO_2) is generated from which a cavity is cut with the shape of initial nanoparticle but slightly bigger (1%). The nanoparticle is compressed by 2% and is fit inside the void. After relaxation, the nanoparticle will expand to the empty space. In Figure 3, a representation for simulation cell and the evolution of gold nanosphere in silica after SHI irradiation are shown.

However, the simulations, so far, do not consider the energy barrier between the conduction bands of the metal nanoparticle and the surrounding matrix (typically 4.1 eV for gold-silica system) as the electrons of the metal need to overcome the barrier to transfer the energy to the electrons of the surrounding matrix.
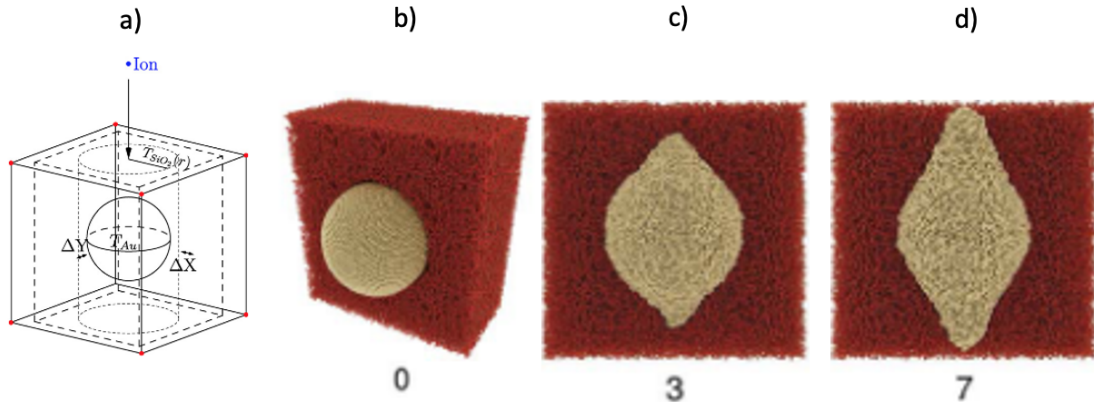
FIGURE 3 (a) Schematic representation of the simulation cell for gold nanosphere embedded in amorphous SiO_2 [39] and (b),(c) and (d) evolution of the elongation of gold nanosphere (12 nm diameter) in SiO_2 after 0 impacts, 3 impacts and 7 impacts respectively. Reproduced from [14] under the license CC BY 3.0.

A recent study [40] showed that the interface between the gold (metal) and silica (insulator) affects the melting of the nanoparticles and the elongation process.

The experimental results differ from the simulations regarding the amount of ion dose needed to observe the elongation. For example, in simulations, a spherical nanoparticle of 10–20 nm diameter embedded in SiO_2 needs less than 10 impacts in order to show clear elongation [14]. But in experiments, the same nanoparticle needs more than 50 ion impacts (10^{13} ions/cm^2 fluence) in order to start showing clear elongation along the ion beam. Another limitation is that MD simulations of nanoparticles bigger than 20 nm diameter take a lot of time so smaller nanoparticles are preferred in comparison with experiments.

Even if there are many studies about SHI irradiation in materials, including SiO_2 [13, 41], Si_3N_4 [25, 42], Al_2O_3 [26, 43], TiO_2 [44, 45], ZnO [46, 47], etc., ion beam shaping has been governed by metallic (Au, Ag, Pt, Co, Zn, etc.) spherical nanoparticles embedded in amorphous SiO_2 [1, 3–5, 7, 10, 11, 48], amorphous Si_3N_4 [11, 49, 50], sapphire (crystalline Al_2O_3) [51, 52], crystalline indium tin oxide ($In_xSn_{1-x}O_z$-ITO) [12], and lithium niobate $LiNbO_3$ [53]. The ion track diameter denotes whether a nanoparticle of specific size can elongate or not. Typically, nanoparticles with diameter less than the ion track diameter do not elongate or elongate at a significantly lower rate than the bigger ones. This limitation applies also to the minimum width that an elongated nanoparticle can reach so that there is a saturation in elongation when the width is close to the track diameter [54]. The ion track diameter limits also the maximum applied fluence after which no more elongation can occur. This maximum fluence depends as well on the nanoparticle size, ion species, and energy [6].

Furthermore, the nanoparticles threshold diameter for elongation and the minimum elongation width are affected secondarily by the energy density per atom required for vaporization of the metal [55]. This energy density varies between different metals resulting basically in smaller threshold diameters for metals with higher melting points. Consequently, the elongation process depends

on the metallic species as well.

According to Rizza et al [7], the result of SHI irradiation of embedded gold spherical nanoparticles in silica differs with size. Nanoparticles with diameters less than 10 nm vaporize during irradiation and remain spherical, nanoparticles from 10 to 30 nm completely melt and transform to nanorods and nanowires, nanoparticles from 30 to 70 nm partially melt and obtain a facetted shape and bigger nanoparticles do not deform at all (Figure 4). The extent of each area depends on the irradiation conditions and nanoparticle-silica system composition.
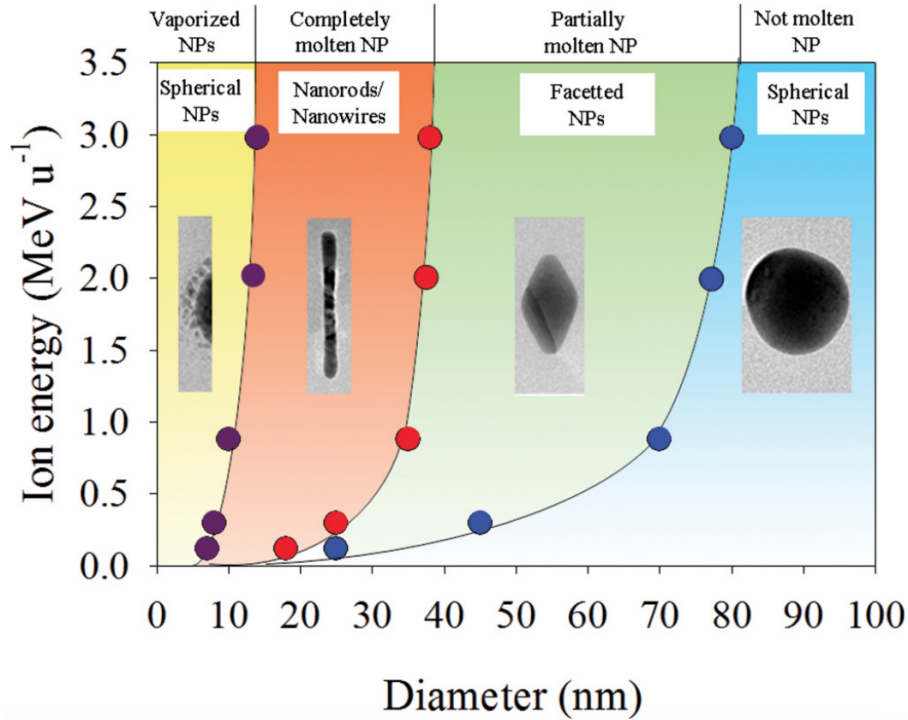

FIGURE 4 Diagram of evolution of gold spherical nanoparticles under SHI irradiation with the ion energy. Reprinted with permission from [7], Copyright 2012, American Physical Society.

According to Mota-Santiago et al [56], SiO_2 favors bigger elongation compared to Si_3N_4 (Figure 5). The main reason is that SiO_2 has bigger electron-phonon coupling strength in conjunction with the lower thermal conductivity allowing the nanoparticle to reach bigger temperature and completely melt. On the other hand, Si_3N_4 cannot reach this temperature because of lower electron-phonon coupling and higher thermal conductivity, and partially melts. This fact justifies also the reason why the nanoparticles in the interface between these two materials have a preferential elongation towards SiO_2 [56].
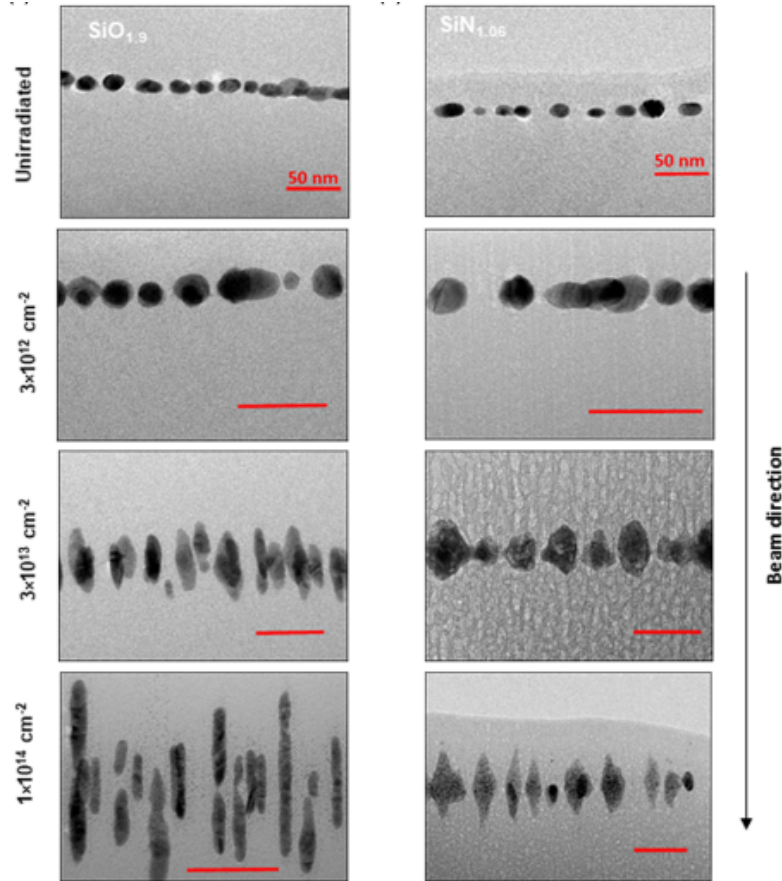
FIGURE 5   TEM images of gold nanoparticles embedded in SiO_2 and Si_3N_4 before and after SHI irradiation. Reproduced from [56] under the license CC BY 4.0.

2.2   Photon interaction with matter: Plasmons

In the category of uncharged particles interacting with matter, photons are the most characteristic case. Generally, when an energetic photon interacts with atoms or atomic electrons in matter, there is a change in its initial energy or its direction, because of scattering, including three interaction mechanisms: the photoelectric effect, the Compton scattering and the pair production. However, when the interest is focused on the interaction of photons (light) with bulk metallic structures, other phenomena take place.

When an electromagnetic wave propagates through a linear and isotropic medium, the propagation of light depends on the electric permittivity ϵ and magnetic permeability μ of the material. The materials are classified to four categories based on whether these two values are positive or negative (Table 1).

Since the interest is focused on the light propagation through nanoparticles surrounded by dielectric materials, surface waves at the boundary between two media have a major importance. In the case of a DPS-SNG boundary where both media have positive magnetic permeability, but one has positive electric permittivity and the other negative, a surface wave can propagate along the boundary being evanescent on both sides of it [57]. Taking the case of a transverse magnetic

24

TABLE 1   Categories of media based on their permittivity and permeability

Type	ϵ	μ
Double Positive(DPS)	+	+
Double Negative(DNG)	-	-
Single Negative(SNG)	+	-
Single Negative(SNG)	-	+

(TM) wave, where the magnetic field is parallel to the boundary and the electric field orthogonal to the direction of propagation, the three field components H_x, E_y and E_z are functions of $e^{-\gamma_1 y}e^{-j\beta z}$ and $e^{+\gamma_2 y}e^{-j\beta z}$ for the two different media respectively (β is the common propagation constant, and γ_1 and γ_2 the extinction coefficients for the two corresponding media). By solving the Helmholtz equation $\nabla^2 U + \beta^2 U = 0$:

$$-\gamma_1{}^2 + \beta^2 = \omega^2 \mu \epsilon_1 \tag{12}$$

$$-\gamma_2{}^2 + \beta^2 = \omega^2 \mu \epsilon_2. \tag{13}$$

The condition that E_z must be continuous to the boundary, it leads to:

$$\frac{-\gamma_1}{\epsilon_1} = \frac{\gamma_2}{\epsilon_2} \tag{14}$$

Also, the condition that $D_y = \epsilon E_y$ should be continuous is satisfied by Maxwell's equation. This fact in combination with the change of the sign of ϵ at the boundary means that E_y should also reverse sign at the boundary. As a result, a surface electric charge in the form of a charge-density longitudinal wave, that oscillates at frequency ω, is created (Figure 6). The optical wave and this charge-density wave form the surface plasmon polariton (SPP). Essential requirement for a SPP wave to exist is that $-\epsilon_2 > \epsilon_1$.
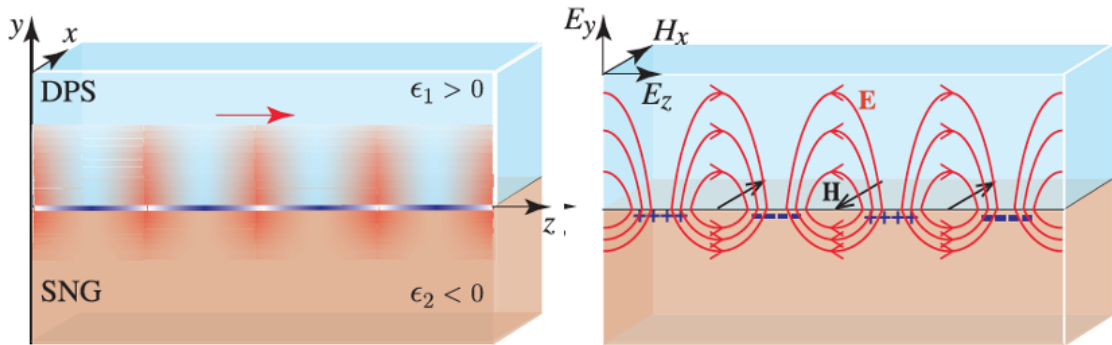

FIGURE 6   Schematic representation of a surface plasmon polariton (SPP) created between a double positive (DPS) and a single negative (SNG) medium. Reprinted with permission from [57], Copyright 2019, John Wiley and Sons.

Regarding the optical properties of linear conductive materials like metals, conductivity σ relates the electric current density J with the electric field E, $J = \sigma E$.

When this relation is dynamic, the conductivity is frequency-dependent and the conduction electrons behave as individual particles moving between scattering events. This is called Drude model and the conductivity has the form:

$$\sigma = \frac{\sigma_0}{1 + j\omega\tau},$$ (15)

where σ_0 is the low frequency conductivity and τ is the scattering time. The corresponding relative effective permittivity of the medium is given by the equation:

$$\frac{\epsilon_c}{\epsilon_0} = 1 + \frac{\omega_p^2}{-\omega^2 + j\omega\zeta},$$ (16)

where $\zeta = 1/\tau$ and $\omega_p = \sqrt{\epsilon_0/\omega\tau}$ the plasma frequency. In the case of frequencies $\omega \gg \zeta$, simplified Drude model is followed. The effective permittivity and the corresponding propagation constant (dispersion relation) are:

$$\frac{\epsilon_c}{\epsilon_0} = 1 - \frac{\omega_p^2}{\omega^2},$$ (17)

$$\beta = nk_0 = \frac{\omega}{c_0}\sqrt{\frac{\epsilon_c}{\epsilon_0}} = \frac{\omega}{c_0}\sqrt{1 - \frac{\omega_p^2}{\omega^2}},$$ (18)

where n is the refractive index of the material, k_0 is the propagation constant in vacuum, and c_0 is the speed of light in vacuum. At frequencies below the plasma frequency, the effective permittivity is negative which makes the metal behave as SNG. As a result, the free electrons of the metal undergo collective oscillations, called plasmons, which are the quanta of the plasma waves. At frequencies greater than plasma frequency, the permittivity is positive so that the waves that travel through the metal are called bulk plasmon polaritons (BPPs).

Therefore, when a metal behaves as an SNG material below plasma frequency, the boundary between a DPS dielectric material can support SPP wave. The effective permittivity of the metal-dielectric boundary is given as:

$$\epsilon_b = \epsilon_1 \frac{1 - \omega^2/\omega_p^2}{1 - \omega^2/\omega_s^2},$$ (19)

where $\omega_s = \omega_p/\sqrt{1 + \epsilon_1/\epsilon_0}$. When $\omega < \omega_s$, the metal is SNG material and $-\epsilon_2 > \epsilon_1$, so the SPP wave propagates along the boundary. But, when $\omega_s < \omega < \omega_p$, SPP wave does not exist any more because $-\epsilon_2 < \epsilon_1$ and bulk waves are propagating. Finally, when $\omega > \omega_p$, the metal is a DPS medium and BPPs are propagating.

This theory can be extended to metal nanostructures of subwavelength dimensions (from hundreds of nm to a few nm) when they are surrounded by dielectric materials. These nanostructures can have different shapes (nanospheres, nanorods, nanodisks) and their plasmon polaritons are distinguished from the bulk metals as localized surface plasmon polaritons or simplified localized surface plasmons (LSPs). Generally, the nanostructures exhibiting plasmonic activity

are characterized by their localized surface plasmon resonance (LSPR) frequency when the exciting frequency matches their resonance frequency.

The most characteristic case is a metallic nanosphere surrounded by a dielectric material. When a plane wave with electric field E_0 is propagating through the nanosphere, it produces a parallel internal field E_i. This internal field creates an oscillating electric dipole which emits a scattered dipole wave E_s. Along with the scattering, the metals can exhibit absorption as well. The strengths of scattering and absorption are characterized by their cross-sections σ_{sca} and σ_{abs}, respectively, which depend on the polarizability of the sphere α. When the radius of the nanosphere is a lot smaller than the wavelength of the incident light ($a<<\lambda$), the polarizability of the nanosphere can be calculated by the quasi-static approximation:

$$\alpha = \frac{4\pi a^3(\epsilon_s - \epsilon)}{2\epsilon_s + \epsilon},$$ (20)

where ϵ_s is the permittivity of the metal and ϵ is the permittivity of the surrounding dielectric. According to Mie/Maxwel-Garnett (MG) theory [58], absorption and scattering cross-sections can be calculated for nanoparticles inside dielectrics:

$$\sigma_{sca} = \frac{k^4|\alpha|^2}{6\pi} = \frac{8\pi k^4 a^6}{3}|\frac{\epsilon_s - \epsilon}{\epsilon_s + 2\epsilon}|^2,$$ (21)

$$\sigma_{abs} = kIm[\alpha] = 4\pi ka^3 Im[\frac{\epsilon_s - \epsilon}{\epsilon_s + 2\epsilon}],$$ (22)

where $k=2\pi/\lambda$. The relation between the internal and the incident electric field is given by the equation:

$$E_i = \frac{3\epsilon}{\epsilon_s + 2\epsilon}E_0$$ (23)

meaning that they are proportional to each other. Resonance occurs when $\epsilon_s=2\epsilon$ and the resonance frequency is:

$$\omega_0 = \frac{\omega_p}{\sqrt{1 + 2\epsilon}}.$$ (24)

In Figure 7, the field lines for a sphere embedded in dielectric matrix and the scattering and absorption spectra for Au nanospheres in water are shown. The peak corresponds to the LSP dipolar mode of a gold spherical nanoparticle in water.

Additionally, this theory can be expanded to other nanoparticle shapes. The difference in optical properties between different nanostructures arise from the value of polarizability which depends strongly on the shape, the dimensions of each particle, and the permittivities of the metal, from which the nanostructure is consisted of, and the surrounding dielectric material. The case of a gold nanoellipsoid embedded in silica is characteristic. The ellipsoid has three major axes
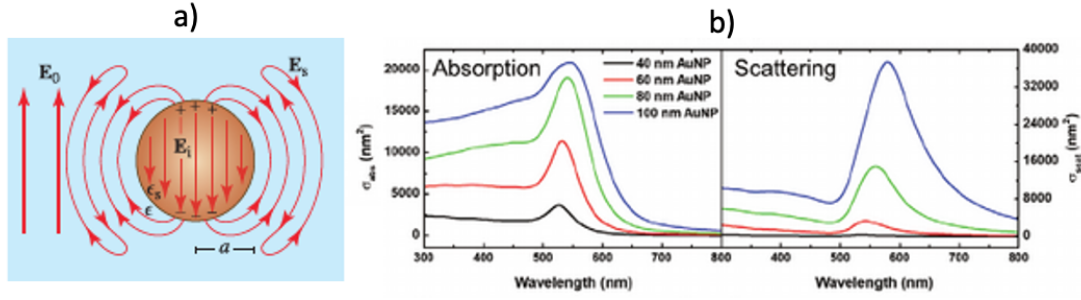
FIGURE 7 (a)Field lines for a sphere embedded in dielectric matrix. Reprinted with permission from [57], Copyright 2019, John Wiley and Sons. (b) Scattering and absorption spectra for Au spherical nanoparticles of various diameters in water. Reprinted with permission from [59], Copyright 2020, John Wiley and Sons.

(a, b, c), where a axis is the long axis and b, c are the shorter axes. For simplicity, short axes are equal to each other. The polarizability α of an ellipsoid can be calculated as:

$$\alpha_i = \frac{4\pi\epsilon_0\epsilon ab^2(\epsilon_s - \epsilon)}{3[\epsilon + A_i(\epsilon_s - \epsilon)]},$$ (25)

where A_i refers to the long and short axis so that:

$$A_{long} = \frac{1 - E^2}{E^2}[\frac{1}{2E}ln(\frac{1 + E}{1 - E} - 1)], A_{short} = \frac{1 - A_{long}}{2}, E^2 = 1 - \frac{b^2}{a^2}.$$ (26)

The extinction spectrum reveals two resonance peaks which correspond to the longitudinal and to the transverse plasmon mode. The longitudinal mode is parallel to the long-axis and is localized to the poles of the ellipsoid. The transverse mode is parallel to the short-axis and is localized at the equatorial region of the ellipsoid. Comparing with a gold nanosphere embedded in silica, the resonance condition has been modified because of the change in the shape, resulting in the longitudinal and transverse plasmon modes which are shifted with respect to the LSPR frequency of the spherical nanoparticle (Figure 8).
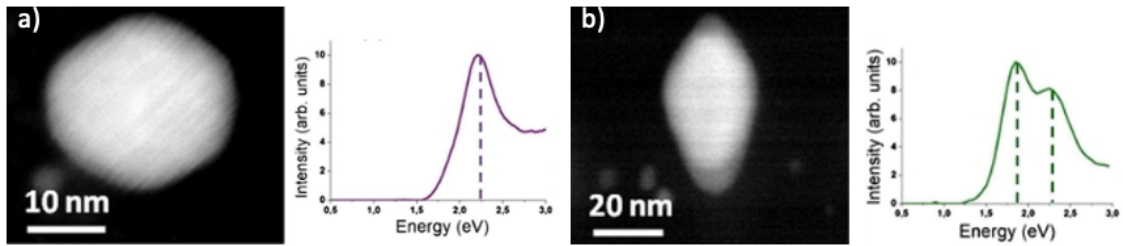
FIGURE 8   (a)Electron Energy Loss spectroscopy (EELS) for (a) a spherical gold nanoparticle embedded in silica which exhibits LSPR at 2.22 eV and (b) an ellipsoid gold nanoparticle embedded in silica which exhibits longitudinal LSPR at 1.90 eV and transverse LSPR at 2.33 eV. Reprinted with permission from [60], Copyright 2018, American Physical Society.

2.3 Electron interaction with matter

When an electron hits onto a material, different interactions can occur (Figure 9). These interactions are categorized to elastic and inelastic interactions. During elastic interactions, the electrons do not lose energy almost at all. Such electrons either travels through the sample without interacting with that or are elastically scattered. These direct electrons are used for imaging at Transmission Electron Microscopy (TEM). Elastic scattering occurs when the electron is deflected from its path by Coulomb interaction with the positive potential inside the electron cloud of the target atom losing only a negligible amount of energy.
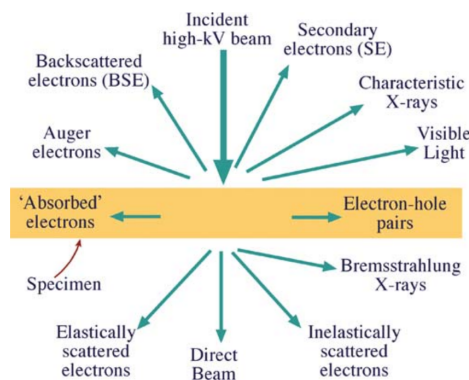

FIGURE 9   Signals generated when a high-energy beam of electrons interacts with a thin specimen. Reprinted with permission from [61], Copyright 2009, Springer Nature.

During inelastic interactions, energy is transferred from the incident electrons to the sample losing energy. This causes the generation of different signals including secondary electrons and Auger electrons by inner-shell ionization. The secondary electrons can be produced when electrons from conduction or valence band can gain enough energy from their interaction with the incoming electrons

to be ejected in vacuum. These electrons can be used to form images of morphology and surface topography from the specimen in Scanning Electron Microscopy (SEM).

3 EXPERIMENTAL TECHNIQUES

3.1 Thin film deposition and etching

3.1.1 Plasma-Enhanced Chemical Vapor Deposition (PECVD)

Plasma-Enhanced Chemical Vapor Deposition (PECVD) is a technique of depositing thin films on a substrate [62]. The deposited film is a result of two reacting gases in plasma state on top of a substrate. A radio frequency (RF) discharge is used to ionize the precursor gases between two electrodes before the reaction and generate the plasma. It consists of an RF driven top electrode and a heated grounded bottom electrode. The substrate is placed on top of the bottom electrode inside a chamber (Figure 10). After the deposition of the film is terminated, a noble gas (usually N_2) is inserted aiming to remove the byproducts of the reactions from the surface of the film. In the present study, a Plasmalab80Plus PECVD (Oxford Instruments) system was used.
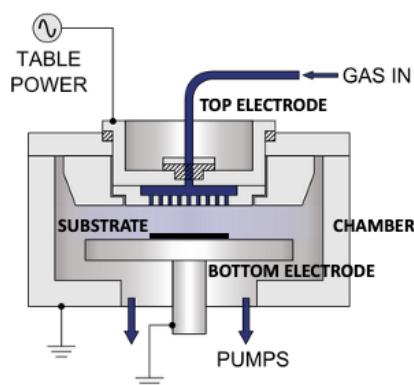

FIGURE 10   PECVD reactor schematic [63].

3.1.2 Atomic Layer Deposition (ALD)

Atomic Layer Deposition (ALD) technique is an effective method of producing films of high quality (uniform and conformal) and precision in thickness [64]. A typical ALD set-up consists of a reactor chamber where the substrate is placed, and the molecules from the precursors are inserted in order to react in the surface of the substrate (Figure 11).
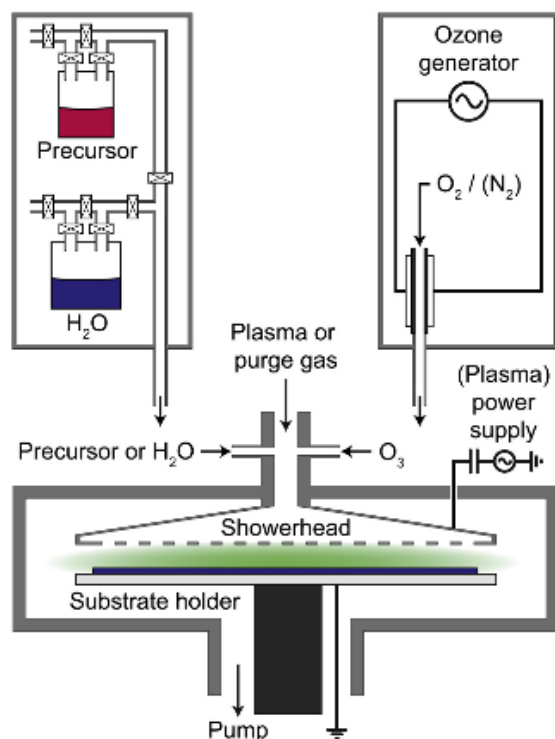

FIGURE 11   ALD reactor configuration equipped with thermal and energy-enhanced ALD capabilities. Reprinted with permission from [65], Copyright 2013, Elsevier.

The deposition process is complete after sequent cycles and in the case of two precursors each of them normally has four steps (Figure 12). The first step includes the exposure of the substrate to the pulse of the first precursor and the reaction with the surface molecules. The second step includes the removal of the non-reacted molecules of the precursor and the reaction byproducts by inserting noble gas (mainly N_2). In the the third step, the molecules from the second precursor are inserted to react with the molecules of the first precursor in the surface of the substrate. Finally, in the forth step, the reaction byproducts and the non-reacted molecules of the second precursors are removed after noble gas flow. By this way, in every cycle, an atomic layer of a few Å is created and the desired thickness is achieved after repeated cycles.

Each deposition is characterized by the growth rate of the film per cycle (GPC) which is given in nm or Å. The GPC depends on the deposition temperature, the material substrate, and the precursors. The basic disadvantage of this

method is that the growth rate of the films is very slow comparing to other deposition methods. For example, the growth rate of a film deposited by PECVD is in the range of tens of nanometers per minute, but ALD deposit films with a rate of a few nm per minute. Depending on the origin of the necessary energy for the surface reactions, ALD is divided to thermal and energy-enhanced ALD. In thermal ALD, the energy is supplied by heating the ALD chamber and the substrate. This kind of ALD was applied in the present study by using a Beneq TFS 200 cross flow reactor. Energy-enhanced ALD includes the cases where the energy is provided by other forms than heat, such as plasma.
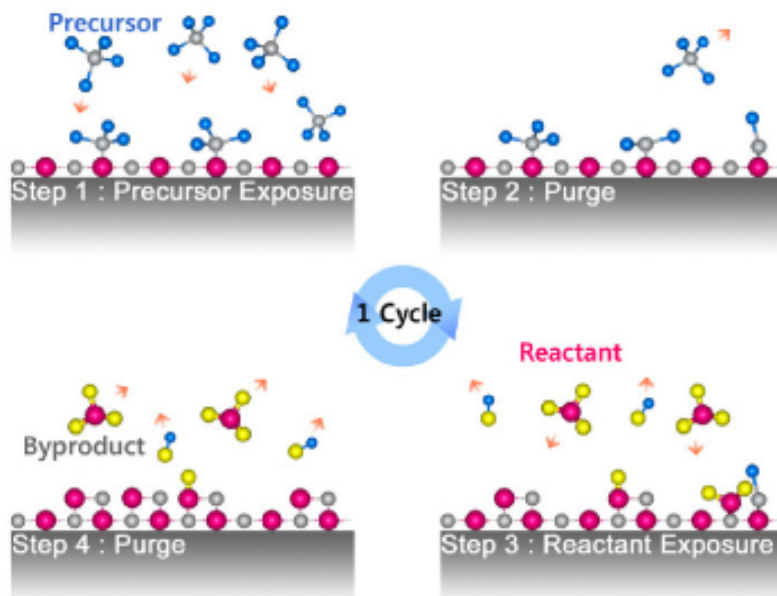

FIGURE 12   Schematic diagram of a deposition cycle with four steps. Reprinted with permission from [66], Copyright 2009, Elsevier.

3.1.3 Reactive Ion Etching (RIE)

Reactive ion etching (RIE) is an important process in nanofabrication which is used to remove partially or totally a thin film layer. RIE is a dry etching method which uses chemically reactive plasma to remove deposited material. The plasma is generated under low pressure by an electromagnetic field supplied by a RF generator. The system configuration is similar with this used for PECVD. Ions from the plasma react chemically with the material deposited on a substrate resulting in dissolution. The ions can cause as well sputtering of the material by transferring some of their kinetic energy. Depending on the material needed to be removed, different gases and conditions for each process should be applied. For instance, the removal of SiO_2 requires the use of CHF_3 at room temperature. By this way, an anisotropic etching of a material can be achieved. For the purposes of this study, a Plasmalab80Plus RIE (Oxford Instruments) system was used.

3.2 Microscopy techniques

3.2.1 Optical microscopy

Bright Field Optical Microscopy is the simplest and the most common illumination technique used in light microscopes. A light microscope is an optical instrument using the visible light to produce magnified image of a specimen. The essential components to build a light microscope are: a transillumination light source (1), like halogen lamp, a condenser optical lens (2) to focus the light onto the specimen, the stage (3) to place the specimen, an objective optical lens (4) which collects the light from the specimen and form a magnified image, and the oculars (eyepiece) (5) and camera to view and record the image. There are also some other components less critical to the formation of the image such as diaphragms and filters. A schematic representation of a light microscope is shown in Figure 13.
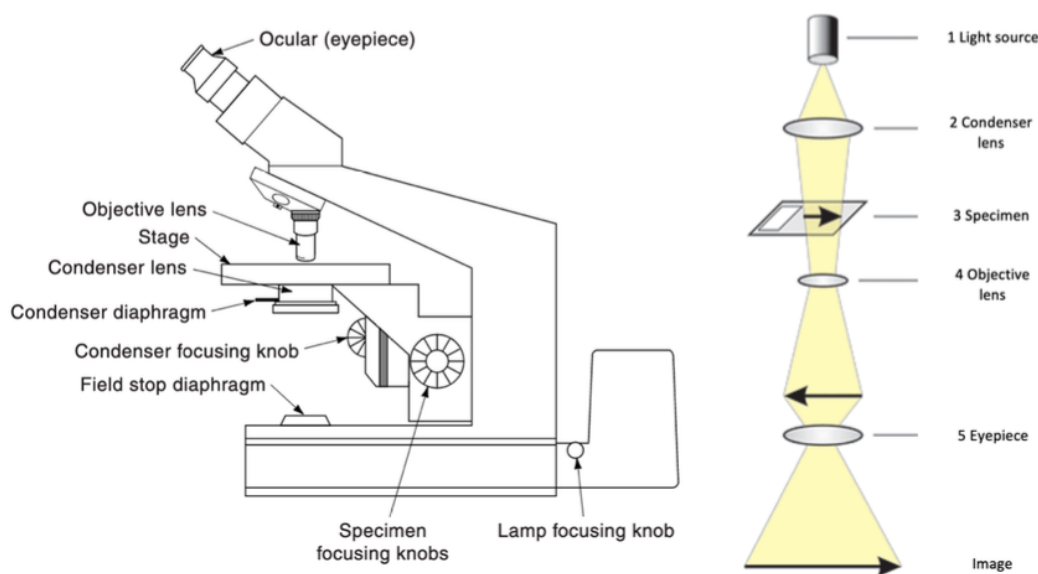

FIGURE 13   Schematic representation of a light microscope. Reprinted with permission from [67], Copyright 2012, John Wiley and Sons.

The biggest limitation of an optical microscope is its resolving power. The resolving power (or resolution) of a microscope is defined as the smallest distance between two objects resolved with the eyes, in other words, the ability to reveal adjacent structural detail as distinct and separate. This happens because of the diffraction of the light. Therefore, the resolution of the microscope is affected by the wavelength of the light (λ), the refractive materials used to manufacture the objective lens, and its numerical aperture (NA). The latter is given by the equation:

$$d = \frac{\lambda}{2NA} \qquad (27)$$

In Bright field microscopy, both directly transmitted and scattered light are collected by the objective lens contributing to image formation. Therefore, the background is very bright resulting to images with low contrast in which details are poorly visible. This problem can be solved by using dark field microscopy where the unscattered beam from the image is removed and the final image presents a dark background improving image contrast.

In order to illuminate specimens in the dark field, the central light rays along the optical axis of the microscope must be blocked. As a result, only those oblique rays originated at large angles are allowed to strike the specimen. This can be obtained quickly with bright field by rotating the condenser turret to illuminate the specimen obliquely. Another way to achieve this is to place a small opaque disk between the light source and the condenser lens. Most of the light is blocked because a hollow cone of light focused on the specimen is created after passing through the condenser. By this way, the condenser creates a hollow cone of light rather than a filled cone of light (bright field). The light at the apex of the cone is focused at the plane of the specimen and after passing the specimen plane, it spreads again into a hollow cone. The only light that reaches the objective is this one scattered by the structures in the specimen. The final image show bright objects on a dark background. In order to increase the resolution, the condenser lens and the specimen should be immersed in oil. The immersion oil will increase the numerical aperture (NA) of the condenser so that the resolution limit will be decreased. The optical images of the samples in the current study were acquired using an Olympus BX51TRF microscope.

3.2.2 Transmission Electron Microscopy (TEM)

Transmission Electron Microscopy (TEM) [61] is a microscopy technique capable of revealing even the smallest features of atomic resolution in a specimen when an electron beam is transmitted through it. This kind of microscope provides resolution much better than light microscopes because of the smaller de Broglie wavelength of electrons with energy E given by the equation:

$$\lambda = \frac{1.22}{\sqrt{E}}. \qquad (28)$$

Basic requirement for imaging is the thickness of the specimen to be approximately equal or less than 100 nm in order to be electron transparent.

The basic operation principal of a conventional TEM instrument can be described in Figure 14. One of the most important parts is the electron source-gun (1). There are only two types of sources: thermionic, like tungsten(W) filaments or lanthanum hexaboride (LaB$_6$), and field-emission sources, like fine tungsten needles.

This crossover acts as an object for the first electromagnetic lens (2) in the illumination system consisting of several electromagnetic condenser lenses determining the size of the beam. After the condenser lenses, the beam passes through

an aperture (3) which confines it and moves the scattered electrons away. Next, the electron beam hits the specimen (4) and the transmitted part is focused on an electromagnetic objective lens (5). Again it passes through an aperture (6) which enhances the contrast by blocking the diffracted electrons of high angle. The electromagnetic projector lens (7), finally, is used to project the beam to the viewing screen (8). The viewing screen is coated with ZnS (10-100 μm) emitting a green fluorescent light. The image is recorded by a charge-coupled device (CCD) camera as CCD is coupled with a scintillator which collects the transmitted electrons and converts them to photons. A JEOL-JEM 1400 TEM was used for the imaging of the samples.
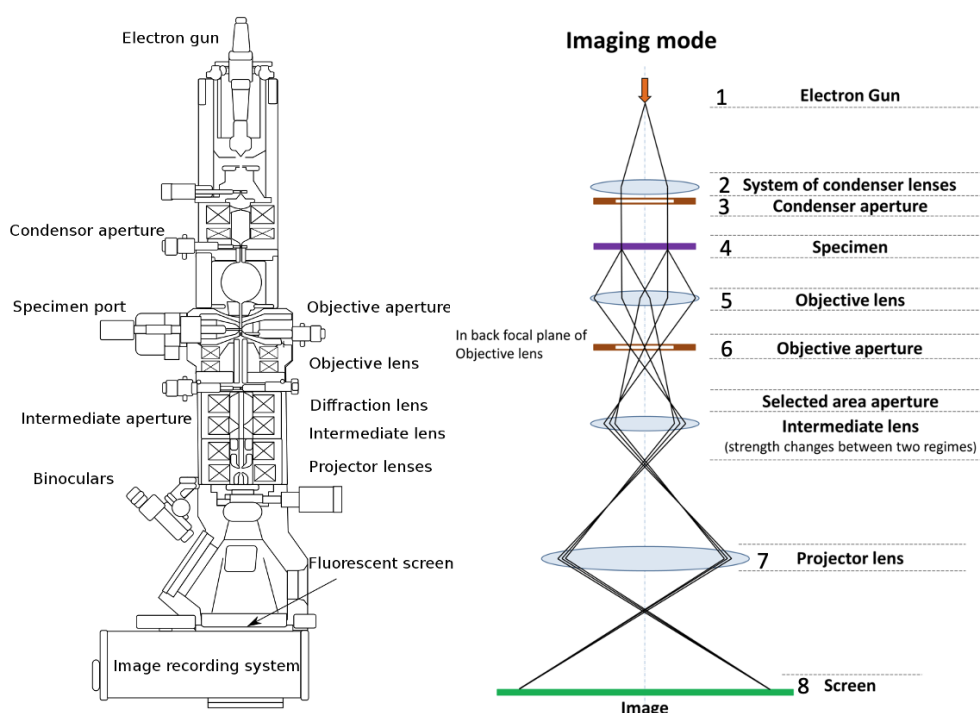

FIGURE 14   Representation of a TEM instrument [68].

3.2.3 Helium Ion Microscopy (HIM)

Helium Ion Microscopy (HIM) [69] is a relatively new technique which offers a possibility for both surface imaging and Focused Ion Beam (FIB) milling in a single tool. Contrary to Scanning Electron Microscopy (SEM), HIM can image non-conductive materials without additional conductive coating. In addition, the direct ion beam in HIM can mill and pattern very small features with minimum damage to the crystal lattice.

HIM working principal consists of three parts: Helium ionization and acceleration, beam formation, and sample interaction with the beam (Figure 15). A Gas Field Ion source (GFIS) (1) provides an emitter (tungsten) with a three sided pyramid tip apex. This tip is shaped in such a manner in order to form a trimer. By this way, helium ionization happens at the end of the tip. Then, ion beam

should be focused before striking the sample surface. For this reason, the ion beam should pass from an extractor (2), a condenser lens (3), an aperture (4), deflectors (5), and an objective lens (6). As a result, a beam of 0.25 nm diameter is formed with spot of 0.5 nm diameter. Except of helium, the tool is equipped also with neon gas which is used mainly for nanofabrication as it is heavier than helium. The HIM tool, which was used in this study, was a Zeiss Orion Nanofab Helium Ion Microscope.
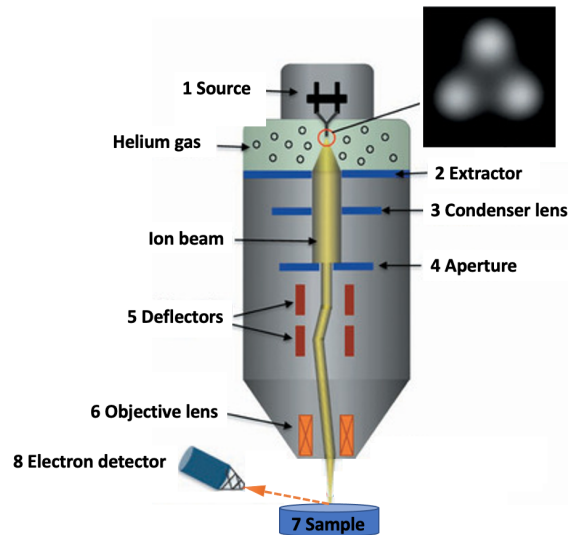

FIGURE 15   Helium Ion Microscope (HIM) configuration. Reprinted with permission from [70], Copyright 2009, IOP Publishing.

As the focused ion beam penetrates the sample (7), the interaction between the accelerated ions and the target atoms produce a number of different signals. For the imaging of the sample surface, secondary electrons (SE) are used. Compared with SEM, the interaction volume for SE generation is smaller for He. A typical SEM beam of low energy electrons (1 keV) produce less damage on the sample, but there are many backscattered electrons which also produce SE some distance away from the incident beam contributing significant non-local information to the image. On the other hand, the small scattering of the helium ions (30 keV) results in minimum beam divergence inside the sample. Consequently, the escaping secondary electrons reveal information about the region of interest. Finally, the SE are collected by electron detectors (8) (CCD camera) to form an image.

3.3   Thin film analysis

3.3.1 Time-of-Flight Elastic Recoil Detection Analysis (ToF-ERDA)

There are several materials characterization techniques which can reveal information about thin films properties. Time-of-Flight Elastic Recoil Detection Analysis

(ToF-ERDA) [71] is an ion beam analysis technique capable of determining the elemental composition of a thin film. This technique requires the use of an accelerator system including usually an ion source and and an electrostatic accelerator capable of producing heavy ion beam from 1 MeV to 200 MeV.

According to the elastic scattering collision between two particles, the incident ion recoils the target atom obtaining a characteristic energy E_2 (Equation 7). In order to quantify the atomic concentrations for each recoiled element from a sample, the number of particles detected (A) should be measured, the solid angle (Ω) should be defined, the scattering cross-section (σ) (different for each element) should be calculated, and the total number of incident particles Q should be known. Therefore, the number of target atoms per unit area, which is the product of the volume density of atoms in the target (N) and the thickness of the sample (t) can be given by the equation:

$$A = \sigma\Omega * Q * Nt. \tag{29}$$

Since the interest is focused on the concentration of the atoms beneath the surface of the target material, the energy loss of ions travelling through the material must be taken into account as well. In Figure 16, a schematic diagram of a typical ToF-ERD set-up is shown. σ can be calculated from the differential scattering cross-section which expresses the probability of a binary collision to take place. The scattering cross-section for a recoiled particle is given from the equation:

$$\frac{d\sigma}{d\Omega} = \frac{[Z_1 Z_2 e^2 (M_1 + M_2)]^2}{(8\pi\epsilon_0 E_0 M_2)^2 cos^3\theta}, \tag{30}$$

where Z_1 and Z_2 the atomic number of the incident and recoiled atom, respectively, M_1 and M_2 their atomic masses, ϵ_0 the electric permittivity in vacuum, E_0 the incident energy, and θ the scattering angle.
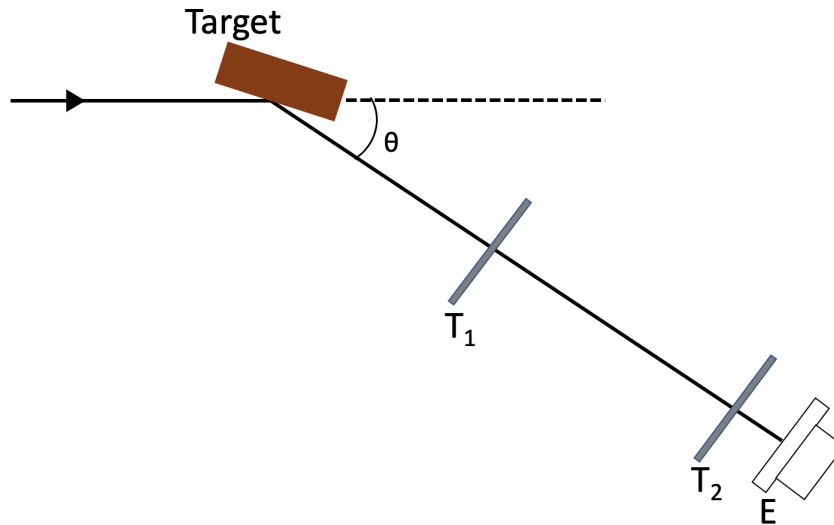
FIGURE 16   A typical ToF-ERD set-up with two time detectors (T$_1$ and T$_2$) and an energy
            detector (E).

Time-of-Flight technique uses two time detectors placed on a distance L between them. Since the time (T) and the distance (L) that a particle travels between the detectors are known, the velocity of the particle can be calculated. An energy detector is used to measure the energy of the recoiled particles. As a result, the mass of the recoiled atoms can be differentiated.

By this way, mass separation can be achieved and a coincidence time-of-flight (ToF) and energy (E) histogram will be obtained with characteristic "banana" curves corresponding to different masses (Figure 17). The knowledge of the mass is crucial for the calculation of the scattering cross-sections. In this study, the 1.7 MV Pelletron accelerator at the Accelerator Laboratory of the University of Jyväskylä was used with ^{63}Cu^{6+} ion source [72]. The energy of the ^{63}Cu^{6+} beam was 11.9 MeV. The analysis of the measurements was done using the software Potku [73].

In 2D TOF-E histogram (Figure 17), the ToF detector channel is given as x axis and the energy detector channel as y axis. In Potku, we determine the different elements and isotopes by graphically placing polygons around the curves in the ToFâE histogram (Figure 17). By this way, the determination of the sample composition as a function of depth is achieved. Firstly, an homogeneous sample composition is assumed by correcting the total yield of each element with the corresponding scattering cross-section. Then, the original depth for each detected recoiled atom is calculated backwards using the detected energy, stopping forces, and the known measurement geometry. This calculation is repeated iteratively until the composition does not change significantly. As a result, the absolute concentration for each element over the depth of the thin film can be extracted.
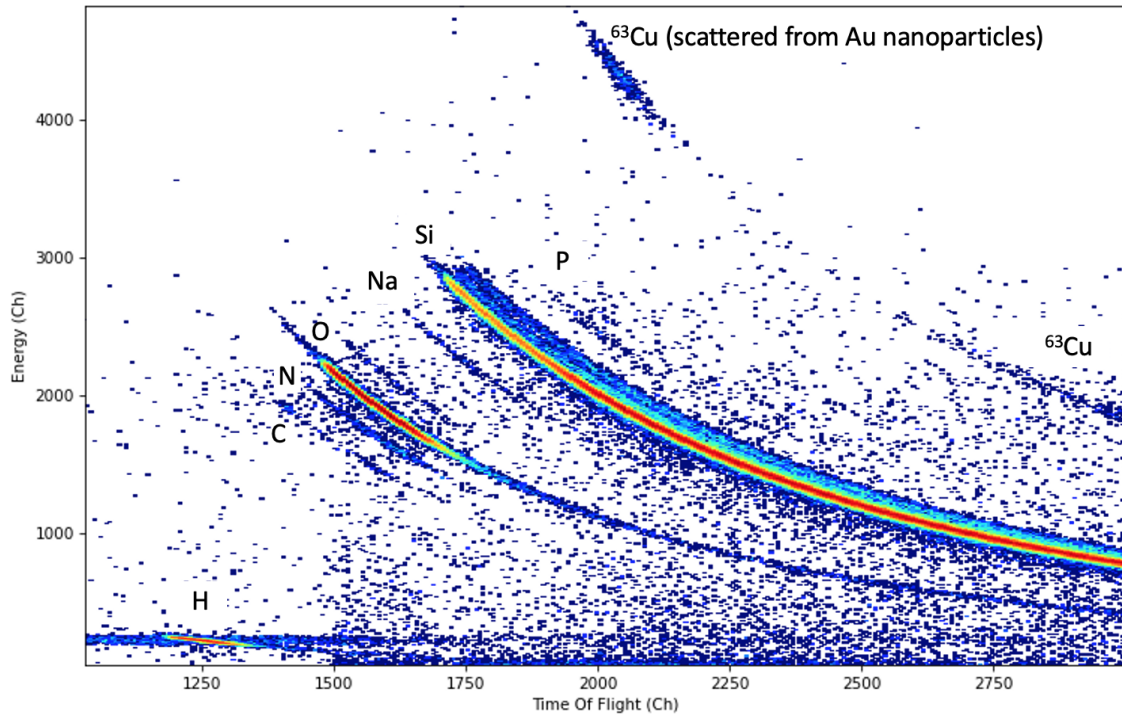
FIGURE 17   Coincidence time-of-flight and energy histogram of a ToF-ERDA measurement from Si/50 nm PECVD SiO$_2$/NPs/50 nm PECVD SiO$_2$ as-deposited sample. Modified with permission from [PII], Copyright 2022, AIP Publishing.

3.3.2 X-ray reflectivity (XRR)

Except for ToF-ERDA, X-ray reflectivity (XRR) [74] measurements were applied to reveal information about the thickness, density, and roughness of the grown films. This technique uses the effect of total reflection of the X-rays from the specimen. The X-rays undergo total reflection when they hit the surface of a material at an angle smaller than the critical angle for total reflection (Figure 18). It actually measures the reflected X-ray intensity at an angle equal with the incident angle. The relative X-ray reflectivity is given approximately by the equation:

$$\frac{R(Q)}{R_0(Q)} = |\frac{1}{\rho_\infty} \int_{-\infty}^{\infty} e^{iQz} (\frac{d\rho_e}{dz}) dz|^2, \tag{31}$$

where $Q=4\pi sin(\theta)/\lambda$, λ is the X-ray wavelength, ρ_∞ is the density deep within the material, and θ is the angle of incidence. Below the critical angle, X-rays penetrate only a few nm into the sample, but above this angle the penetration depth increases rapidly and the reflectivity decreases proportionally to Q^4. The measurements in this study were done with PANalytical X'Pert Pro Alpha 1 MPD X-ray powder diffractometer set up to X-ray reflectivity with Cu $K\alpha_1$ X-ray source (λ=0.154056 nm, V=45 kV, I=40 mA). The analysis of the samples was done with the use of GenX open software where a fitting was made at the experimental data from which the values of the thickness, density, and roughness of SiO$_2$ were extracted.
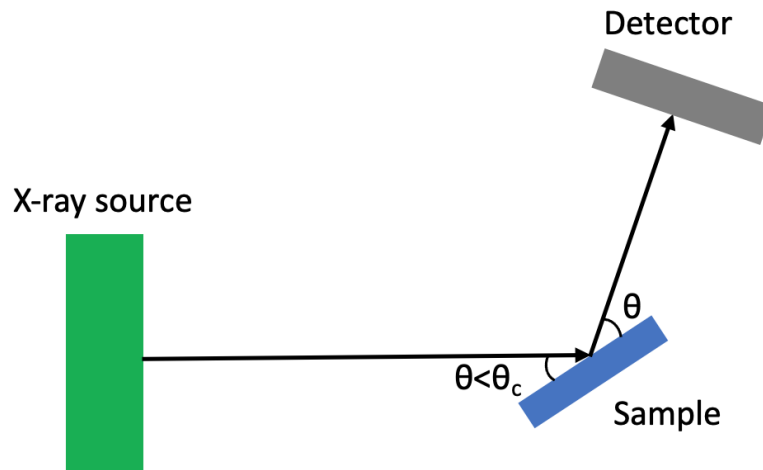
FIGURE 18   Simplified X-ray reflectivity set-up where incident X-rays are totally re-
flected at an angle equal with the incident.

3.3.3 Spectroscopic ellipsometry

Regarding the film thickness measurements, spectroscopic ellipsometry (Figure 19) is an accurate and fast method to determine the thickness of a film. This is an optical technique capable of measuring the thickness and the refractive index of thin films from a few to several hundreds of nm by using the interaction of the polarized light with the material surface [75, 76]. In this study, the measurements were done by using a SOPRA GES 5E ellipsometer. A linearly polarized light, which reaches the surface of a material under an angle of incidence, can be expressed by two components, one parallel (denoted -s) to the plane of incidence and one perpendicular (denoted -p) to that. After the reflection of the light from the surface, its polarization has changed to elliptical. As a result, the components of the light has changed.
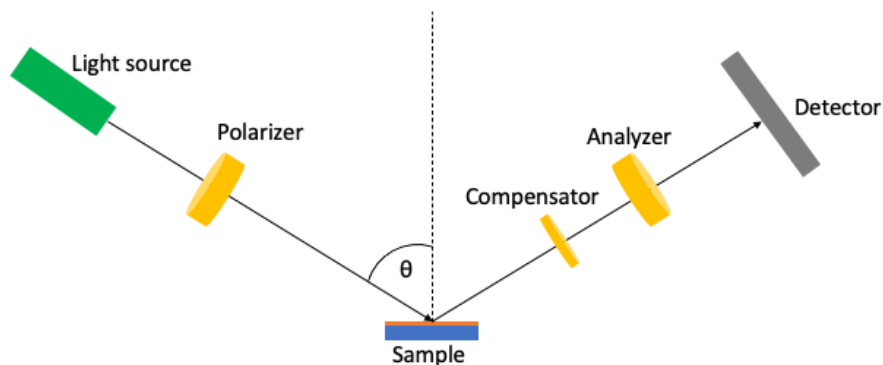

FIGURE 19   Ellipsometry set-up where the light beam from the source passes through the polarizer, hits the sample, and is reflected entering the compensator first and then the analyzer before reaching the detector.

The ellipsometer uses the ratio of the components of the reflected light (R_p/R_s) to estimate the thickness (t) and the refractive index (n) of the film based on the

equation:

$$\frac{R_p}{R_s} = \tan(\Psi)e^{i\Delta}, \tag{32}$$

where Ψ and Δ are the relative attenuation and phaseshift of the two polarization eigenstates, respectively. These quantities are determined from the measurements, however they do not give direct information about the thickness and the refractive index. Therefore, a model based on Maxwell's equation needs to be used in order to calculate the desired values [76, 77].

4 SAMPLE FABRICATION, IRRADIATION, AND CHARACTERIZATION

4.1 Sample preparation

The use of thin Si_3N_4 TEM windows grid as a substrate is essential for the fabrication of the samples. The grid consists of nine windows (eight windows with 100×100 μm^2 size and one window with 100×350 μm^2 size) of 20 nm thickness (Figure 20). The TEM imaging of the same embedded nanostructures is possible before and after the irradiation. On top of the grid, a film of amorphous material is deposited either by Plasma-Enhanced Chemical Vapor Deposition (PECVD) or by Atomic Layer Deposition (ALD). As a next step, nanostructures are placed on top of the film. They were either made by colloidal chemistry (obtained by Sigma-Aldrich) and dispersed on top of the film by dropcasting or they were fabricated by direct ion beam milling. Finally, a second film of the same material was deposited on top of the nanostructures in order to encapsulate them in the amorphous material.

The shape of the nanostructures were chosen to be sphere and rod. Since metallic nanoparticles are subject to elongation along the ion beam direction, nanostructures of two different metal species were used: gold and silver. A high deposition temperature of the matrix material can induce shape changes to the nanoparticles. Gold nanoparticles are observed to deform at 300 °C, leading to the conclusion of choosing lower deposition temperature than 300 °C. This observation is more visible in nanorods, because the spherical ones keep their spherical shape after cooling. Figures 21a,b show the deformation of the nanorods after PECVD SiO_2 deposition at 300 °C. As a result, lower deposition temperatures were tested and deposition at 200 °C showed that nanorods do not change shape (Figure 21c).

Possible shape changes of the post-deposition thermal annealing on the embedded nanoparticles were investigated as well. The thermal annealing process was accomplished in a conventional furnace (Carbolite CTF/12/65/550 tube furnace). The tube furnace was shielded by two metallic lids, one left and one right.
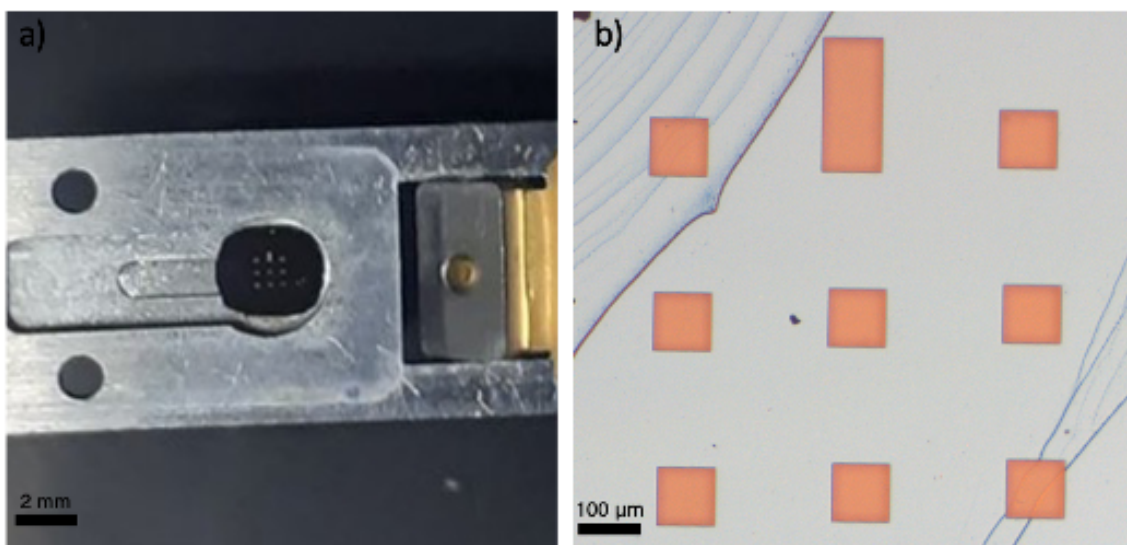
FIGURE 20 (a) Photo of a TEM grid and (b) optical microscope images of a TEM grid with SiO$_2$ deposited by ALD. Modified with permission from [PII], Copyright 2022, AIP Publishing.
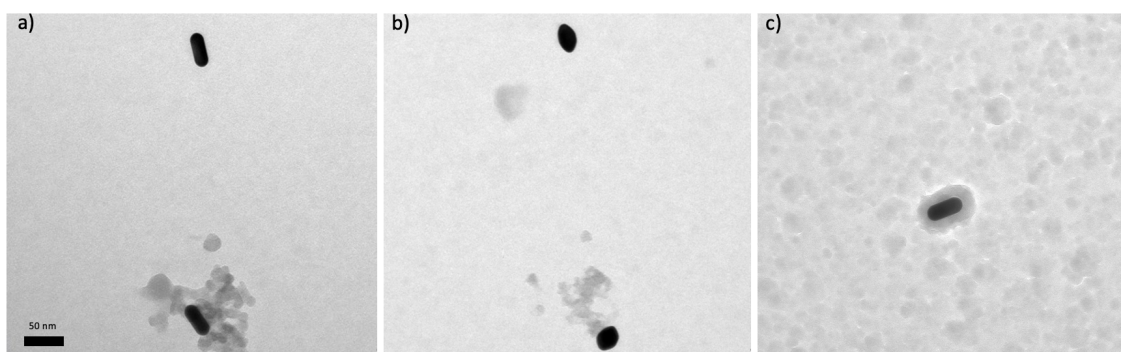

FIGURE 21 TEM images of gold nanorods (a) before the PECVD SiO$_2$ deposition at the 300 °C and (b) after the PECVD SiO$_2$ deposition and etching. (c) TEM image of gold nanorod after PECVD SiO$_2$ deposition at 200 °C. Reprinted with permission from [PII], Copyright 2022, AIP Publishing.

The right lid is used to insert the samples inside the tube and the left allows the flow of different annealing gases, such as N$_2$, O$_2$, and Ar. This is shown in Figure 22, in which gold nanorods on a bulk Si substrate were imaged before and after annealing at 900 °C and etching of top SiO$_2$ prior imaging. There was no significant change even after annealing at 900 °C.
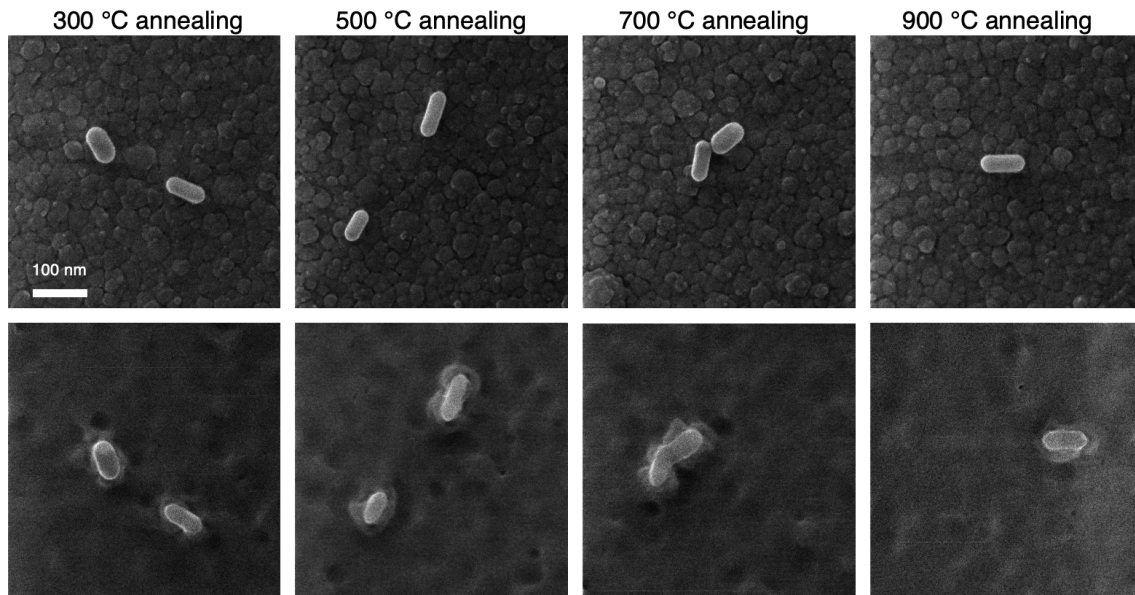
FIGURE 22   Helium Ion Microscope (HIM) images of nanorods embedded in PECVD
SiO$_2$ before and after annealing at various temperatures. The top row i-
mages show nanorods before the deposition of the second layer on the top
and the bottom row images show nanorods after annealing and etching by
RIE of the excessive layer. Reprinted with permission from [PII], Copyright
2022, AIP Publishing.

Three different amorphous materials were selected to be used in the sam-
ple fabrication: SiO$_2$, Al$_2$O$_3$, and TiO$_2$. SiO$_2$ was deposited by both PECVD and
ALD. SiO$_2$ films were deposited by a Plasmalab80Plus PECVD (Oxford Instru-
ments) at 200 °C with silane (SiH$_4$ in Ar) and nitrous oxide (N$_2$O) as precursors
[78]. The chamber was pre-heated and purged with N$_2$ for 2 min. The working
pressure during the deposition was 133 Pa. The growth rate of the deposited
film was 50 nm/min. The deposition of SiO$_2$ films at 200 °C by ALD was done
using a Beneq TFS 200 cross flow reactor working at 150 Pa base pressure du-
ring the deposition. Nitrogen from Inmatec PN 1150 nitrogen generator (99.999%
purity) was used as a carrier gas as well as for purging between the precur-
sor pulses. One ALD cycle consisted of subsequent pulses of (3-aminopropyl)-
triethoxysilane (APTES) (Sigma Aldrich, 99%), deionized water, and O$_3$ which
were used as precursors for the deposition. APTES was heated to 95 °C in order
to provide sufficient vapor pressure while H$_2$O was kept at room temperature
and O$_3$ was produced with BMT 803 N ozone generator from O$_2$. One ALD cycle
consisted of 1.25 s, 0.75 s, and 0.9 s pulses of APTES, H$_2$O, and O$_3$, respectively.
Exposure time after each pulse was 20 s, 18 s, and 15 s and purging times were
20 s, 15 s, and 15 s, respectively. The GPC was 0.4 Å/cycle. A set of SiO$_2$ sam-
ples were also fabricated with an additional step of post-deposition annealing at
900 °C for 30 min with N$_2$ flow at a conventional furnace.

Al$_2$O$_3$ and TiO$_2$ were deposited by ALD using the Beneq TFS 200 working at
100-200 Pa base pressure during the deposition. For the deposition of Al$_2$O$_3$ films
at 200 °C, trimethylaluminium (TMA) (Strem Chemicals, >98%) and deionised

water were used as precursors. Both TMA and water pulses were 150 ms long and the purging after each precursor pulse was 3 s. The GPC was 1.1 Å/cycle. The deposition of TiO_2 films at 150 °C was accomplished with the use of titanium tetrachloride ($TiCl_4$) (Sigma Aldrich, >99%) and deionised water, and the growth temperature was kept at 150 °C in order to produce amorphous film. Both $TiCl_4$ and water pulses were 300 ms long and purging time after each precursor was 2 s. The GPC was 0.4 Å/cycle.

In the early stages of this research, the thickness of the SiO_2 matrix (the first material tested) was several hundreds of nm because most of the previous studies were mentioning that nanoparticles should be buried deep inside the matrix in order the elongation to occur. Nevertheless, some studies [2, 79] have shown that the heavy ion irradiation of colloidal nanoparticles, consisted of a 14 nm diameter Au core surrounded by a 72 nm thick SiO_2 shell, resulted in aligned gold nanorods along the ion beam direction. This fact implies that elongation does not requires thick SiO_2 films. For these reasons, on top of 20 nm thick Si_3N_4 TEM grid, a 30 nm PECVD SiO_2 film was the first deposited at 200 °C and after the dispersion of chemically synthesised Au spherical nanoparticles with diameter varying from 5 to 80 nm, another SiO_2 film with 200 nm thickness was deposited in order to embed the nanoparticles. The imaging of the sample took place before the deposition of the second film. After the irradiation, around 150 nm of SiO_2 was etched by RIE so that the sample had the required thickness to be imaged by TEM. In Figure 23, TEM images from this type of sample irradiated at 2×10^{14} ions/cm^2 are shown.
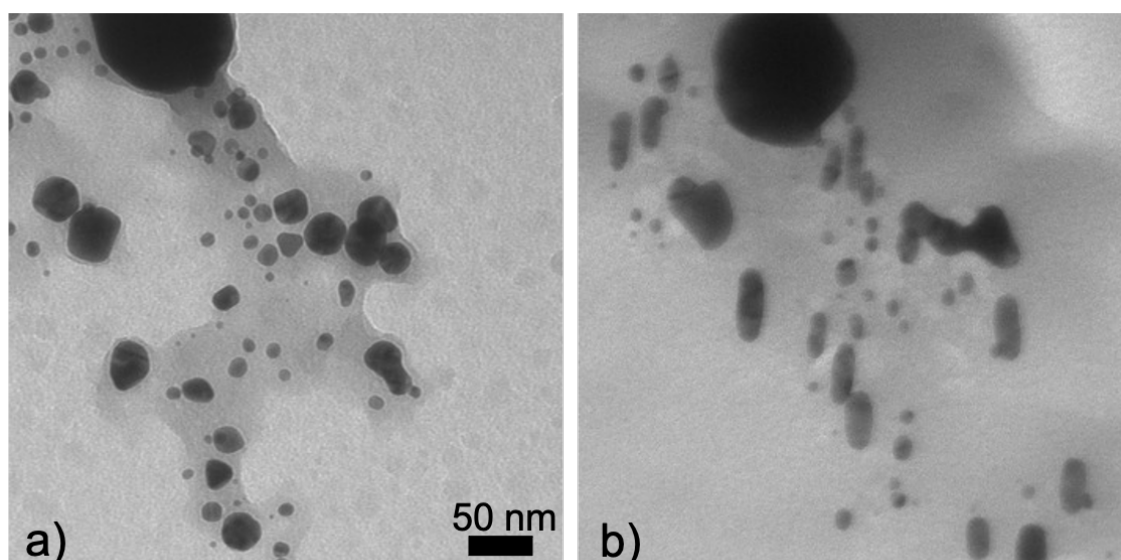
FIGURE 23   TEM images of 20 nm Si_3N_4/30 nm PECVD SiO_2/NPs/200 nm PECVD SiO_2 sample irradiated at 2×10^{14} ions/cm^2 fluence with ^{84}Kr ions (a) before and (b) after the irradiation. Reprinted with permission from [PII], Copyright 2022, AIP Publishing.

When samples with right thickness were fabricated in order to be imaged with TEM (without etching), the elongation results were similar as in Figure 23.

As a result, every step in this procedure was planned carefully in order to monitor the evolution of the nanostructure elongation. The procedure started with a precise fabrication of the sample with the deposition of 50 nm thin film on top of the TEM windows grid. The dispersion or the fabrication of the nanostructures on top of the film was then applied and consequently their encapsulation with the deposition of the second film with the same thickness was following. As a result, chemically synthesised Au spherical nanoparticles with diameter varying between 5 and 80 nm, with a 5 nm step, were embedded in 100 nm SiO_2 made by ALD or PECVD, 100 nm ALD Al_2O_3 and 100 nm ALD TiO_2. Additionally, Ag spherical nanoparticles with diameter varying between 5 and 25 nm were embedded in 100 nm ALD Al_2O_3 and 100 nm ALD TiO_2. Regarding the nanorods, Au nanorods with diameter varying from 20-45 nm and length varying from 30-90 nm were embedded between two SiO_2 layers of 50 nm thickness each. The following steps were the imaging of the embedded nanostructures by TEM and their SHI beam irradiation under $45°$. Finally, the irradiated samples were imaged in order to investigate the effect of the irradiation.

4.2   Thin film properties investigation

Additional Si substrate was present in the depositions in order to investigate the properties of the grown films using thin film analysis techniques. ToF-ERDA was used to quantify the elemental composition of the grown films prior to irradiation. Moreover, spectroscopic ellipsometry was applied to confirm the desired thickness for the grown films as well as to measure their refractive index. Except ellipsometry, XRR was used to measure the thickness in addition to their roughness and density.

4.3   Lithography of nanostructures

The dispersion of chemically synthesized Au nanorods leads to random nanorod orientation on the surface of the sample. This inconvenience can be overcome by applying HIM nanolithography in order to create nanorods with the desired size and orientation. A Zeiss Orion Nanofab Helium Ion Microscope was used for imaging with helium beam as well as for patterning with neon beam. A NanoPatterning and Visualization Engine (NVPE) was used to generate the milling patterns.

The fabrication of metal nanostructures was made as following: A thin layer of metal (gold) (15-20 nm thickness) was first deposited on TEM grid using Ultra High Vacuum (UHV) evaporator. The next step was the milling of a selected area by neon beam in HIM. A rectangle area was selected where neon beam removed the material inside this area leaving to the center a nanostructure of desired shape

and orientation. In Figure 24a, a HIM image is shown with nearly spherical gold nanoparticles patterned on top of a TEM grid, while in Figure 24b, a TEM image with patterned gold nanorods on top of a TEM grid are shown after embedding them in SiO_2.
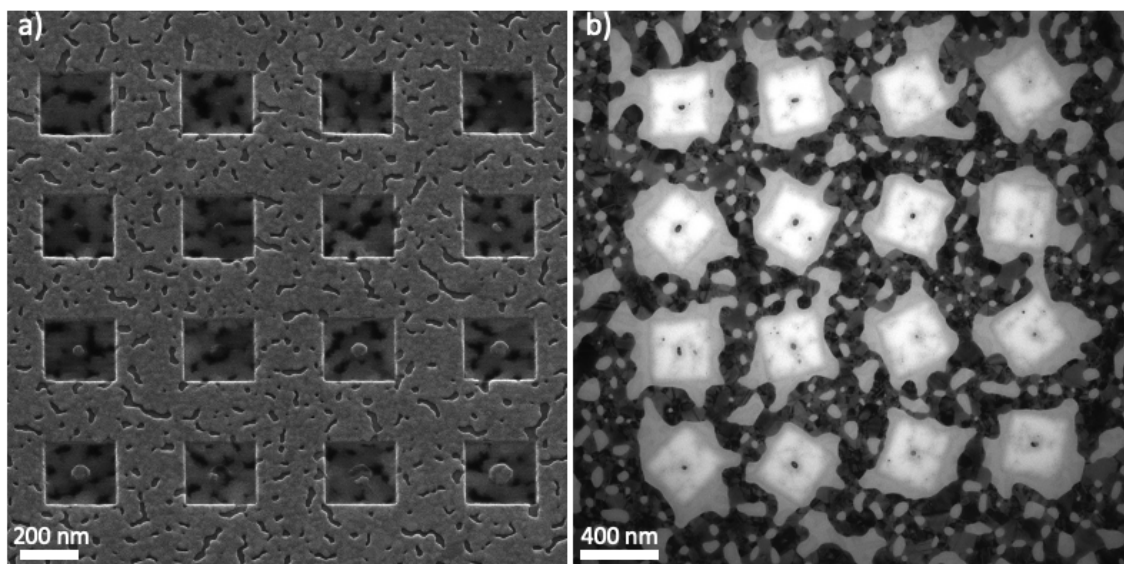

FIGURE 24   (a) HIM image of nearly spherical gold nanoparticles patterned on top of a TEM grid and (b) TEM image of patterned gold nanoparticles on top of a TEM grid after embedding them in SiO_2. Modified from [PIII] under the license CC BY 3.0.

4.4   Irradiation

The swift heavy ion irradiation of the samples were performed mainly in University of Helsinki and partly in University of Jyväskylä. In Helsinki, 50 MeV $^{127}I^{9+}$ ions from the TAMIA 5 MV tandem accelerator at Helsinki Accelerator Laboratory were used (Figure 25). The angle of incidence was $45°$ (Figure 26) and several fluences from 10^{13} ions/cm^2 to 5×10^{14} ions/cm^2 were applied at room temperature. During the irradiation, the beam was raster scanned over 2×2 cm^2 area by magnetic deflectors. The beam current was measured by beam profilometer placed in front of the sample. The calibration of the profilometer was done against Faraday cup with aperture area of 0.6 cm^2, which was placed behind the sample (Figure 26b). In order to achieve a homogeneous irradiation over the samples, a millimeter paper was irradiated to measure the beam area. By this way, the beam spot could be controlled and it covered evenly each TEM grid (around 6 mm^2 area). The TEM grids were mounted on silver plates using a conductive carbon paste to avoid any damage by overheating during the irradiation. All of the nine windows in a TEM grid were covered by the beam spot.

Additionally, swift heavy ion irradiation of the samples was performed with

383 MeV $^{84}Kr^{16+}$ ions from K-130 cyclotron at JyvÃ€skylÃ€ Accelerator Laboratory in 45° incidence with several fluences at room temperature. Samples were so thick that etching part of the SiO_2 film with a Plasmalab80 Plus system equipped with RIE was essential.
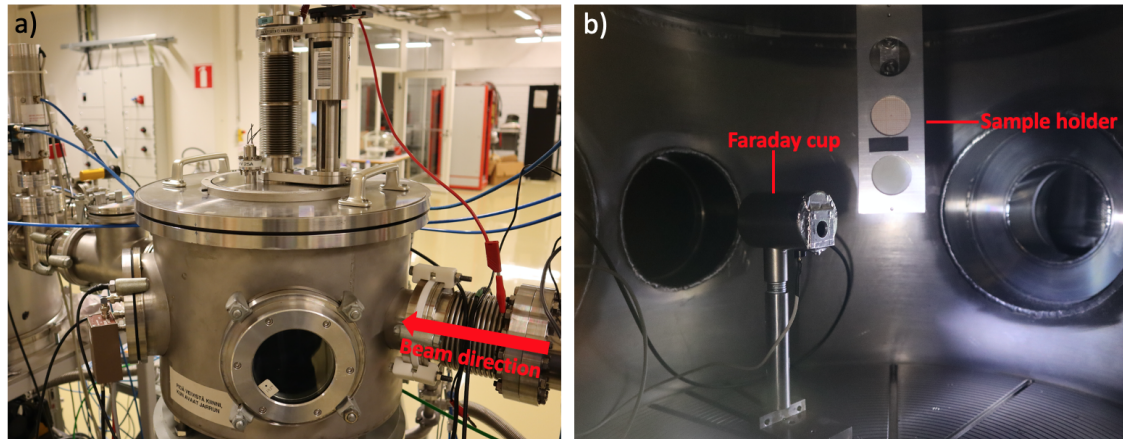

FIGURE 25   (a)Photo of the chamber where the samples were irradiated in Helsinki.(b) Photo from inside the chamber where a Faraday cup is also visible. The ion beam is coming from the right.
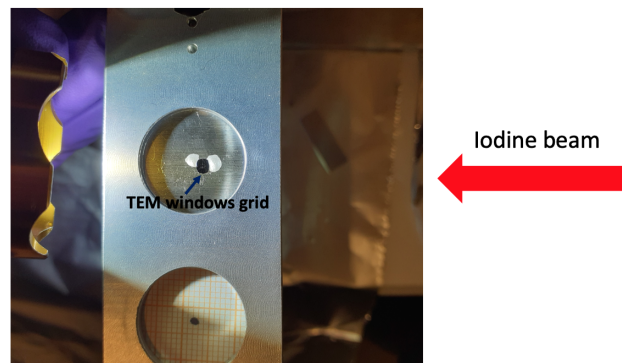
FIGURE 26   Schematic representation of the ion beam hitting the sample at 45° angle.

4.5   TEM imaging of the nanostructures

The samples were imaged with a JEOL-JEM 1400 TEM operated at 120 kV. Before the irradiation, the samples were imaged from the top without tilting the TEM stage. After the irradiation, a series of three images was taken for each (Figure 27a) image before the irradiation: one image from the top without tilting the stage, one image after tilting the stage 45° so that electron beam direction is perpendicular to ion beam direction and one image after tilting the stage –45° so that electron beam direction is along the ion beam direction (Figure 27b,c, and

d). If the total thickness of the sample exceeds the maximum thickness allowing TEM imaging, the imaging of the samples before the irradiation should be done before adding the matrix second layer.
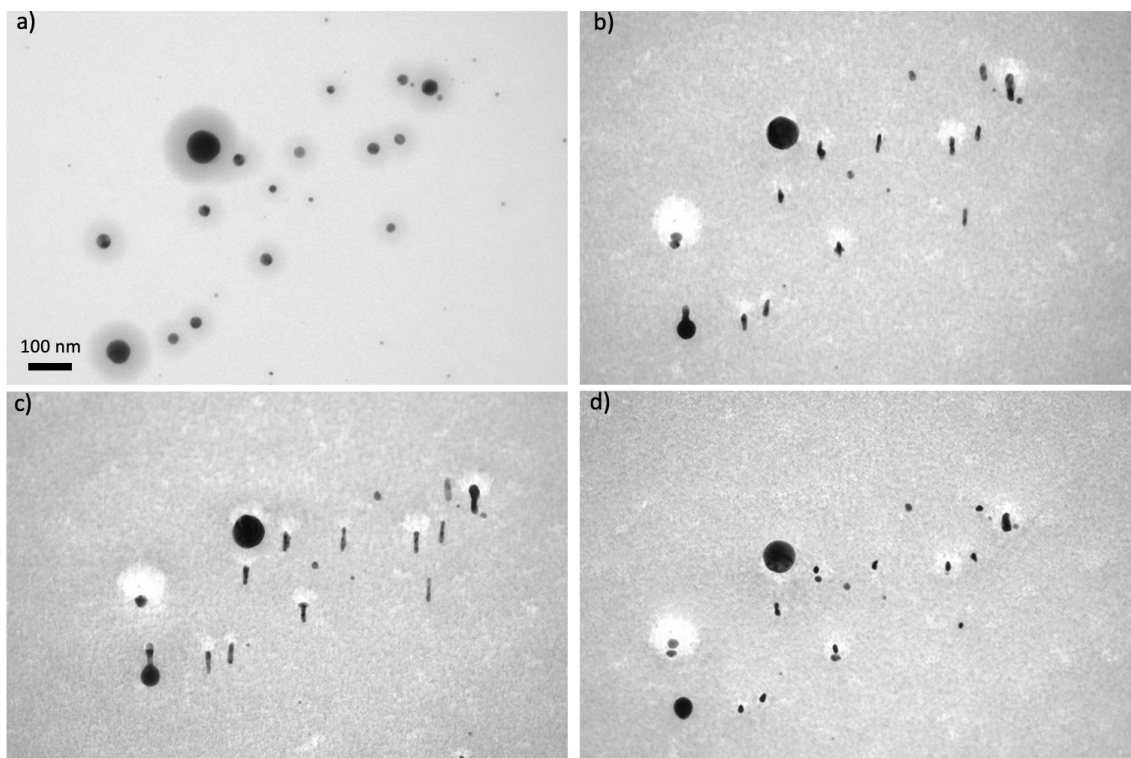

FIGURE 27   TEM images of the annealed 20 nm Si_3N_4/50 nm ALD SiO_2/NPs/50 nm ALD SiO_2 sample irradiated at 5×10^{14} ions/cm^2 which were taken (a) from the top before the irradiation, (b) from the top after the irradiation, (c) perpendicular to the ion beam direction after the irradiation and (d) along the ion beam direction after the irradiation. Modified with permission from [PII], Copyright 2022, AIP Publishing.

Since the main interest of this work was focused on the geometry of nanoparticles, an accurate and fast method was needed to determine the geometric characteristics of each particle before and after the irradiation. Even if there are several open softwares like Gwyddion [80] or ImageJ [81] to measure the size of a nanoparticle, it is hard to accomplish that as automatic and fast as possible when there is a need to match the same nanoparticle before and after the irradiation. An image segmentation code was written in Python to measure the dimensions of the nanoparticles before and after the irradiation. For example, before irradiation an image picturing spherical nanoparticles is loaded, particle diameters are measured automatically and each one of them is represented by a number in order to be easier to match it with the same particle after the irradiation. In this way, plenty of data can be collected and detailed elongation analysis as a function of the initial particle size can be accomplished. In Figure 28, an example of this method is shown for two TEM images before and after the irradiation.
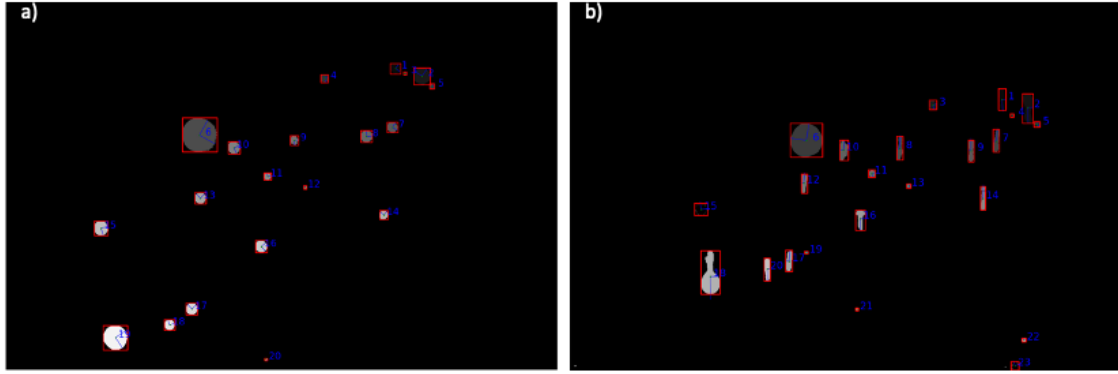
FIGURE 28   Segmented images corresponding to TEM images of the annealed 20 nm Si$_3$N$_4$/50 nm ALD SiO$_2$/NPs/50 nm ALD SiO$_2$ sample irradiated with 50 MeV ^{127}I beam at 5×10^{14} ions/cm^2 which were taken (a) from the top before the irradiation and (b) perpendicular to the ion beam direction. Modified with permission from [PII], Copyright 2022, AIP Publishing.

4.6 Molecular Dynamics (MD) simulations for nanorods

The understanding of the mechanism behind the modification of the nanorods can be achieved by applying atomistic simulations combining molecular dynamics (MD) with inelastic thermal spike model (iTS). Classical molecular dynamics code PARCAS [82, 83] was used since the same has been already applied for the elongation of spherical nanoparticles [14, 84]. To simulate a nanorod, a box of fcc Au is created and a nanorod is cut from this. The size of the simulated nanorod was smaller than the experimental (length 18 nm and width 10 nm) in order to run faster the simulations for multiple ion impacts. The nanorods were embedded inside the matrix with the same way as described by Djurabekova et al [38].

In the simulations, 50 MeV ^{127}I ions consumed a lot of CPU time in order to produce the same results as in experiments. Therefore, we decided to run with Iodine beam until 100 ion impacts and we also used 164 MeV ^{197}Au ions, which are more energetic, in order to produce results with fewer simulated ion impacts [PI]. In MD simulations, interatomic potentials should be correctly adjusted for the motion of the atoms. Watanabe-Samela [30, 31] approaches were applied for interactions in silica, EAM-like for Au-Au interactions [32, 33], and ZBL [34] for Au-O and Au-Si interactions.

System relaxation was done for 50 ps in NPT with zero pressure and 300 K temperature. After the system was relaxed, radial energy deposition was added perpendicular to the initial long axis of the nanorod. The center of the track went through the nanorod in random locations. After adding the radial energy deposition, the system was then simulated for 100 ps in NVE. NVT in 300 K was used in thin boundary regions perpendicular to the ion direction to dampen oscillations from pressure waves and to emulate cooling provided by bulk material. Berendsen thermostat [37] was used for thermostatting and barostatting.

4.7 Optical characterization

Dark field optical microscopy was applied for the detection of metal nanoparticles placed on a transparent substrate (TEM windows grid). By means of this technique, even individual nanoparticles can be detected with high sensitivity and contrast. In order to optically characterise the embedded nanostructures, the microscope (Figure 29) is connected with a spectrograph via an optical fiber. A green LED is used to locate the position of the fiber on the sample. When the fiber is covering the area with a nanostructure, the scattering spectrum from this is measured.
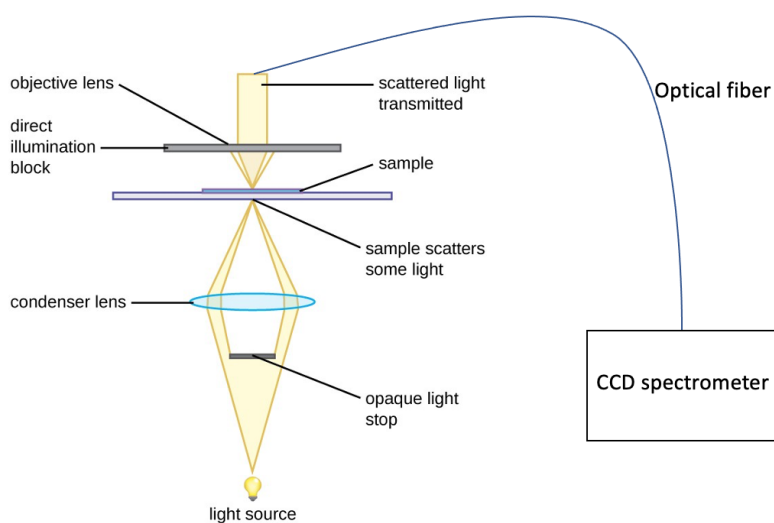

FIGURE 29   A dark-field optical microscope configuration [85].

An Olympus BX51TRF microscope equipped with EOS 6D camera and coupled to Andor SP2150i spectrograph via a fiber (Thorlabs UM22-300-custom; core size, 300 μm) was used to acquire the dark field spectra [86, 87]. The dark field spectra were recorded by Andor IVAC DR-324-FI EMCCD camera, which was attached to the spectrograph. During the recording, Olympus MPLANFL N 100$\times$ objective was used. The microscope was equipped as well a polarizer (Thorlabs LPVISE200-A 2) in order to acquire the signal from different polarization angles and an analyzer (Olympus U-AN360-3) to filter the different light polarization coming from the sample [PIII]. On the microscope sample stage, a clean microscope slide was placed. Underneath the slide, a dark field condenser (Olympus U-DCW) was positioned and a drop of oil was added to the condenser. The condenser and the slide were brought in contact so that there was a thin oil layer between them. Another drop of oil was added to the slide on top of which the TEM windows grid was immersed so that the grid was touching the oil [PIII].

In order to find the correct window and the nanoparticles, TEM reference images were used (Figure 30). A green LED (Thorlabs M530L3) light from the spectrograph end was used to visualize the position of the fiber. The polarization measurements were done by positioning the fiber spot in such a way in order

to cover the desired area. After that, the desired polarization angle was selected (starting from the angle 0°) and the spectrum was recorded. Then an empty area next to the nanoparticle was selected for the background (BG) measurements. The same process was repeated for 45°, 90°, 135° and 180° angles. After finishing the samples measurements, we removed the sample and the condenser, and recorded the lamp spectrum and the dark current (DC). The final nanoparticle intensity I was calculated using the equation 33.

$$I = \frac{I_{AuNP} - I_{BG}}{I_{lamp} - I_{DC}},\tag{33}$$

where I_{AuNP} is the intensity of the scattering light from the nanoparticles, I_{BG} is the intensity of the scattering light from the background, I_{lamp} is the intensity of the light from the lamp, and I_{DC} is the intensity of the dark current.
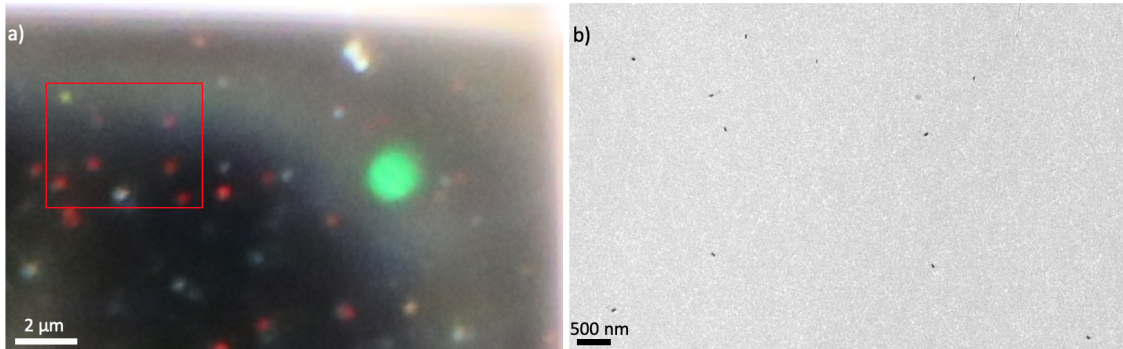

FIGURE 30   (a)Dark field optical images from a sample containing nanostructures and (b) TEM image from the same sample containing the nanostructures located at the red rectangle in Dark-field optical image. The green circle denotes the fiber position. Reproduced from [PIII] under the license CC BY 3.0.

4.8   Optical simulations

The FDTD simulations were performed using Ansys Lumerical FDTD Solutions software (version v202r4) [88]. The simulations were conducted in two ways [PIII]: first, the original model with the air-medium-silicon nitride interface was employed. This model was then contrasted with the infinite medium approximation, which was used to simulate all the results. Figure 31 shows the schematic view of the original model. The dimensions of the gold nanoparticles in simulations were taken from the corresponding TEM images assuming that the elongated nanoparticles are ellipsoids with one long axis and two short axes with equal length. The refractive index (R.I.) of Au was taken from Johnson and Christy [89].
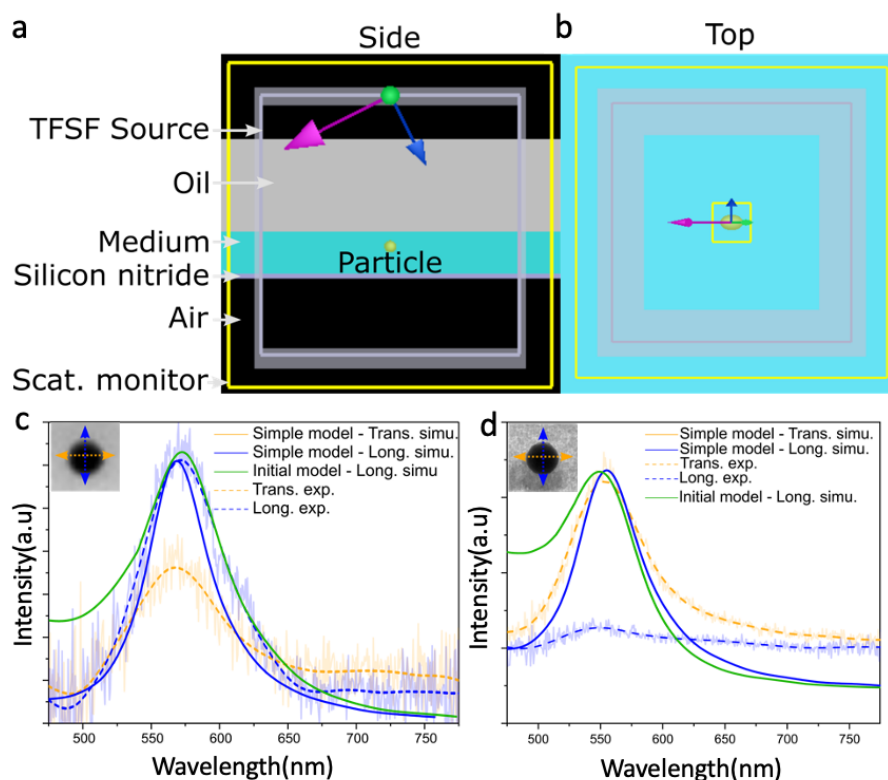
FIGURE 31   (a)-(b) The side and the top view of the original FDTD model of the elongated and embedded nanoparticles either in Al_2O_3 or SiO_2 medium. (c) Comparison between the original model and the simplified model for a spherical nanoparticle embedded in Al_2O_3 medium. The solid green curve depicts the fit using the original model, as the solid blue and yellow curves depict the simplified model. The dashed curves show the corresponding measured data. (d) Comparison between the original model and the simplified model for a spherical nanoparticle embedded in SiO_2. The solid green curve depicts the fit using the original model, as the solid blue and yellow curves depict the simplified model. The dashed curves show the corresponding measured data. The size of the TEM images is 110 nm×110 nm. Reproduced from [PIII] under the license CC BY 3.0.

The air-medium-silicon nitride interface was firstly employed, where the nanoparticles are embedded in the medium (either SiO_2 or Al_2O_3). The solid green curve in Figure 31, which represents the original simulation model for the nanoparticles, is matched with the measured LSPR peaks for the same nanoparticles (the dashed blue and yellow curves). The refractive indexes of SiO_2 and Al_2O_3 were 1.52 and 1.66, respectively. After that, we approximated an infinite medium and changed the R.I. of that in order to fit the simulated LSPR peaks to the experimental ones. The difference with the original model is that the new refractive indexes are averaged, distance-weighted values between air, medium, and silicon nitride allowing the simulation to proceed more quickly. The new refractive indices for SiO_2 and Al_2O_3 were 1.38 and 1.55, respectively. The solid blue and yellow curves in Figure 31 depict the simplified model. Around the nanoparticles, a mesh of 1 nm was applied and an overall mesh of 50 nm was

defined for the rest of the simulated area. The short axis and the long axis are the only two main LSPR modes for our ellipsoid, hence only two polarization angles were taken into consideration that corresponded to these modes (Figure 32).
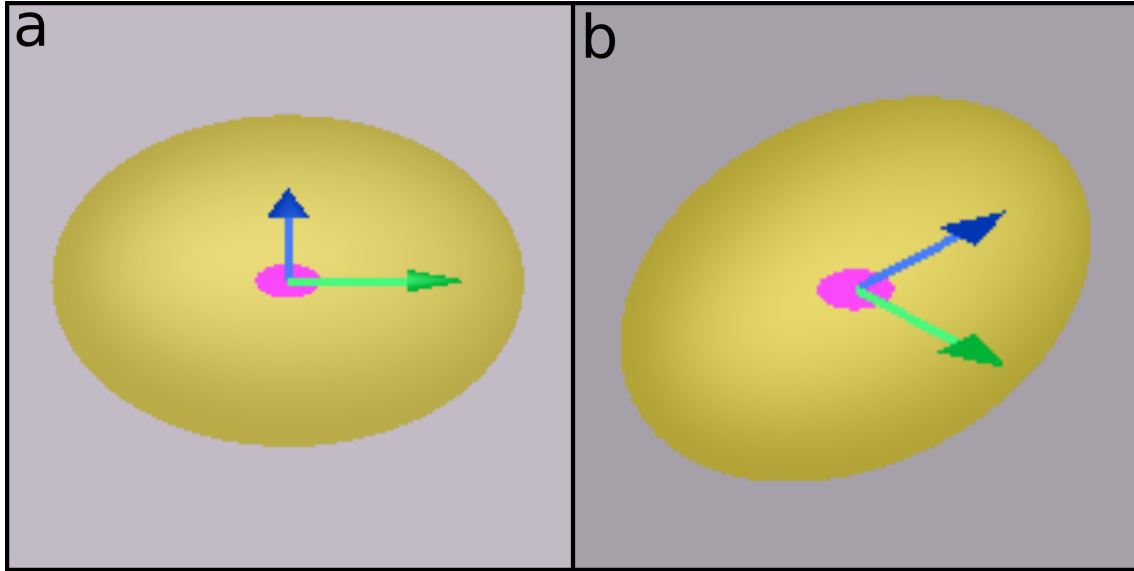

FIGURE 32   ((a)-(b) The two polarization angles considered in the simplified simulations. Reproduced from [PIII] under the license CC BY 3.0.

5 SHI IRRADIATION OF SPHERICAL METALLIC NANOPARTICLES EMBEDDED IN SiO$_2$

5.1 Elongation of SHI irradiated spherical nanoparticles embedded in PECVD and ALD deposited SiO$_2$

Even if a variety of deposition techniques has been used for the deposition of SiO$_2$, the effect of different deposition technique on elongation process has not been studied. Additionally, ALD has not been earlier used for the fabrication of SiO$_2$ which is subject to SHI irradiation. Consequently, the differences in elongation process induced by ALD and PECVD SiO$_2$ were investigated. Additional step of post-deposition annealing was done as well to investigate if there is any effect on the irradiated samples. All the steps described above are shown in Figure 33.
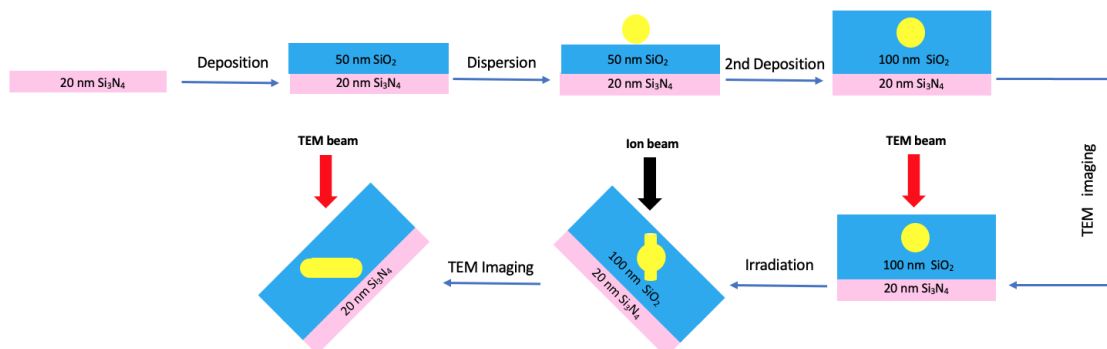

FIGURE 33 Schematic representation of sample preparation, irradiation, and imaging using TEM. Reprinted with permission from [PII], Copyright 2022, AIP Publishing.

5.2 Thin film characteristics

The images in Figure 34 clearly demonstrate the difference between TEM grids with ALD and PECVD SiO_2 coatings as explained analytically in [PII]. Especially, TEM images in Figures 34c,d show an area of darker contrast forming around the nanoparticles, because they act as nucleation sites for the growth of SiO_2. These regions are a lot more distinct in PECVD SiO_2, as grains could be noticed as well [90], compared to more uniform ALD SiO_2.
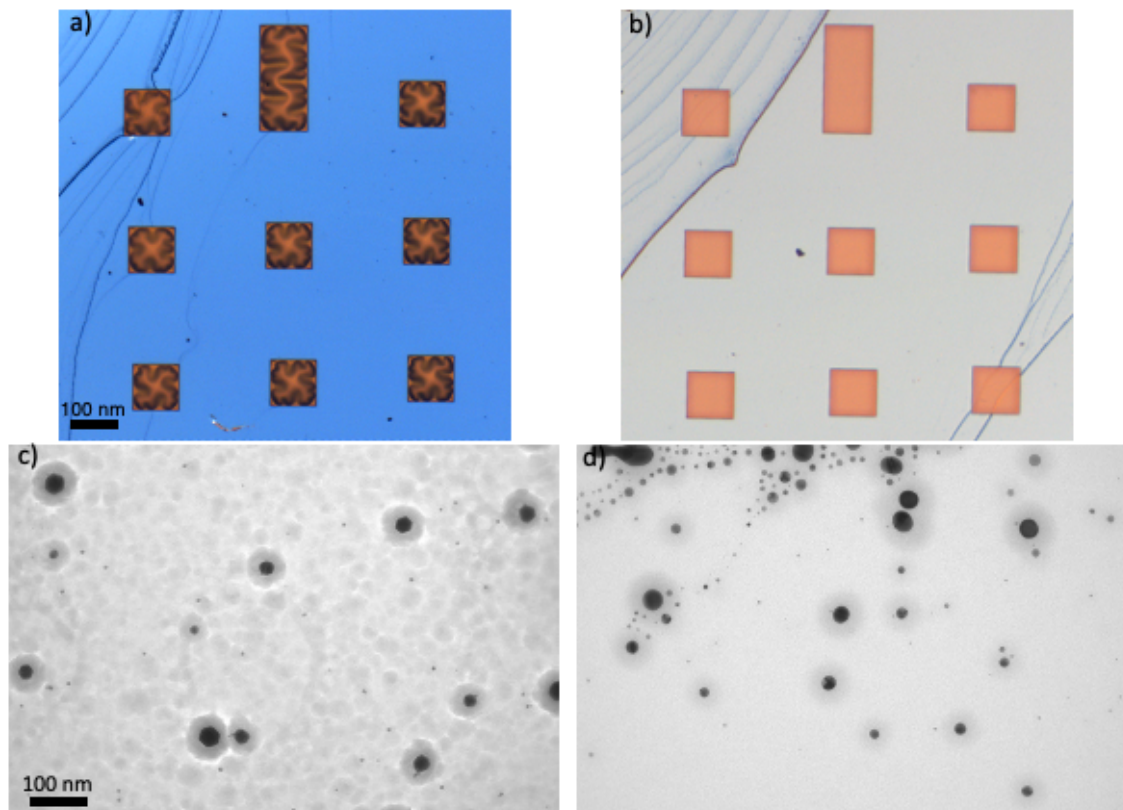
FIGURE 34 Optical microscope images of a TEM grid with SiO_2 deposited (a) by PECVD and (b) by ALD. TEM images of nanoparticles embedded in SiO_2 grown using (c) PECVD and (d) ALD. Modified with permission from [PII], Copyright 2022, AIP Publishing.

The properties of grown SiO_2 films on Si substrate were investigated by ToF-ERDA and XRR measurements. Coincidence time-of-flight and energy data (Figure 17) gave the elemental composition of the samples. ToF-ERDA depth profiles showed that the as-deposited PECVD sample (Figure 35a) was nearly stoichiometric SiO_2 (O/Si=2.06$\pm$0.02) while the annealed PECVD sample (Figure 35b) was slightly oxygen poor SiO_2 (O/Si=1.88$\pm$0.02). Both films contained some amount of impurities, including hydrogen, nitrogen, carbon, and sodium. However, there is a difference in the amount of hydrogen impurity in the films. The as-deposited film has a significant amount of hydrogen (7.6 at.%), but it reduces significantly in the annealed film (<0.1 at.%). In addition, gold is naturally de-

tected because of the presence of gold nanoparticles inside the SiO_2.

ALD samples have similar behaviour. The as-deposited ALD sample (Figure 36a) was closely stoichiometric SiO_2 (O/Si=2.07±0.02). The amount of hydrogen was still significant (6.5 at.%), while small amount of other impurities (less than 1 at.%) was also detected [PII]. The annealed ALD sample (Figure 36b) was stoichiometric SiO_2 (O/Si=1.97±0.02), but hydrogen concentration was again significantly reduced (<0.2 at.%). The number of gold nanoparticles embedded inside SiO_2 was always calculated based on the atomic concentrations of gold (1.4×10^7-1.1×10^8 nanoparticles/cm^2) showing that nanoparticles had a low average areal density covering less than 0.1% of the area.

In Figures 37a,b, XRR curves are shown for Si/50 nm ALD SiO_2/50 nm PECVD SiO_2 and Si/50 nm ALD SiO_2 samples, respectively. The information about PECVD layer was obtained using firstly ALD-only fit and then we fit the PECVD layer. The density of PECVD SiO_2 in the first sample was measured to be 2.20±0.06 g/cm^3, while the density of ALD SiO_2 in the second sample was 2.14±0.05 g/cm^3. The roughness was 2.21±0.10 nm and 0.21±0.09 nm, respectively. While the measured thickness for ALD SiO_2 was 56.4±0.7 nm, close to the estimated, the thickness of PECVD SiO_2 was 41.0±0.9 nm. This value may not be so accurate because basically the two films in the first sample are the same material and it is difficult to be distinguished depending on their thickness.
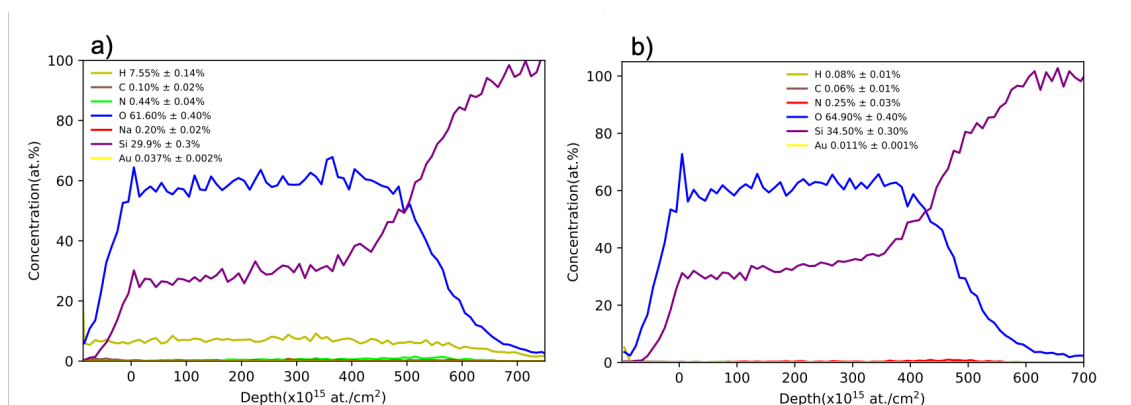

FIGURE 35 ToF-ERDA depth profiles of Si/50 nm PECVD SiO_2/NPs/50 nm PECVD SiO_2 (a) as-deposited sample and (b) annealed sample. Reprinted with permission from [PII], Copyright 2022, AIP Publishing.
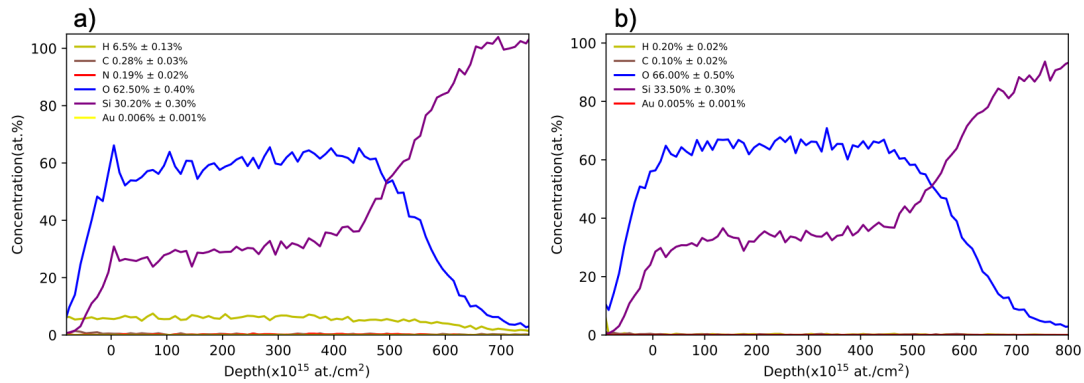
FIGURE 36   ToF-ERDA depth profiles of Si/50 nm ALD SiO$_2$/NPs/50 nm ALD SiO$_2$ (a) as-deposited sample and (b) annealed sample. Reprinted with permission from [PII], Copyright 2022, AIP Publishing.
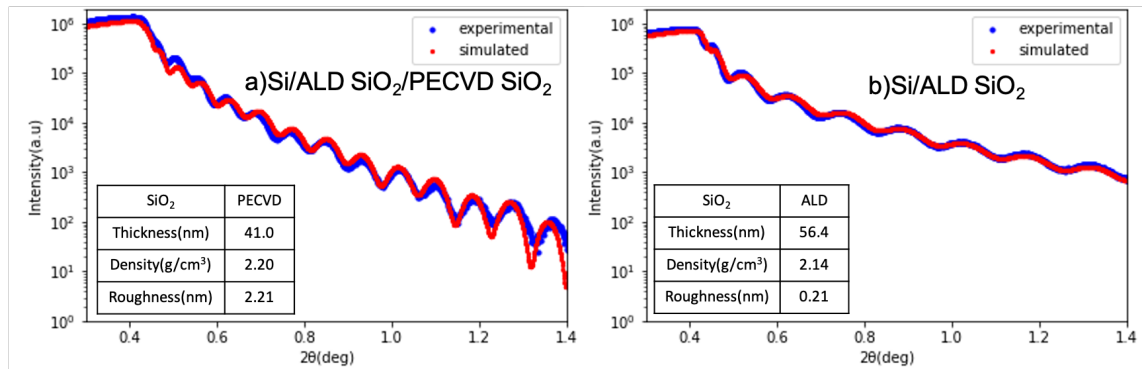
FIGURE 37   Measured and simulated XRR curves of (a) Si/50 nm ALD SiO$_2$/50 nm PECVD SiO$_2$ as-deposited sample and (b) Si/50 nm ALD SiO$_2$ as-deposited sample. In each graph, there is a table with the measured quantities for each film. Reprinted with permission from [PII], Copyright 2022, AIP Publishing.

5.3   Elongation of nanostructures

The elongation of the embedded nanoparticles in SiO$_2$ was studied by applying several fluences between 10^{13} and 5×10^{14} ions/cm^2. The initial spherical nanoparticles have been categorized in the ranges of 5 nm, i.e 5-10 nm, 10-15 nm, 15-20 nm, etc. A variation in the change of the nanoparticles shape is observed, which is in compliance with previous studies [11]. The elongation ratios with uncertainties calculated by the standard deviation method are shown in Tables 2 and 3. Those nanoparticles, that showed the maximum elongation ratio in each range before and after the irradiation, are shown in Figures 39-42 indicatively for two fluences (the other fluences are analytically shown in [PII]). A comparison between ALD and PECVD samples elongation ratio is shown at Figure 38.

TABLE 2   Length/width ratio for nanoparticles embedded in annealed (ann.) and as-deposited (as-dep.) PECVD SiO$_2$ samples regarding the initial diameter and fluence. Modified with permission from [PII], Copyright 2022, AIP Publishing.

	5×10^{14}(an.)	5×10^{13}(an.)	5×10^{13}(as-dep.)	10^{13}(an.)	10^{13}(as-dep.)
5-10 nm	1.0±0.0	1.03±0.03	1.12±0.12	1.02±0.02	1.0±0.0
10-15 nm	1.0±0.0	1.43±0.22	1.37±0.29	1.16±0.12	-
15-20 nm	1.52±0.52	1.78±0.38	1.53±0.30	1.19±0.09	1.36±0.32
20-25 nm	2.24±0.70	2.06±0.35	1.62±0.38	1.18±0.10	1.47±0.45
25-30 nm	2.12±0.52	2.00±0.38	1.73±0.32	1.12±0.06	1.43±0.38
30-35 nm	1.99±0.54	1.73±0.34	1.60±0.29	1.09±0.07	1.14±0.14
35-40 nm	1.88±0.43	1.48±0.17	1.58±0.26	1.03±0.03	1.18±0.18
40-45 nm	-	1.21±0.13	1.50±0.39	1.02±0.02	1.21±0.20
45-50 nm	1.46±0.05	1.11±0.11	1.24±0.20	1.0±0.0	1.05±0.05
50-60 nm	1.30±0.30	1.0±0.0	1.0±0.0	1.0±0.0	1.0±0.0
60-70 nm	1.0±0.0	1.0±0.0	1.0±0.0	1.0±0.0	1.0±0.0

TABLE 3 Length/width ratio for nanoparticles embedded in annealed (ann.) and as-deposited (as-dep.) ALD SiO_2 samples regarding the initial diameter and fluence. Modified with permission from [PII], Copyright 2022, AIP Publishing.

|	5×10^{14}(an.)	10^{14}(as-dep.)	5×10^{13}(an.)	5×10^{13}(as-dep.)	10^{13}(an.)	10^{13}(as-dep.)
5-10 nm	1.0±0.0	-	1.15±0.15	1.0±0.0	1.12±0.12	1.06±0.06
10-15 nm	1.0±0.0	-	1.31±0.24	1.26±0.20	1.32±0.14	1.24±0.12
15-20 nm	3.79±1.82	1.53±0.0	1.33±0.15	1.37±0.21	1.34±0.19	1.16±0.09
20-25 nm	3.74±1.61	1.90±0.05	1.23±0.14	1.37±0.23	1.21±0.11	1.10±0.08
25-30 nm	2.79±1.43	2.36±0.17	1.16±0.08	1.40±0.17	1.12±0.10	1.07±0.07
30-35 nm	2.84±1.03	2.39±0.26	1.05±0.05	1.39±0.12	1.08±0.07	1.04±0.04
35-40 nm	2.86±1.25	1.88±0.05	1.03±0.03	1.25±0.18	1.03±0.03	1.05±0.05
40-45 nm	2.87±0.89	1.40±0.25	1.0±0.0	1.10±0.05	1.0±0.0	1.0±0.0
45-50 nm	2.33±0.53	1.15±0.04	1.0±0.0	1.07±0.07	1.0±0.0	1.0±0.0
50-55 nm	2.07±0.74	-	1.0±0.0	1.0±0.0	1.0±0.0	1.0±0.0
55-60 nm	1.49±0.49	-	1.0±0.0	1.0±0.0	1.0±0.0	1.0±0.0
60-65 nm	1.29±0.26	-	1.0±0.0	1.0±0.0	1.0±0.0	1.0±0.0
65-70 nm	1.04±0.04	-	1.0±0.0	1.0±0.0	1.0±0.0	1.0±0.0
70-80 nm	1.0±0.0	-	1.0±0.0	1.0±0.0	1.0±0.0	1.0±0.0
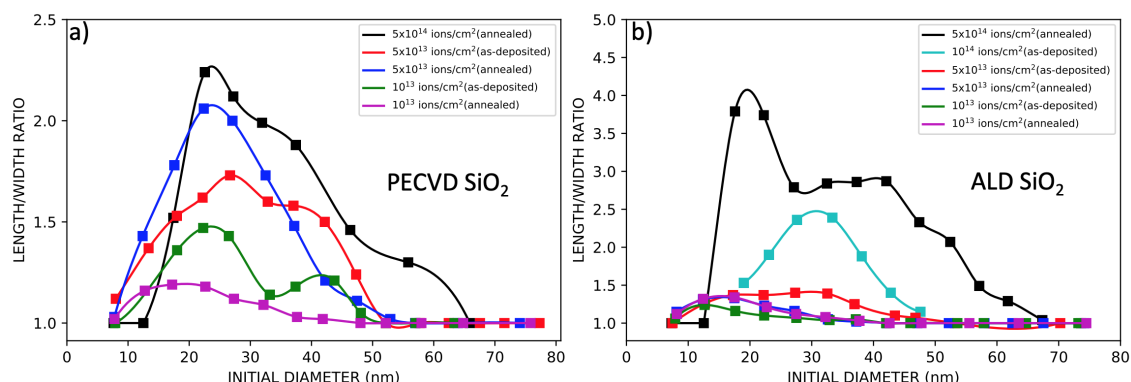
FIGURE 38   Representation of the average ratio (length/width) vs initial diameter of the elongated nanoparticles after 50 MeV ^{127}I irradiation at fluences between 10^{13} and 5×10^{14} ions/cm^2, which are embedded in (a) PECVD SiO$_2$ and (b) ALD SiO$_2$. The uncertainties are left out from image for clarity (shown in Tables). Reprinted with permission from [PII], Copyright 2022, AIP Publishing.

Single nanoparticles irradiated at fluence 5×10^{13} ions/cm^2 are shown in Figures 39 and 40. The elongation ratio shows to be similar for the as-deposited and annealed samples at the same fluence. However, the nanoparticles embedded in PECVD SiO$_2$ achieved slightly higher elongation ratio than nanoparticles embedded in ALD SiO$_2$ for fluences $\leq 5 \times 10^{13}$ ions/cm^2.

FIGURE 39   TEM images of nanoparticles sandwiched between two 50 nm PECVD SiO$_2$ layers (annealed after the deposition). The samples were irradiated with ^{127}I at fluence of 5×10^{13} ions/cm^2, and imaged before (left) and after (right) the irradiation. Modified with permission from [PII], Copyright 2022, AIP Publishing.

FIGURE 40   TEM images of nanoparticles sandwiched between two 50 nm ALD SiO$_2$ layers (as-deposited). The samples were irradiated with ^{127}I irradiated at fluence of 5×10^{13} ions/cm^2, and imaged before (left) and after (right) the irradiation. Modified with permission from [PII], Copyright 2022, AIP Publishing.

On the other hand, at the highest fluence (5×10^{14} ions/cm^2) the as-deposited PECVD and ALD sample windows did not resist irradiation as most of the windows broke during the irradiation. The annealed PECVD sample suffered as well as only a few nanoparticles could be traced after the irradiation. The problem was overcome by collecting images from nanoparticles which had not been imaged prior to the irradiation. The volume of the pre-imaged nanoparticles was found to be slightly smaller (5-10%) after the irradiation. The initial diameter of the non-imaged nanoparticles before the irradiation was found by assuming their shape as cylinder and comparing it with their spherical volume before the irradiation. However, this problem was not appeared in annealed ALD sample, which had intact windows.

In Figures 41 and 42, the nanoparticles having the highest elongation ratio in each size are shown. Between the two deposition techniques, ALD samples achieve greater elongation ratio than PECVD samples. However, some of those nanorods inside ALD SiO$_2$ were split into smaller fragments after excessive elongation [60].

It is clear that nanoparticles elongation ratio increases with increasing fluence (Figure 43) and the biggest nanoparticles also modify. Moreover, the Figure 43 denotes that ALD samples have higher threshold fluence for larger elongation than PECVD and the smaller nanoparticles elongate a little more in both cases.
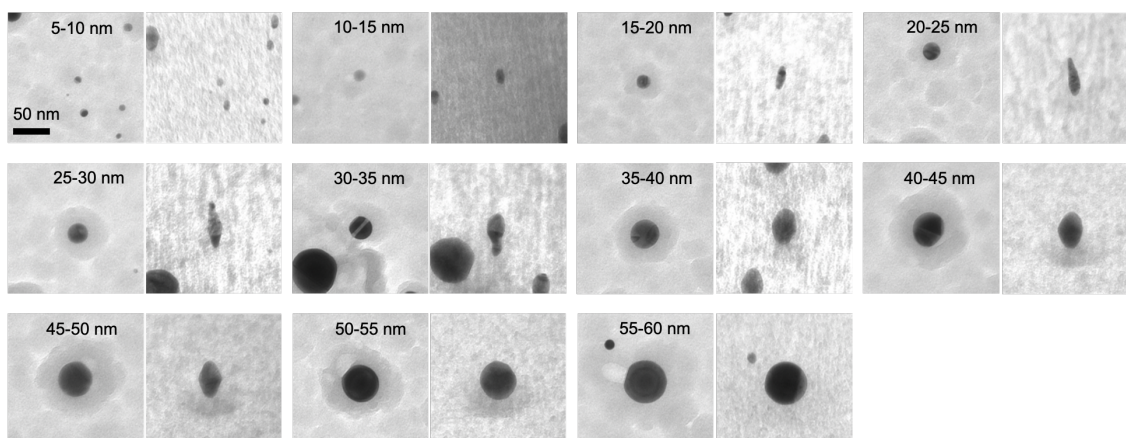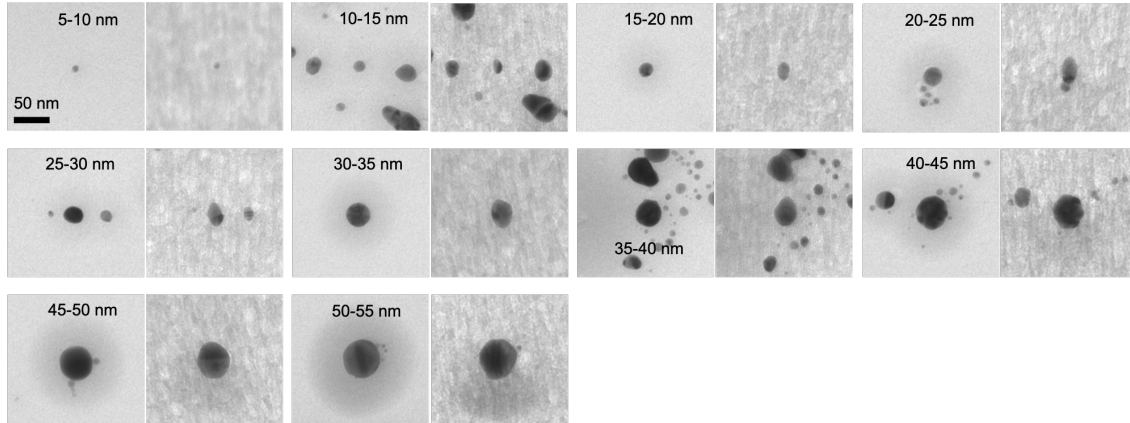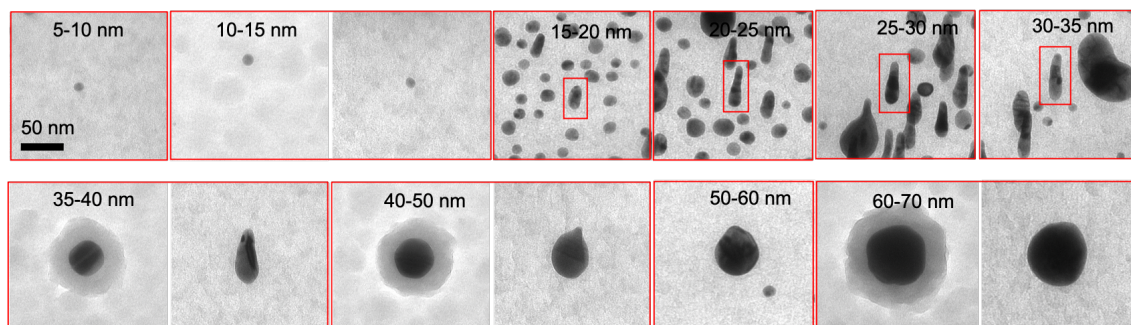
FIGURE 41   TEM images of nanoparticles sandwiched between two 50 nm PECVD SiO_2 layers (annealed after the deposition). The samples were irradiated with ^{127}I at fluence of 5×10^{14} ions/cm^2, and imaged before and after the irradiation. Red outline includes either a pair of nanoparticles before (left) and after (right) the irradiation or only nanoparticles after the irradiation. Modified with permission from [PII], Copyright 2022, AIP Publishing.

According to the results, the two factors, which mainly affect the elongation, are the irradiation fluence and the initial size of the nanoparticle. While the lower fluences ($\leq5\times10^{13}$ ions/cm^2) favour the elongation of nanoparticles smaller than 50 nm, the higher fluences ($\geq10^{14}$ ions/cm^2) can elongate bigger nanoparticles as well because of the enough high deposited energy. However, when the smallest nanoparticles (<15 nm) are irradiated with higher fluences, they start to shrink instead of elongate, and reform towards a spherical shape or complete disintegration. This shrinkage is because of the high amount of irradiation preventing them from further elongation. As a result, the larger atoms absorb the constituent atoms of the disintegrating nanoparticles (Ostwald ripening) [91].

The nanoparticle threshold diameter for elongation depends as well on the ion track diameter. Nanoparticles with diameter smaller than the ion track diameter can elongate in much lower rate than the bigger ones or cannot elongate at all [54]. Additionally, the track diameter affects the smallest width which an elongated nanoparticle can achieve. Both threshold diameter and minimum elongation width are affected as well by the metal which the nanoparticle consists of. This dependence is more pronounced in threshold diameter for elongation which always differs between different metals. SAXS (Small Angle X-ray Scattering) measurements by Mota-Santiago et al [11] revealed that SiO_2 irradiated with 185 MeV Au beam has an ion track of 10.8 nm in diameter. In our case, the diameter of the smallest nanoparticles that can elongate and the smallest elongation width were found to be 7–8 nm approximately. Furthermore, the elongation of so small nanoparticles is affected by their small size and small chance that they will be hit by a significant number of ions (8–40 ion hits/10^{13}–5×10^{13} ions/cm^2).

According to Rizza et al [7], there is a relation between the initial particles size and their deformation path in SiO_2. This relation is clear at the highest applied fluence, where nanoparticles of different initial diameter deform in different way [PII]. Therefore, the smallest nanoparticles (<15 nm), either fully disintegrate and disappear, or partially disintegrate but maintain their spherical shape. Nanoparticles with diameter between 15 and 45 nm totally melt during
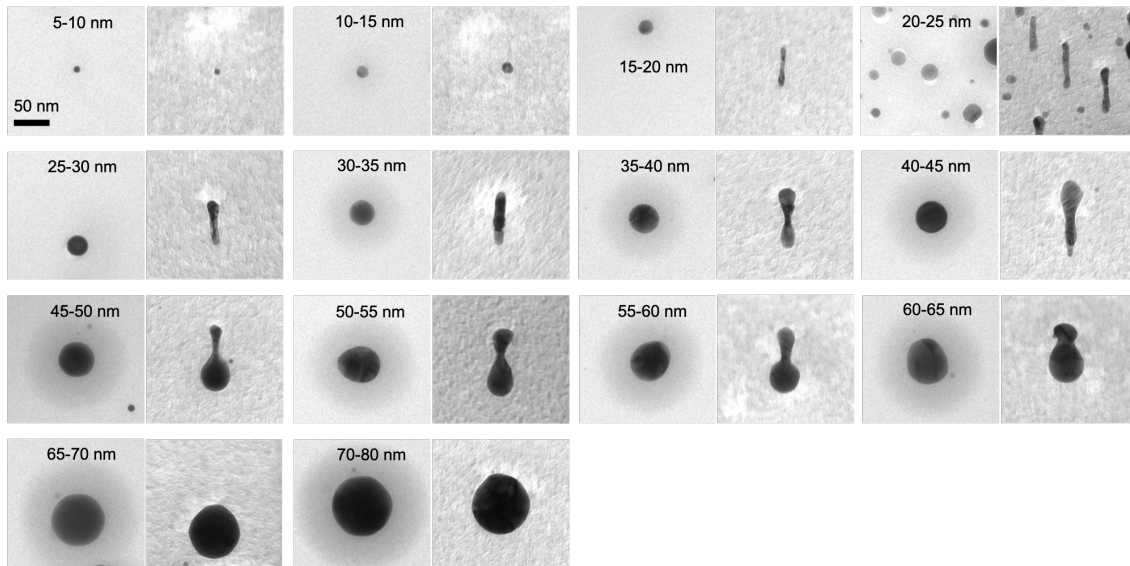
FIGURE 42   TEM images of nanoparticles sandwiched between two 50 nm ALD SiO$_2$ layers (annealed after the deposition). The samples were irradiated with ^{127}I at fluence of 5×10^{14} ions/cm^2, and imaged before (left) and after (right) the irradiation. Modified with permission from [PII], Copyright 2022, AIP Publishing.

ion impact, transforming into nanorods in the direction of the ion beam. They are partially molten at the range from 45 to 65 nm, and the elongation occurs as an elongated part attached to a sphere. Finally, because the ion energy is insufficient to melt bigger nanoparticles (>65 nm), the deformation is negligible. In Rizza's work [7], nanoparticles up to 30 nm in diameter entirely melted, but in our study, nanoparticles up to 45 nm in diameter completely melt because they clearly transform to nanorods. This observation is most likely due to the different composition of the samples and the different irradiation conditions. Regarding the composition of the samples, SiO$_2$ does not have to be hundreds of nanometers thick like in earlier studies [7, 11, 50, 92] in order to achieve elongation.

     Since there is a difference in elongation ratio between SiO$_2$ deposited by ALD and PECVD, the deposition technique of SiO$_2$ affects the elongation. On the one hand, nanoparticles embedded in ALD SiO$_2$ have higher elongation ratio than PECVD SiO$_2$ at the fluence of 5×10^{14} ions/cm^2. On the other hand, the opposite occurs at lower fluences. The fact that PECVD SiO$_2$ is denser than the ALD SiO$_2$ and the presence of grains in PECVD SiO$_2$ may give an explanation to this phenomenon. The denser the irradiated material is, the greater the deposited energy is in this and consequently greater elongation takes place. Except for the different overall density between the two types of SiO$_2$ obtained by XRR measurements, the dark spots around the nanoparticles can indicate areas of higher density. Since these areas are much more pronounced in PECVD SiO$_2$ than in ALD SiO$_2$, this layer has such a density forcing the nanoparticle to elongate more in PECVD SiO$_2$. However at higher fluences, these dark halos jointly with the grains appearing in the PECVD SiO$_2$ lead to greater damage preventing from greater elongation. As a result, more deposited energy is needed for nanoparti-
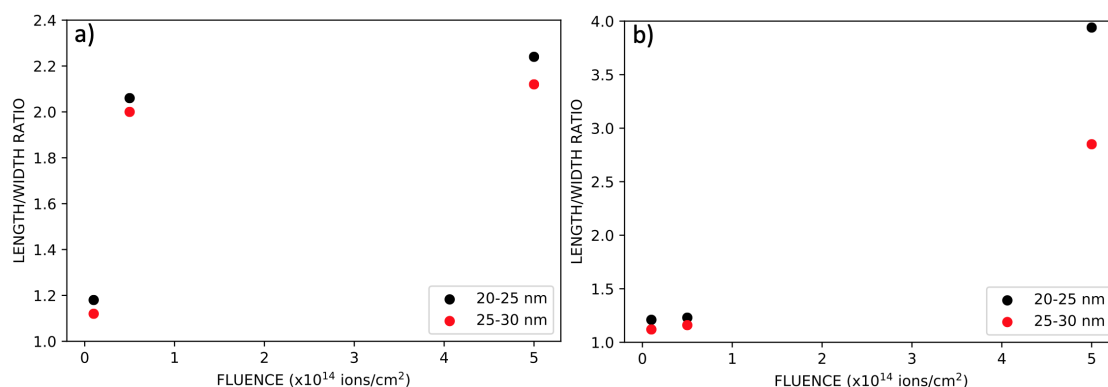
FIGURE 43   Evolution of the elongation ratio with increasing fluence for two nanoparticle size in (a) PECVD SiO$_2$ and (b) ALD SiO$_2$. Reprinted with permission from [PII], Copyright 2022, AIP Publishing.

cles embedded in ALD SiO$_2$ to achieve the same elongation ratio as in PECVD. But the nanoparticles embedded in PECVD SiO$_2$ elongate more quickly and reach saturation. On the other hand, for ALD the degree of elongation is significantly higher (two times) at 5×10^{14} ions/cm^2 fluence compared to 10^{14} ions/cm^2 fluence and to PECVD sample at 5×10^{14} ions/cm^2 fluence.

      Finally, the annealing after the deposition and prior the irradiation does not affect significantly the elongation at lower fluences. However, at 5×10^{14} ions/cm^2 fluence, the as-deposited sample does not withstand irradiation with almost all the windows broken. This is due to the fact that the annealing process makes the material stronger against the plastic deformation during the irradiation and not to break resulting in more durable TEM grids.

6 IRRADIATION EFFECTS ON SHI IRRADIATED NANORODS EMBEDDED IN SiO$_2$

6.1 Synthesized nanorods

Ion beam shaping has been applied mostly to initially spherical nanoparticles and it is worth to investigate the irradiation impact on embedded nanorods as well. Firstly, chemically synthesized Au nanorods were embedded in 100 nm thick PECVD SiO$_2$. The samples were irradiated with 50 MeV ^{127}I^{9+} under 45° at 10^{14} ions/cm^2 fluence. By this way, we managed to identify the same nanorod before and after the irradiation.

In this study, the swift heavy ion beam irradiation reshaped nanorods differently depending on their initial size. The differences can be classified into three categories. In the first category, the nanorods were totally reshaped and obtained again the same shape but along the ion beam direction (Figure 44). As a result, they were re-oriented along the ion beam direction. The initial size of the nanorods that were reshaped and aligned with the ion beam varied with diameter from 20 to 31 nm and length from 32 to 63 nm.

FIGURE 44   TEM images of single nanorods imaged before (left) and after (right) the irradiation. The nanorods were embedded in 100 nm PECVD SiO$_2$ and irradiated with 50 MeV ^{127}I at 10^{14} ions/cm^2 and they "rotate" along the ion beam direction. (a) Initial length = 34.3 nm and diameter = 21.2 nm,(b) length = 38.5 nm and diameter = 20.3 nm and (c) length = 53 nm and diameter = 32 nm. Modified with permission from [PI], Copyright 2022, AIP Publishing.

In the second category, protrusions/spikes have been created on the nanorods

along the ion beam direction. The nanorods with diameter varying between 25 nm and 44 nm and length varying between 52 nm and 86 nm (Figure 45) had this behaviour. It seems that these nanorods were initially shrinking and only after their size reached the range of sizes that are seen to rotate with the beam, the rotation began. But this process remained incomplete as the remaining fluence was not high enough to fully reshape the nanorods. In the same range of size as in category 2, quite a number of nanorods remained unchanged (Figure 46). These belong to the third category, although their size had somewhat shrunk due to significant ion fluence. This fact implies that this procedure of creating spikes/protrusions is more random.
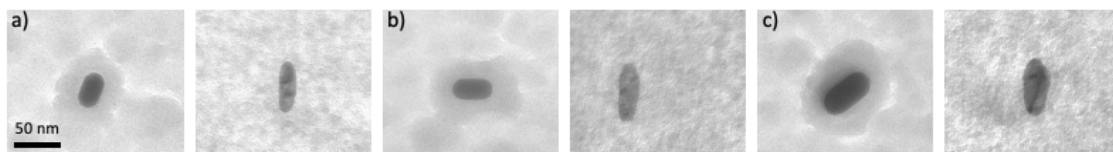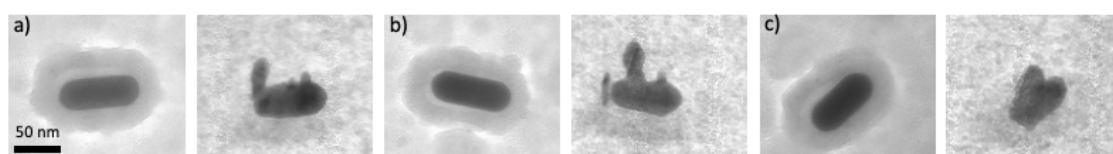

FIGURE 45   TEM images of single nanorods imaged before (left) and after (right) the irradiation. The nanorods were embedded in 100 nm PECVD SiO_2 and irradiated with 50 MeV ^{127}I at 10^{14} ions/cm^2 and the ion beam creates protrusions/spikes on them. (a) Initial length = 81.5 nm and diameter = 32.4 nm),(b) length = 82.2 nm and diameter = 33 nm and (c) length = 75.1 nm and diameter = 37.9 nm. Modified from [PIII] under the license CC BY 3.0.
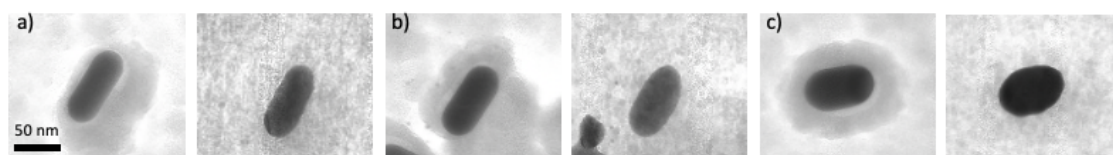
FIGURE 46   TEM images of single nanorods imaged before (left) and after (right) the irradiation. The nanorods were embedded in 100 nm PECVD SiO_2 which were irradiated with 50 MeV ^{127}I at 10^{14} ions/cm^2 and remained unchanged. (a) Initial length = 86 nm and diameter = 35 nm,(b) length = 78.2 nm and diameter = 37.4 nm and (c) length = 69.9 nm and diameter = 42 nm. Modified from [PIII] under the license CC BY 3.0.

6.2   Nanolithography nanorods

The experiments described above proved that elongation of nanostructures with shape other than spherical is possible and the shape is limited to those commercially available. Nanorods of different size and orientation were embedded inside the ALD SiO_2 and were irradiated with 50 MeV ^{127}I^{9+} at 3 fluences, 5×10^{13}, 10^{14} and 2×10^{14} ions/cm^2. In Figure 47, images from the patterns and the nanorods created by HIM are shown before and after the irradiation. The as-fabricated

nanorods have different orientation but after the irradiation, they are aligned along the ion beam direction.

FIGURE 47   TEM images of HIM fabricated nanorods embedded in 100 nm ALD SiO$_2$ and irradiated with 50 MeV ^{127}I at 5×10^{13} ions/cm^2. Image (a) before and (b) after 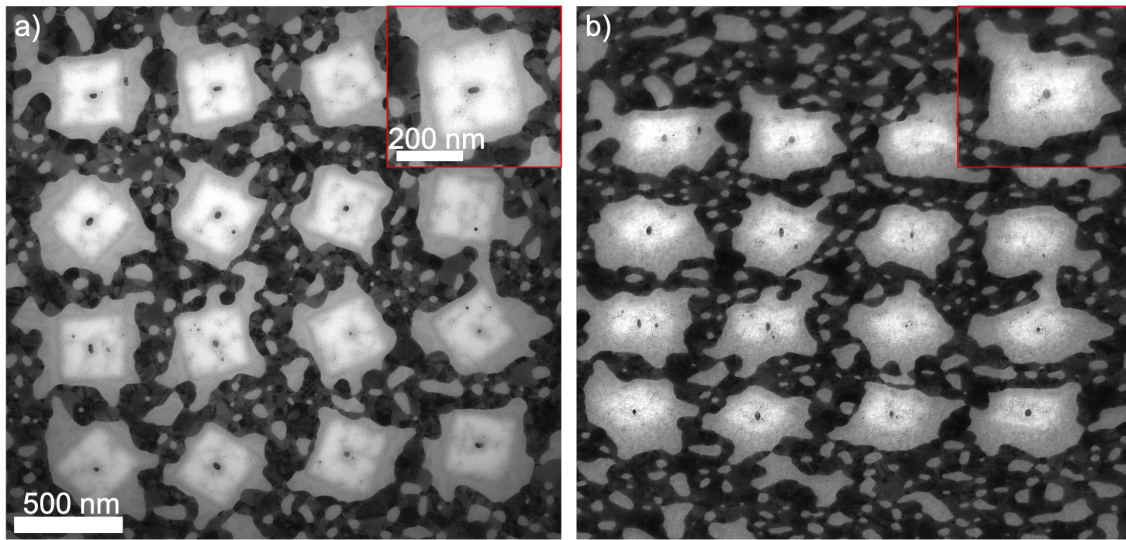the irradiation. The sample was tilted $45°$ in (b). The inset magnified images show a nanorod before and after the irradiation. Modified from [PIII] under the licence CC BY 3.0.

At 5×10^{13} ions/cm^2 fluence, the irradiated nanorods had obtained different shape depending on their initial size. The smaller nanorods were re-oriented along the ion beam direction. However, some nanorods were not affected much and kept their shape, while the ion beam shaping was incomplete for others. In Figures 48a,b, nanorods of different size and orientation align along the ion beam direction after the irradiation. The nanorods that did not fully elongate along the ion beam direction are shown in Figures 48c-e. They turned to spheroids as they had started to elongate along the ion beam direction and at the same time shrink in the dimension perpendicular to that. Finally, in Figure 48f, a nanorod, which is bigger than the others and kept its original shape, is shown.

The same effect occurred at 10^{14} ions/cm^2 fluence with nanorods of different orientation aligned along the ion beam direction (Figures 48g-i). Due to the higher ion fluence, the nanorods had elongated more than at 5×10^{13} ions/cm^2. However, the biggest nanorod shown in Figure 48j did not elongate, only reduced in size after 10^{14} ions/cm^2 fluence.

At the highest applied fluence (2×10^{14} ions/cm^2), the smallest nanorods elongated along the ion beam direction but their elongation reached saturation (48k,l). The high energy deposition prevented them from elongating more than the lower fluences leading to disintegration in some cases because the third dimension of the nanorod is close to 15 nm.

5x10¹³ ions/cm²

10¹⁴ ions/cm²
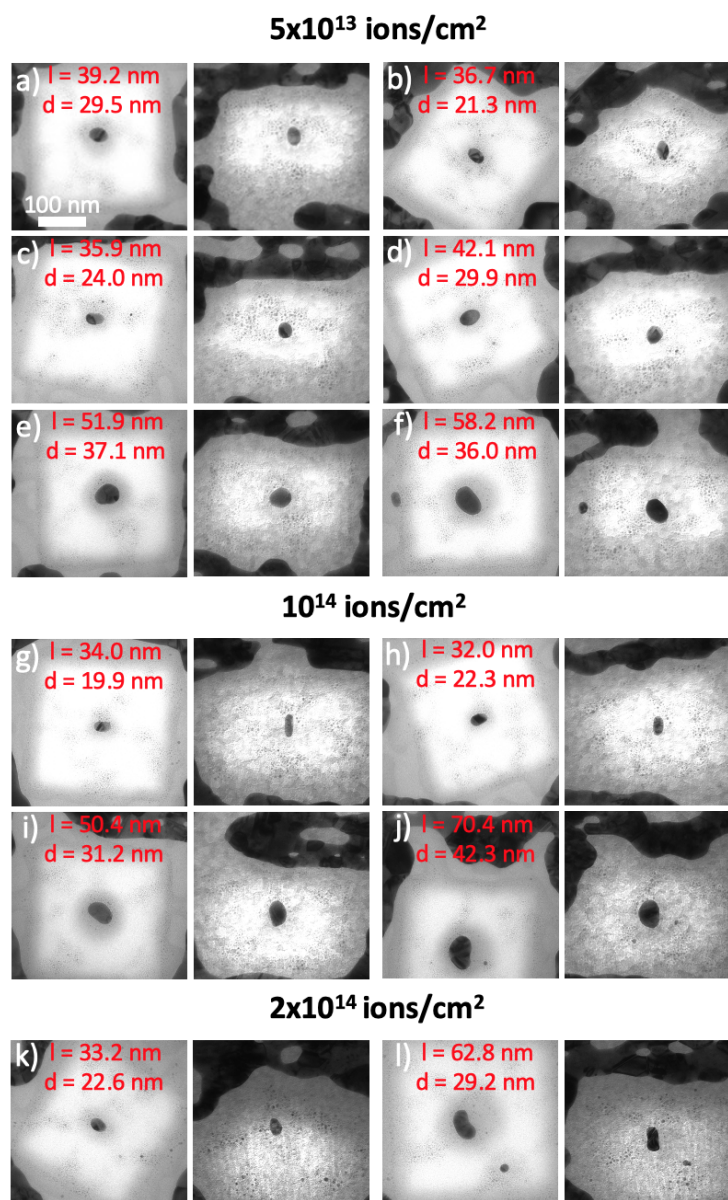
2x10¹⁴ ions/cm²

FIGURE 48   TEM images of fabricated nanorods with different orientations embedded in 100 nm ALD SiO_2 before (left) and after (right) the irradiation with 50 MeV ^{127}I at fluences 5×10^{13} ions/cm²–2×10^{14} ions/cm². Modified from [PIII] under the licence CC BY 3.0.

6.2.1 MD simulations

Nanorods are initially aligned perpendicular to the ion beam direction in the simulation system. With 164 MeV ^{197}Au ions, the ion impacts hit the nanorod randomly creating, firstly, protrusions in those locations. After the first 15 ion impacts, the shape had incrementally changed to an asymmetrical spheroid with left side being more elongated. After 30 impacts, the initial perpendicular nanorod has been reshaped into a nanorod along the beam direction. The evolution of the irradiated nanorod is shown in Figure 49. With 50 MeV ^{127}I ion simulations,

the shape change was much slower than with Au ions because of the lower energy deposition (Figure 50). Comparing these results with the experimental, Figure 48e shows the nanorod in a state which corresponds to 25 ion impacts with 50 MeV ^{127}I ions. As the ion impacts increase, the nanorod turned to spheroid along the ion beam direction as shown in Figure 48c,d. Finally, the nanorod has completely reshaped along the ion beam direction as shown with 164 MeV ^{197}Au ions in Figure 49.
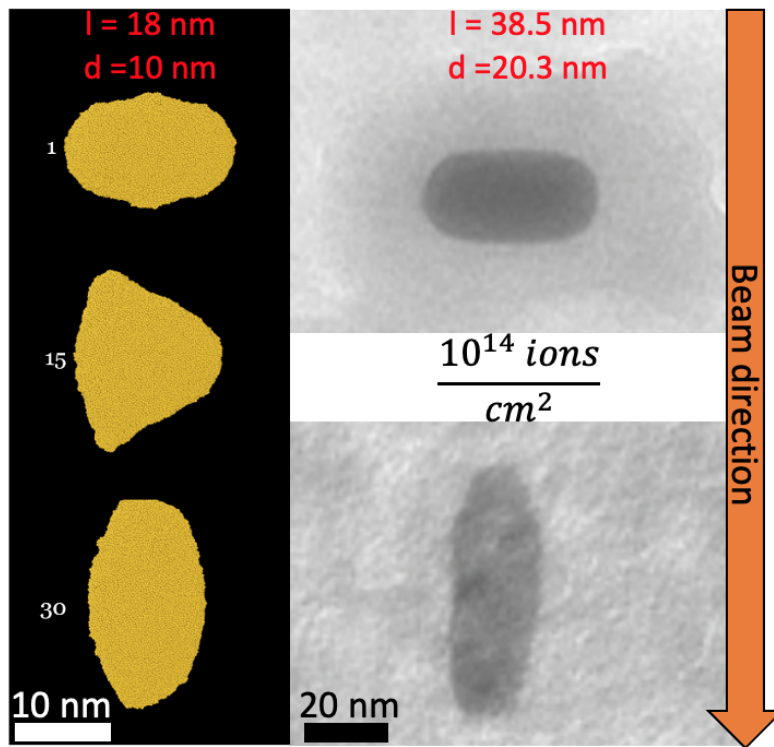
FIGURE 49   Left side: Nanoparticle shape after simulating 1, 15, and 30 impacts to random positions on the nanorod with 164 MeV ^{197}Au ions. Right side: Zoom in of the same nanorod as in Figure 44b. Modified with permission from [PI], Copyright 2022, AIP Publishing.
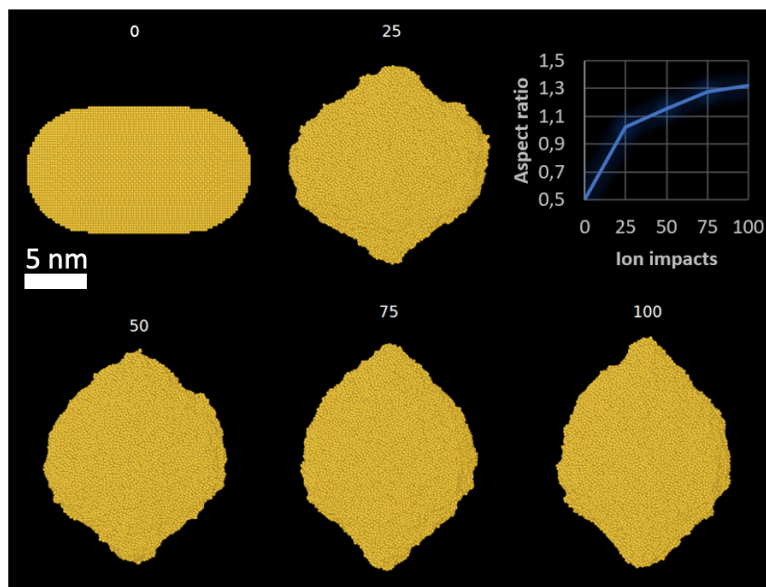
FIGURE 50   Nanorod shape after 0, 25, 50, 75, and 100 simulated 50 MeV ^{127}I ion impacts to the center of the nanorod (length = 18 nm and diameter = 10 nm). Reprinted with permission from [PI], Copyright 2022, AIP Publishing.

The same mechanism as previously reported by Leino et al [14] for spherical nanoparticles occurs during the shape change of a nanorod. From both simulations, we conclude that the molten nanorod expands into the tracks making the material flow into these. Small incremental shape changes accumulate resulting in growth along the ion beam direction and shrinking in others. Consequently, the nanorod gets aligned along the ion beam direction.

7 SHI IRRADIATION OF SPHERICAL METALLIC NANOPARTICLES EMBEDDED IN Al_2O_3 AND TiO_2

7.1 Irradiation effects on nanoparticles embedded in ALD Al_2O_3

Except for SiO_2, samples with Au and Ag nanoparticles embedded in Al_2O_3 were created in order to investigate the ion beam shaping. The thickness and the refractive index of the deposited Al_2O_3 film was measured by spectroscopic ellipsometry (SOPRA GES 5E) equipped with a Xe lamp (75 W). Al_2O_3 film had 100.4 ± 0.6 nm thickness and its refractive index was measured to be 1.66. Detailed composition analysis performed by Time-of-Flight Elastic Recoil Detection Analysis (ToF-ERDA) [72] for Al_2O_3 is found in [93]. The samples were irradiated with 50 MeV $^{127}I^{9+}$ under $45°$ at fluences from 5×10^{13} to 2×10^{14} ions/cm^2.

In Figures 51 and 52 ,the elongation of spherical Au nanoparticles is shown for 5×10^{13} and 2×10^{14} ions/cm^2 fluences, respectively. As the fluence increases, the elongation ratio increases as well (Figure 53). Al_2O_3 presents slightly higher elongation ratio than SiO_2 for the initial size range from 15 to 30 nm after 5×10^{13} ions/cm^2 fluence (Figure 54). At higher fluences, we cannot compare them because SiO_2 samples were irradiated with higher fluence (5×10^{14} ions/cm^2). However, the biggest difference in elongation ratio was observed for particles with initial size between 15 and 25 nm. Then the nanoparticles embedded in SiO_2 elongated almost twice as much compared to Al_2O_3. For bigger sizes, the difference in ratio was less than 1.

FIGURE 51   TEM images of Au elongated nanoparticles sandwiched between two 50 nm ALD Al_2O_3 layers and irradiated with 50 MeV ^{127}I at 5×10^{13} ions/cm^2. The same particles were imaged before (left) and after (right) the irradiation. Reproduced from [PIII] under the license CC BY 3.0.

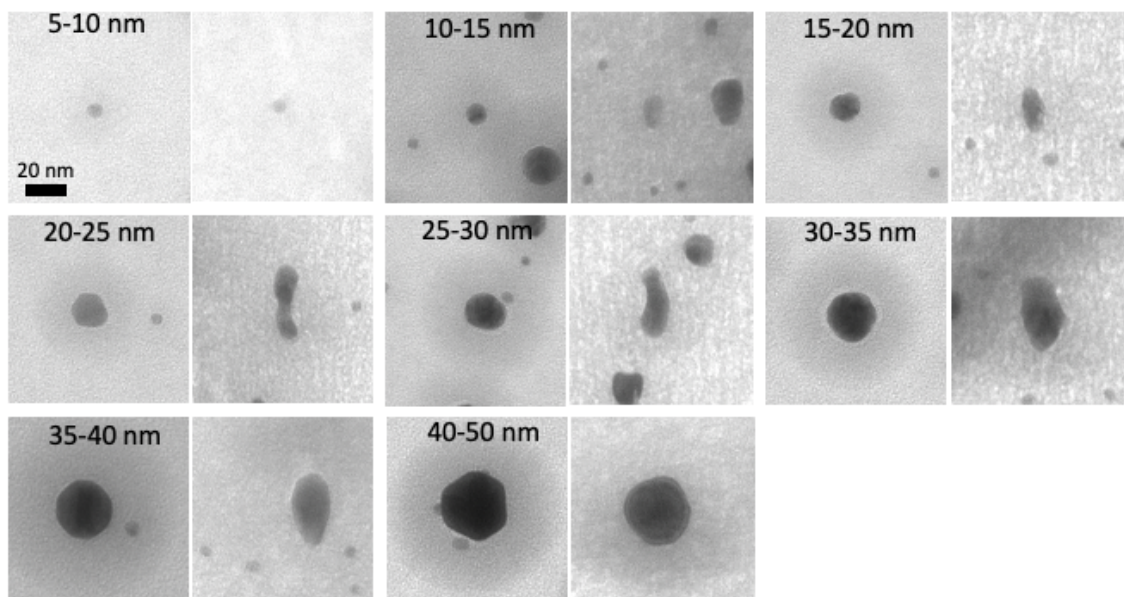FIGURE 52   TEM images of Au elongated nanoparticles sandwiched between two 50 nm ALD Al_2O_3 layers and irradiated with 50 MeV ^{127}I at 2×10^{14} ions/cm^2. The same particles were imaged before (left) and after (right) the irradiation. Reproduced from [PIII] under the license CC BY 3.0.
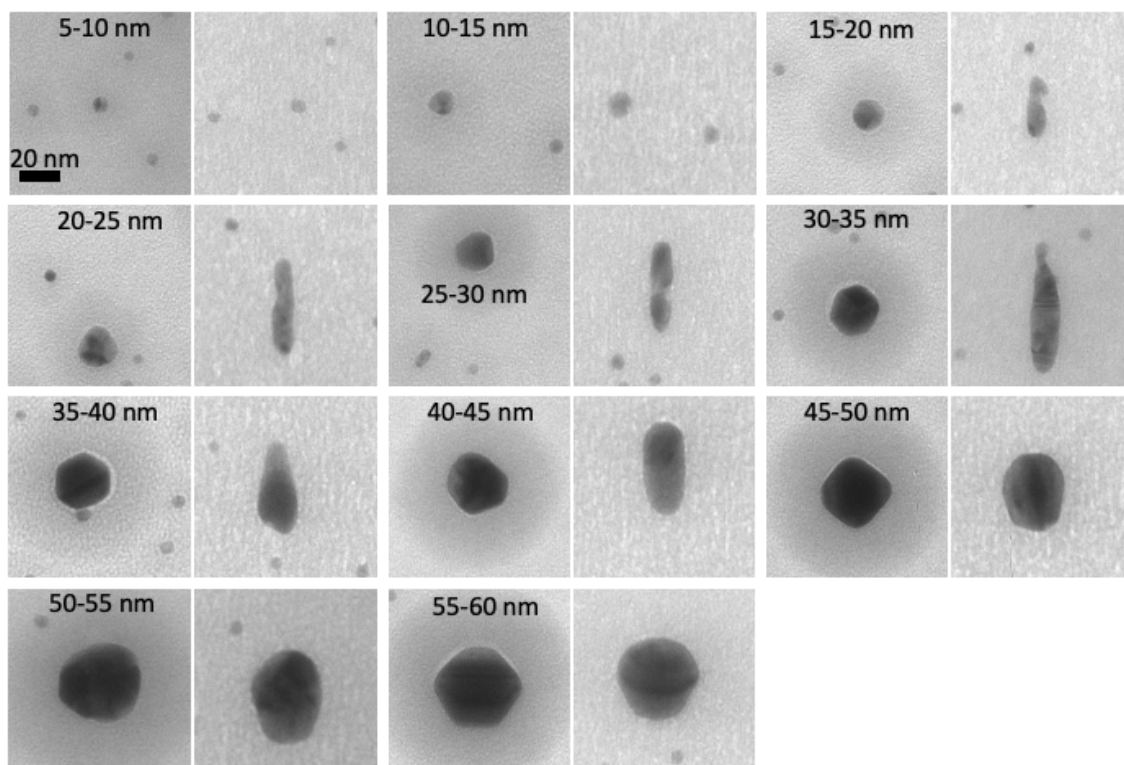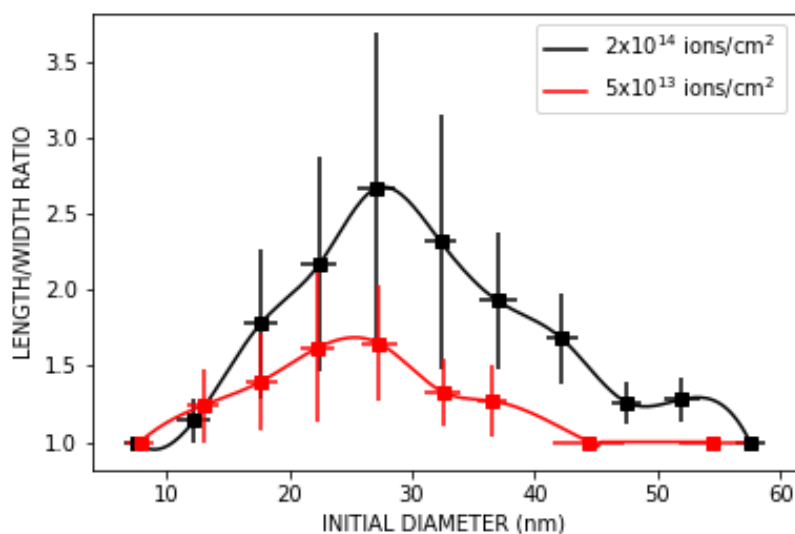
FIGURE 53   Elongation ratio vs initial diameter for the nanoparticles embedded in Al_2O_3 and irradiated with two different fluences.

It is obvious that Au nanoparticles embedded in Al_2O_3 can elongate with comparable ratio as in SiO_2. Based on the study of Mota-Santiago et al [11], the difference in nanoparticles elongation ratio between two host materials (SiO_2 and Si_3N_4 in that case) is caused by the electron-phonon coupling and the thermal conductivity of the host matrix. As a result, the higher electron-phonon coupling of SiO_2 ($g_{SiO_2} = 1.25 \times 10^{19}$ Wm^{-3}K^{-1}, $g_{Si_3N_4} = 0.52 \times 10^{19}$ Wm^{-3}K^{-1} [50]) denotes greater energy transfer from the electronic subsystem to the lattice. However, the smaller thermal conductivity of SiO_2 ($k_{SiO_2} = 3$ Wm^{-1}K^{-1}, $k_{Si_3N_4} = 11$ Wm^{-1}K^{-1} [50]) leads to slower cooling resulting in more material flow into the ion track. Consequently, Au nanoparticles elongate more in SiO_2 than in Si_3N_4. In our case, Al_2O_3 has lower electron-phonon coupling ($g_{Al_2O_3} = 0.48 \times 10^{19}$ Wm^{-2}K^{-1} [94]) and higher thermal conductivity ($k_{Al_2O_3} = 30$ Wm^{-1}K^{-1} [95]) than SiO_2. Nevertheless, the elongation ratio does not differ much between them.
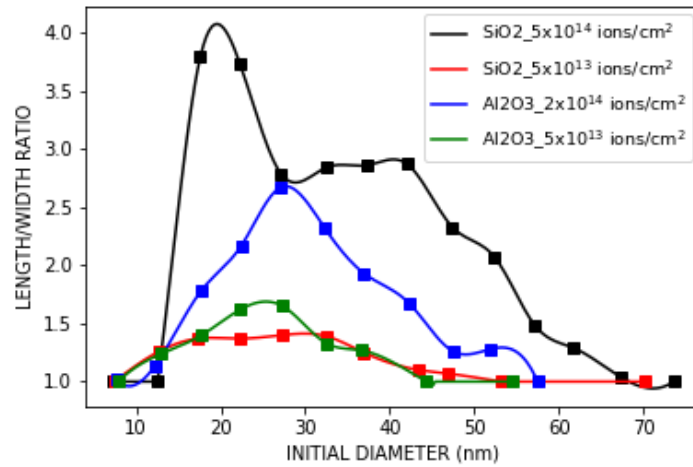
FIGURE 54   Comparison of the elongation ratio vs initial diameter for the nanoparticles embedded either in ALD SiO_2 or ALD Al_2O_3. The uncertainties are left out from the image for clarity. Reproduced from [PIII] under the license CC BY 3.0.

In the case of Ag nanoparticles, the observed elongation was small. In Figure 55, the elongation results for nanoparticles of different diameter are shown. For 2×10^{14} ions/cm^2 fluence, the nanoparticles achieve, in average, about 50% of the elongation ratio compared to the Au nanoparticles. The reason can be attributed to the higher energy density per atom to vaporize the gold compared to silver, which results in lower elongation width for gold [55].

FIGURE 55   TEM images of Ag elongated nanoparticles sandwiched between two 50 nm ALD Al_2O_3 layers and irradiated with 50 MeV ^{127}I at 2×10^{14} ions/cm^2. The same particles were imaged before (left) and after (right) the irradiation. Reproduced from [PIII] under the license CC BY 3.0.

7.2   Irradiation effects on nanoparticles embedded in ALD TiO_2

Although TiO_2 has already been subject to SHI irradiation to investigate the formation of ion track, there is no reported work about ion beam shaping of metallic nanoparticles embedded in this oxide. For this reason, Au and Ag spherical nanoparticles embedded between two 50 nm TiO_2 films deposited by ALD were irradiated with 50 MeV ^{127}I^{9+} under 45° with 2×10^{14} ions/cm^2 fluence.

Au nanoparticles embedded in TiO_2 are shown in Figure 56. The nanoparticles with a diameter less than 20 nm elongate visibly. However, nanoparticles with diameter bigger than that do not elongate at all or elongate only a little. According to O'Connell et al [45], 167 MeV Xe ions form an ion track of 5-6 nm diameter in TiO_2 compared to around 8 nm of the same ions in SiO_2. This fact which is due to the much lower electron-phonon coupling (g_{TiO_2} = 0.031×10^{19} $Wm^{-3}K^{-1}$ [45]) makes the larger nanoparticles elongate less, taking into consideration as well the higher thermal conductivity (k_{TiO_2} = 8.5 $Wm^{-1}K^{-1}$ [96]).

FIGURE 56   TEM images of Au elongated nanoparticles sandwiched between two 50 nm ALD TiO_2 layers and irradiated with 50 MeV ^{127}I at 2×10^{14} ions/cm^2. The same particles were imaged before (left) and after (right) the irradiation.

On the other hand, Ag nanoparticles do not elongate in TiO_2 for diameter less than 15 nm and the bigger ones elongate at the same ratio with Au nanoparticles.
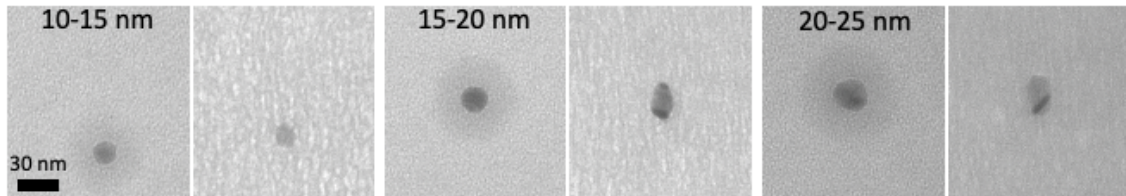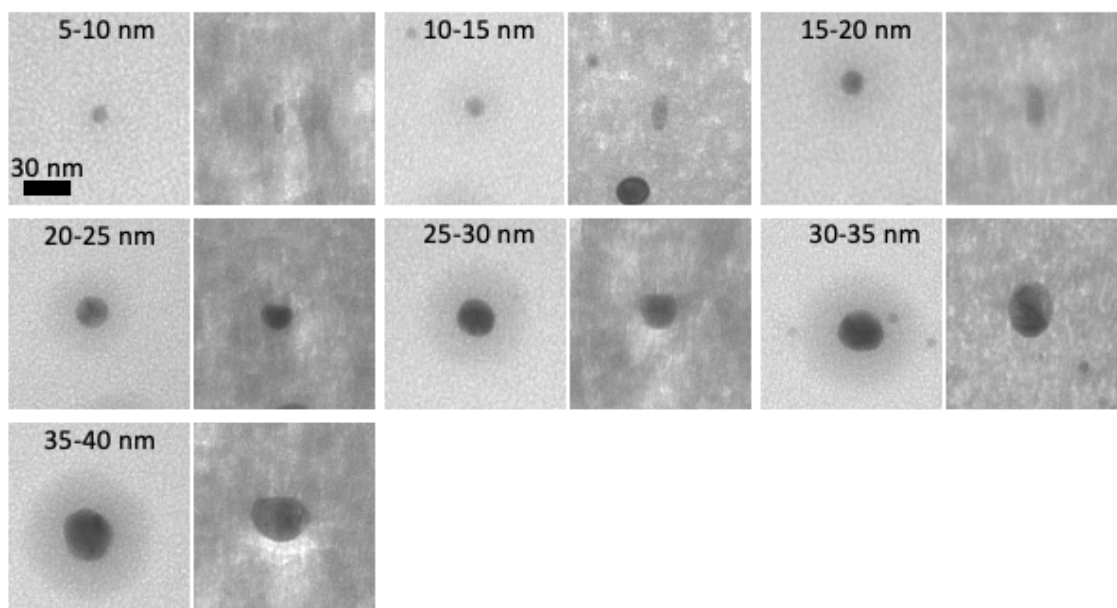

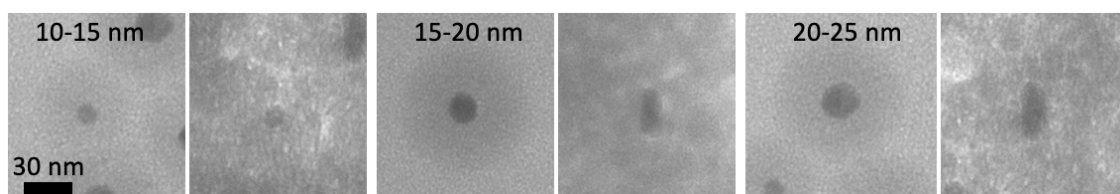FIGURE 57   TEM images of Ag elongated nanoparticles sandwiched between two 50 nm ALD TiO_2 layers and irradiated with 50 MeV ^{127}I at 2×10^{14} ions/cm^2. The same particles were imaged before (left) and after (right) the irradiation.

8 NANOPLASMONIC ACTIVITY OF SHI IRRADIATED NANOPARTICLES

8.1 Elongated nanoparticles embedded in SiO$_2$ and Al$_2$O$_3$

Dark field optical microscopic spectroscopy is a well established technique to locate and measure the scattering spectra of individual nanostructures. However, some difficulties appear which limit the size range of the measured nanostructures. Firstly, the image of an illuminated nanostructure is a colored circle with size bigger than the actual (a few hundreds of nm) because of the resolution of the microscope. This fact initiates problems when two nanostructures are relatively close to each other and their signals overlap. The internanostructure distance affects also the area that a fiber covers as it has diameter close to 2 μm. If the nanostructure is located at the center of the fiber, it should have more than 1 μm distance from the neighboring nanostructure. Moreover, only elongated nanoparticles with width more than 30 nm can be imaged [97–99], because the absorption is dominating for sizes less than 30 nm resulting in weak scattering, which is easily lost in the background [99] in conjugation to the fact that the nanoparticles are embedded inside a material and are not lying on a surface. If our microscope setup would have had, for example, CCD camera of higher resolution or better coupling between the fiber and the spectrograph, the limit could have been slightly lower. In Figure 58, a dark field optical image and the corresponding TEM image are shown. It is obvious that nanoparticles over a specific size can be imaged by a dark field optical microscope, but smaller ones are not visible.

The experiments were accompanied by finite difference time domain (FDTD) simulations of the embedded and elongated nanoparticles in order to confirm the reliability of the experimental results.

The spectra with the corresponding nanostructures are shown in Figure 59. The spherical nanoparticles in Figure 59c exhibit one (dipolar) plasmon mode and the elongated nanoparticles in Figure 59a,b and d exhibit two plasmon modes, one longitudinal (main peak) and one transverse (smaller peak). In the case of Al$_2$O$_3$, the split between the two LSPR modes is 71 nm and 46 nm in the Figures
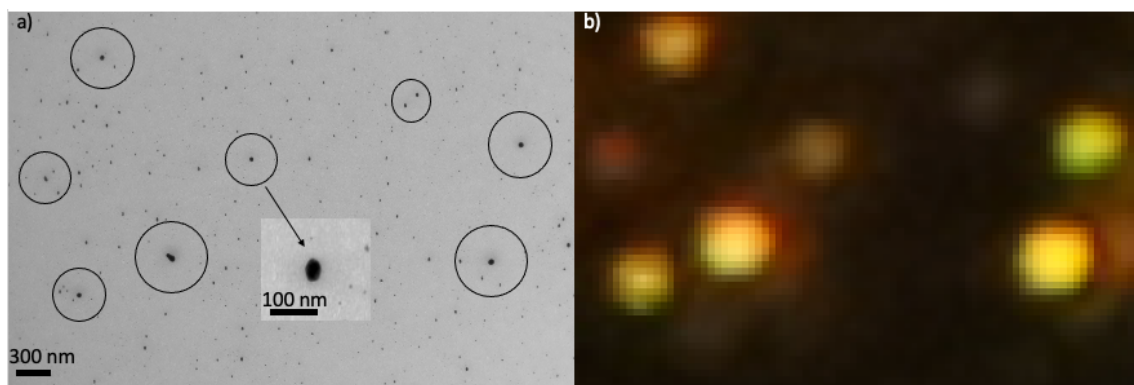
FIGURE 58 (a) TEM image of irradiated nanoparticles embedded in Al_2O_3 and (b) dark field optical image of the same area. The inset image in (a) corresponds to a magnified image of the nanoparticle indicated by the arrow, while the nanoparticles inside the circle in TEM image correspond to the coloured spots in dark field image.

59a and 59b, respectively due to the different width of the nanoparticles. In the case of SiO_2, the split is 48 nm in Figure 59d. However, the transverse mode of the elongated nanoparticle in Figure 59d is very weak due to the width of the nanoparticle which reaches the limit of the size detection [100]. In addition, the measured main LSPR peak of Al_2O_3 is more red shifted than that of SiO_2 because of higher refractive index.

80
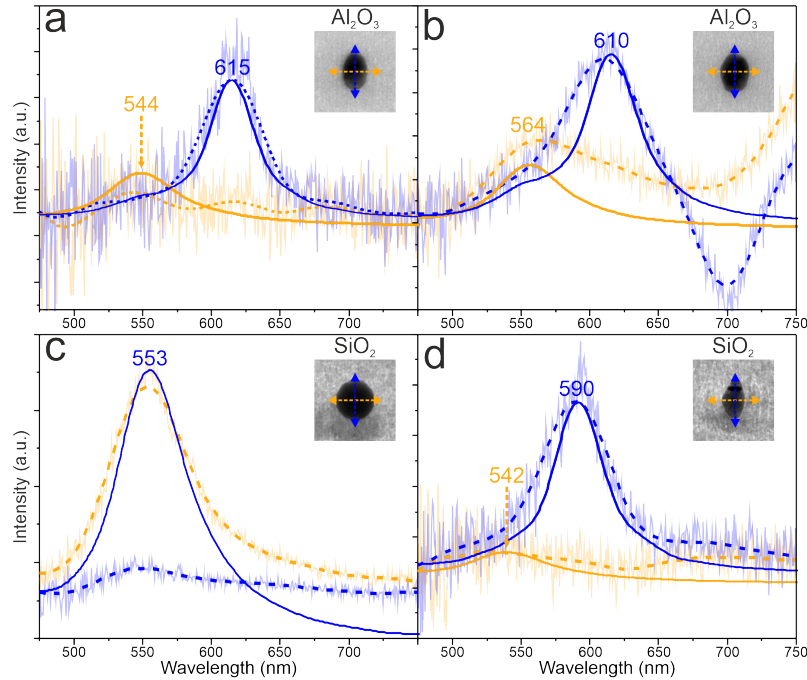
FIGURE 59 Dark field scattering spectra of two elongated nanoparticles embedded in Al$_2$O$_3$ (a,b), one spherical nanoparticle embedded in SiO$_2$ (c) and one elongated nanoparticle embedded in SiO$_2$ (d). The solid line is the result from the FDTD simulation and the dashed line the averaged measurement, with original data shown as a lighter line. The blue and the yellow spectra correspond to the longitudinal and transverse modes, respectively. The inset TEM images show the measured particles with LSP polarisations marked. The size of the TEM images is 110 nm×110 nm. The lengths and the widths of the particles in (a) and (b) are 51.3 nm and 32.5 nm and 51.9 nm and 39.9 nm, respectively. The diameter of the particle in (c) is 53.6 nm and the length and the width of the particle in (d) are 52.5 nm and 31.9 nm, respectively. Reproduced from [PIII] under the license CC BY 3.0.

The nanoplasmonic activity of individual nanoparticles embedded in SiO$_2$ and irradiated with SHI has been previously investigated by means of electron energy loss spectroscopy in scanning transmission electron microscope (STEM EELS) [10, 60]. In the case of a spherical Au nanoparticle, there is a small shift of the LSPR peak to lower wavelength (553 nm) for a nanoparticle with 22 nm diameter in Kobylko's results because in our study, the spherical nanoparticle is bigger (53.6 nm) and measured after the irradiation. In the case of an elongated nanoparticle, Kobylko et al [60] measured a nanoparticle of 61.6 nm length and 31.4 nm width (aspect ratio 1.94), which had longitudinal LSPR peak at 652 nm and transverse peak at 532 nm. In our measurements, the elongated nanoparticle had 52.5 nm length and 31.4 nm width (aspect ratio 1.64). The transverse peak was located at 542 nm which slightly differs from Kobylko's result because the width in both cases is almost the same and there is a difference in irradiation conditions. On the other hand, the longitudinal peak was located at 590 nm which significantly differs from Kobylko's result because there is 9.1 nm difference in length.

As mentioned above, there is a limitation in the size of the nanoparticles that can be measured by means of dark field spectroscopy. There are other techniques which can be used to investigate the LSPRs of nanoparticles with even smaller dimensions including STEM EELS [60, 101, 102], scanning near-field optical microscopy (SNOM) [103, 104] and confocal microscopy [105]. Even in the case of EELS [60], the transverse LSP mode of the nanorods with big aspect ratio (5-14) and width between 7 and 12 nm cannot be detected while they are embedded in SiO_2. However, both longitudinal and transverse modes of free standing nanorods on SiO_2 with 10 nm width (aspect ratio 4) can be detected by means of EELS [101]. In conclusion, dark field optical microscopy and spectroscopy can be easily utilized to detect single elongated nanoparticles without the need of preimaging with TEM.

9   SUMMARY AND OUTLOOK

A systematic study of nanoparticles shape modification under swift heavy ion irradiation was conducted. This investigation was facilitated by identifying the same nanoparticle buried inside an insulating matrix before and after the irradiation as thin Si_3N_4 TEM grid was used as a substrate.

Since the elongation of the spherical nanoparticles is expected to be sensitive to the matrix material properties, we performed analytical comparison of nanoparticles elongation in SiO_2 matrix deposited through different methods. The results showed that the nanoparticle elongation depends strongly on the deposition process of SiO_2 and SiO_2 quality in addition to the initial size of the nanoparticles. Therefore, several processing parameters should be carefully tuned in order to produce the desired result. Earlier, we could not observe significant differences concerning the elongation of gold nanoparticles in SiO_2 between different studies.

Once the basic process was proven to be working, the elongation of spherical nanoparticles embedded in SiO_2 was followed by the irradiation of spherical nanoparticles embedded in other materials, such as Al_2O_3 and TiO_2. Depending on the different matrix and the elemental compositions of the nanoparticles, the nanoparticles elongate differently. As a result, gold nanoparticles embedded in ALD Al_2O_3 elongated similarly as in ALD SiO_2, but smaller elongation was achieved for silver nanoparticles embedded in Al_2O_3. On the other hand, ALD TiO_2 offers significantly smaller elongation for both gold and silver nanoparticles compared to other materials, so it is not worth to be considered any further. Basically, we proved that an amorphous material, such as Al_2O_3, with lower electron-phonon coupling and greater thermal conductivity than SiO_2 can lead to the production of nanorods with ratio comparable to that of SiO_2. This observation should lead to the reconsideration how much these two values affect the elongation.

The shortage of research on nanoparticles having shape other than spherical motivated the investigation of gold nanorods embedded in SiO_2. Depending on the nanorod initial size and irradiation fluence, the nanorods can be re-oriented to align along the ion beam direction or some nanorods do not manage to get fully

re-oriented. In this case, they rather turn to spheroid or random spikes can be induced on them. In addition, the biggest nanorods cannot change at all. MD simulations showed that the nanorod re-orientation is a result of small incremental shape changes from nanorod to spheroid and back to a nanorod aligned with the ion beam direction. Finally, the scattering spectra from the elongated nanoparticles by means of dark field spectroscopy confirmed the existence of two discrete plasmon modes, one longitudinal and one transverse. As a result, the fabricated samples were proved to be possible candidates for photonic applications.

In the future, there are plenty of possibilities for further investigations. First of all, MD simulations should be applied for nanoparticles embedded in Al_2O_3 and Si_3N_4 as well to obtain information about the elongation mechanism. Furthermore, nanorods should be investigated more in order to precisely produce complex morphologies on them when they are embedded either in SiO_2 or in other matrices (Al_2O_3 and Si_3N_4). Finally, wafer scale samples should be fabricated to test the photonic applications in true industrial scale.

BIBLIOGRAPHY

1. d'Orleans, C. *et al.* Anisotropy of Co nanoparticles induced by swift heavy ions. *Physical Review B* **67,** 220101 (2003).

2. Roorda, S. *et al.* Aligned gold nanorods in silica made by ion irradiation of core–shell colloidal particles. *Advanced Materials* **16,** 235–237 (2004).

3. Mishra, Y. *et al.* Synthesis of elongated Au nanoparticles in silica matrix by ion irradiation. *Applied Physics Letters* **91,** 063103 (2007).

4. Giulian, R. *et al.* Shape transformation of Pt nanoparticles induced by swift heavy-ion irradiation. *Physical Review B* **78,** 125413 (2008).

5. Awazu, K. *et al.* Synthesis of elongated Au nanoparticles in silica matrix by ion irradiation. *Physical Review B* **78,** 054102 (2008).

6. Dawi, E., Vredenberg, A., Rizza, G & Toulemonde, M. Ion-induced elongation of gold nanoparticles in silica by irradiation with Ag and Cu swift heavy ions: track radius and energy loss threshold. *Nanotechnology* **22,** 215607 (2011).

7. Rizza, G *et al.* Rational description of the ion-beam shaping mechanism. *Physical Review B* **86,** 035450 (2012).

8. Amekura, H *et al.* Shape elongation of Zn nanoparticles in silica irradiated with swift heavy ions of different species and energies: scaling law and some insights on the elongation mechanism. *Nanotechnology* **25,** 435301 (2014).

9. Coulon, P.-E. *et al.* Ion-shaping of embedded gold hollow nanoshells into vertically aligned prolate morphologies. *Scientific Reports* **6,** 1–12 (2016).

10. Slablab, A. *et al.* Fabrication of ion-shaped anisotropic nanoparticles and their orientational imaging by second-harmonic generation microscopy. *Scientific Reports* **6,** 37469 (2016).

11. Mota-Santiago, P *et al.* Ion shaping of single-layer Au nanoparticles in amorphous silicon dioxide, in silicon nitride, and at their interface. *Physical Review Materials* **4,** 096002 (2020).

12. Li, R. *et al.* Matrix-material dependence on the elongation of embedded gold nanoparticles induced by 4 MeV C60 and 200 MeV Xe ion irradiation. *Nanotechnology* **31,** 265606 (2020).

13. Kluth, P. *et al.* Fine structure in swift heavy ion tracks in amorphous SiO_2. *Physical Review Letters* **101,** 175503 (2008).

14. Leino, A. A. *et al.* Swift heavy ion shape transformation of Au nanocrystals mediated by molten material flow and recrystallization. *Materials Research Letters* **2,** 37–42 (2014).

15. Vu, T. *et al.* Elongation mechanism of the ion shaping of embedded gold nanoparticles under swift heavy ion irradiation. *Nuclear Instruments and Methods in Physics Research Section B: Beam Interactions with Materials and Atoms* **451,** 42–48 (2019).

16. Amekura, H *et al.* On the mechanism of the shape elongation of embedded nanoparticles. *Nuclear Instruments and Methods in Physics Research Section B: Beam Interactions with Materials and Atoms* **475,** 44–48 (2020).

17. Toulemonde, M, Dufour, C. & Paumier, E. The ion-matter interaction with swift heavy ions in the light of inelastic thermal spike model. *ACTA PHYSICA POLONICA SERIES A* **109,** 311 (2006).

18. Suntola, T. Atomic layer epitaxy. *Materials Science Reports* **4,** 261–312 (1989).

19. George, S. M. Atomic layer deposition: an overview. *Chemical Reviews* **110,** 111–131 (2010).

20. Bharadwaj, P., Deutsch, B. & Novotny, L. Optical Antennas. *Advances in Optics and Photonics* **1,** 438–483 (2009).

21. Lee, K.-S. & El-Sayed, M. A. Gold and silver nanoparticles in sensing and imaging: sensitivity of plasmon response to size, shape, and metal composition. *The Journal of Physical Chemistry B* **110,** 19220–19225 (2006).

22. Knoll, G. F. *Radiation detection and measurement* (John Wiley & Sons, 2010).

23. Leino, A. *Atomistic Simulations of Swift Heavy Ion Irradiation Effects in Silica* PhD thesis (University of Helsinki, 2020).

24. Krasheninnikov, A. & Nordlund, K. Ion and electron irradiation-induced effects in nanostructured materials. *Journal of Applied Physics* **107,** 3 (2010).

25. Kitayama, T *et al.* Formation of ion tracks in amorphous silicon nitride films with Mev C60 ions. *Nuclear Instruments and Methods in Physics Research Section B: Beam Interactions with Materials and Atoms* **356,** 22–27 (2015).

26. O'Connell, J., Rymzhanov, R., Skuratov, V., Volkov, A. & Kirilkin, N. Latent tracks and associated strain in Al_2O_3 irradiated with swift heavy ions. *Nuclear Instruments and Methods in Physics Research Section B: Beam Interactions with Materials and Atoms* **374,** 97–101 (2016).

27. Toulemonde, M *et al.* Track creation in SiO_2 and $BaFe_{12}O_{19}$ by swift heavy ions: a thermal spike description. *Nuclear Instruments and Methods in Physics Research Section B: Beam Interactions with Materials and Atoms* **116,** 37–42 (1996).

28. Zhang, J. *et al.* Nanoscale phase transitions under extreme conditions within an ion track. *Journal of Materials Research* **25,** 1344–1351 (2010).

29. Waligorski, M., Hamm, R. & Katz, R. The radial distribution of dose around the path of a heavy ion in liquid water. *International Journal of Radiation Applications and Instrumentation. Part D. Nuclear Tracks and Radiation Measurements* **11,** 309–319 (1986).

30. Watanabe, T, Yamasaki, D, Tatsumura, K & Ohdomari, I. Improved interatomic potential for stressed Si, O mixed systems. *Applied Surface Science* **234,** 207–213 (2004).

31. Samela, J., Nordlund, K., Popok, V. N. & Campbell, E. E. Origin of complex impact craters on native oxide coated silicon surfaces. *Physical Review B* **77,** 075309 (2008).

32. Foiles, S., Baskes, M. & Daw, M. S. Embedded-atom-method functions for the fcc metals Cu, Ag, Au, Ni, Pd, Pt, and their alloys. *Physical Review B* **33,** 7983 (1986).

33. Foiles, S., Baskes, M. & Daw, M. Erratum: Embedded-atom-method functions for the fcc metals Cu, Ag, Au, Ni, Pd, Pt, and their alloys. *Physical Review B* **37,** 10378 (1988).

34. Ziegler, J., Biersack, J. & Littmark, U. SRIM-The Stopping and Range of Ions in Solids. *Pergamon* (1985).

35. Bringa, E. & Johnson, R. Coulomb explosion and thermal spikes. *Physical Review Letters* **88,** 165501 (2002).

36. Devanathan, R. & Weber, W. J. Simulation of collision cascades and thermal spikes in ceramics. *Nuclear Instruments and Methods in Physics Research Section B: Beam Interactions with Materials and Atoms* **268,** 2857–2862 (2010).

37. Berendsen, H. J., Postma, J. v., van Gunsteren, W. F., DiNola, A. & Haak, J. R. Molecular dynamics with coupling to an external bath. *The Journal of Chemical Physics* **81,** 3684–3690 (1984).

38. Djurabekova, F. & Nordlund, K. Atomistic simulation of the interface structure of Si nanocrystals embedded in amorphous silica. *Physical Review B* **77,** 115325 (2008).

39. Leino, A. A., Pakarinen, O. H., Djurabekova, F. & Nordlund, K. A study on the elongation of embedded Au nanoclusters in SiO_2 by swift heavy ion irradiation using MD simulations. *Nuclear Instruments and Methods in Physics Research Section B: Beam Interactions with Materials and Atoms* **282,** 76–80 (2012).

40. Jantunen, V. *et al.* Interface effects on heat dynamics in embedded metal nanoparticles during swift heavy ion irradiation. *Journal of Physics D: Applied Physics* **55,** 275301 (2022).

41. Kluth, P. *et al.* Nanoscale density fluctuations in swift heavy ion irradiated amorphous SiO_2. *Journal of Applied Physics* **110,** 123520 (2011).

42. Mota-Santiago, P. *et al.* Nanoscale density variations induced by high energy heavy ions in amorphous silicon nitride and silicon dioxide. *Nanotechnology* **29,** 144004 (2018).

43. Rymzhanov, R., Medvedev, N & Volkov, A. Damage threshold and structure of swift heavy ion tracks in Al_2O_3. *Journal of Physics D: Applied Physics* **50,** 475301 (2017).

44. Zhai, P. *et al.* Fine structure of swift heavy ion track in rutile TiO_2. *Nuclear Instruments and Methods in Physics Research Section B: Beam Interactions with Materials and Atoms* **457,** 72–79 (2019).

45. O'Connell, J., Skuratov, V., Akilbekov, A, Zhumazhanova, A & van Vuuren, A. J. EM study of latent track morphology in TiO_2 single crystals. *Nuclear Instruments and Methods in Physics Research Section B: Beam Interactions with Materials and Atoms* **379,** 200–205 (2016).

46. Pakarinen, O. H., Djurabekova, F. & Nordlund, K. Density evolution in formation of swift heavy ion tracks in insulators. *Nuclear Instruments and Methods in Physics Research Section B: Beam Interactions with Materials and Atoms* **268,** 3163–3166 (2010).

47. Sahoo, D., Ali, N., Singh, B. & Ghosh, S. *Swift heavy ion irradiation in ZnO films* in *AIP Conference Proceedings* **2142** (2019), 040020.

48. Amekura, H. *et al.* Zn nanoparticles irradiated with swift heavy ions at low fluences: Optically-detected shape elongation induced by nonoverlapping ion tracks. *Physical Review B* **83,** 205401 (2011).

49. Dawi, E., ArnoldBik, W., Ackermann, R & Habraken, F. Shaping of Au nanoparticles embedded in various layered structures by swift heavy ion beam irradiation. *Nuclear Instruments and Methods in Physics Research Section B: Beam Interactions with Materials and Atoms* **384,** 86–92 (2016).

50. Mota-Santiago, P., Kremer, F., Nadzri, A., Ridgway, M. C. & Kluth, P. Elongation of metallic nanoparticles at the interface of silicon dioxide and silicon nitride. *Nuclear Instruments and Methods in Physics Research Section B: Beam Interactions with Materials and Atoms* **409,** 328–332 (2017).

51. Sanchez-Dena, O. *et al.* Size-and shape-dependent nonlinear optical response of Au nanoparticles embedded in sapphire. *Optical Materials Express* **4,** 92–100 (2014).

52. Mota-Santiago, P.-E. *et al.* Size characterisation of noble-metal nano-crystals formed in sapphire by ion irradiation and subsequent thermal annealing. *Applied Surface Science* **259,** 574–581 (2012).

53. Wolf, S. *et al.* Shape manipulation of ion irradiated Ag nanoparticles embedded in lithium niobate. *Nanotechnology* **27,** 145202 (2016).

54. Kluth, P *et al.* Energy dependent saturation width of swift heavy ion shaped embedded Au nanoparticles. *Applied Physics Letters* **94,** 113107 (2009).

55. Ridgway, M. C. *et al.* Role of thermodynamics in the shape transformation of embedded metal nanoparticles induced by swift heavy-ion irradiation. *Physical review letters* **106,** 095505 (2011).

56. Mota-Santiago, P. E. *Swift Heavy-Ion Irradiation of Amorphous Silicon Dioxide, Silicon Nitride and Silicon Oxynitrides Composite Systems: From Ion Tracks to Nanoparticle Shaping* PhD thesis (Australian National University, 2020).

57. Saleh, B. E. & Teich, M. C. *Fundamentals of Photonics* (john Wiley & sons, 2019).

58. Mie, G. Beiträge zur Optik trüber Medien, speziell kolloidaler Metallösungen. *Annalen der physik* **330,** 377–445 (1908).

59. Wang, L., Hasanzadeh Kafshgari, M. & Meunier, M. Optical Properties and Applications of Plasmonic-Metal Nanoparticles. *Advanced Functional Materials* **30,** 2005400 (2020).

60. Kobylko, M. *et al.* Localized plasmonic resonances of prolate nanoparticles in a symmetric environment: experimental verification of the accuracy of numerical and analytical models. *Physical Review Applied* **9,** 064038 (2018).

61. Williams, D. B. & Carter, C. B. *Transmission Electron Microscopy* (Springer Nature, 2009).

62. Sterling, H. & Swann, R. Chemical vapour deposition promoted by rf discharge. *Solid-State Electronics* **8,** 653–654 (1965).

63. https://plasma.oxinst.com/technology/pecvd (Last retrieved at 05-01-2023).

64. Suntola, T. & Antson, J. *Method for producing compound thin films* US Patent 4,058,430. 1977.

65. Potts, S. & Kessels, W. Energy-enhanced atomic layer deposition for more process and precursor versatility. *Coordination Chemistry Reviews* **257,** 3254–3270 (2013).

66. Kim, H., Maeng, W.-J., *et al.* Applications of atomic layer deposition to nanofabrication and emerging nanodevices. *Thin Solid Films* **517,** 2563–2580 (2009).

67. Murphy, D. B. *Fundamentals of Light Microscopy and Electronic Imaging* (John Wiley & Sons, 2002).

68. https://en.wikipedia.org/wiki/Transmission_electron_microscopy (Last retrieved at 05-01-2023).

69. Hlawacek, G., Veligura, V., van Gastel, R. & Poelsema, B. Helium ion microscopy. *Journal of Vacuum Science & Technology B, Nanotechnology and Microelectronics: Materials, Processing, Measurement, and Phenomena* **32,** 020801 (2014).

70. Bell, D. C., Lemme, M. C., Stern, L. A., Williams, J. R. & Marcus, C. M. Precision cutting and patterning of graphene with helium ions. *Nanotechnology* **20,** 455301 (2009).

71. Tesmer, J. R. & Nastasi, M. Handbook of modern ion beam materials analysis. *Materials Research Society, 9800 McKnight Rd, Suite 327, Pittsburgh, PA 15237, USA, 1995. 700* (1995).

72. Laitinen, M., Rossi, M., Julin, J. & Sajavaara, T. Time-of-flight - Energy spectrometer for elemental depth profiling - Jyväskylä design. *Nuclear Instruments and Methods in Physics Research Section B: Beam Interactions with Materials and Atoms* **337,** 55–61 (2014).

73. Arstila, K. *et al.* Potku–New analysis software for heavy ion elastic recoil detection analysis. *Nuclear Instruments and Methods in Physics Research Section B: Beam Interactions with Materials and Atoms* **331,** 34–41 (2014).

74. Daillant, J. & Gibaud, A. *X-ray and neutron reflectivity: principles and applications* (Springer, 2008).

75. Tompkins, H. & Irene, E. A. *Handbook of ellipsometry* (William Andrew, 2005).

76. Airaksinen, V.-M. in *Handbook of Silicon Based MEMS Materials and Technologies* 381–390 (Elsevier, 2015).

77. Jenkins, T. Multiple-angle-of-incidence ellipsometry. *Journal of Physics D: Applied Physics* **32,** R45 (1999).

78. Zarchi, M., Ahangarani, S. & Sanjari, M. Z. Properties of silicon dioxide film deposited by PECVD at low temperature/pressure. *Metallurgical and Materials Engineering* **20,** 89–96 (2014).

79. Van Dillen, T., van Blaaderen, A. & Polman, A. Shaping colloidal assemblies. *Materials Today* **7,** 40–46 (2004).

80. Nečas, D. & Klapetek, P. Gwyddion: an open-source software for SPM data analysis. *Open Physics* **10,** 181–188 (2012).

81. Schneider, C. A., Rasband, W. S. & Eliceiri, K. W. NIH Image to ImageJ: 25 years of image analysis. *Nature methods* **9,** 671–675 (2012).

82. Nordlund, K. *et al.* Defect production in collision cascades in elemental semiconductors and fcc metals. *Physical Review B* **57,** 7556 (1998).

83. Ghaly, M., Nordlund, K. & Averback, R. S. Molecular dynamics investigations of surface damage produced by kiloelectronvolt self-bombardment of solids. *Philosophical Magazine A* **79,** 795–820 (1999).

84. Amekura, H. *et al.* Vaporlike phase of amorphous SiO_2 is not a prerequisite for the core/shell ion tracks or ion shaping. *Physical Review Materials* **2,** 096001 (2018).

85. https://bio.libretexts.org/Bookshelves/Microbiology/Microbiology_(OpenStax)/02 (Last retrieved at 05-01-2023).

86. Shen, B. *et al.* Plasmonic nanostructures through DNA-assisted lithography. *Science Advances* **4,** eaap8978 (2018).

87. Tapio, K. *et al.* A DNAânanoparticle actuator enabling optical monitoring of nanoscale movements induced by an electric field. *Nanoscale* **10,** 19297–19309 (2018).

88. (2021) Lumerical Inc.

89. Johnson, P. & Christy, R. Optical Constants of the Noble Metals. *Physical Review B* **6,** 4370–4379 (1972).

90. Amirzada, M. R., Tatzel, A., Viereck, V. & Hillmer, H. Surface roughness analysis of SiO_2 for PECVD, PVD and IBD on different substrates. *Applied Nanoscience* **6,** 215–222 (2016).

91. Peña-Rodríguez, O. *et al.* Understanding the ion-induced elongation of silver nanoparticles embedded in silica. *Scientific Reports* **7,** 1–9 (2017).

92. Amekura, H *et al.* C60 ions of 1 MeV are slow but elongate nanoparticles like swift heavy ions of hundreds MeV. *Scientific Reports* **9,** 1–10 (2019).

93. Kinnunen, S., Arstila, K. & Sajavaara, T. Al2O3 ALD films grown using TMA+ rare isotope 2H216O and 1H218O precursors. *Applied Surface Science* **546,** 148909 (2021).

94. Rymzhanov, R., Medvedev, N. & Volkov, A. Effect of valence holes kinetics on material excitation in tracks of swift heavy ions. *Nuclear Instruments and Methods in Physics Research Section B: Beam Interactions with Materials and Atoms* **365,** 462–467 (2015).

95. https://www.makeitfrom.com/material-properties/Alumina-Aluminum-Oxide-Al2O3 (Last retrieved at 05-01-2023).

96. Gao, T. & Jelle, B. P. Thermal conductivity of TiO2 nanotubes. *The Journal of Physical Chemistry C* **117,** 1401–1408 (2013).

97. Anderson, L. J. *et al.* Quantitative measurements of individual gold nanoparticle scattering cross sections. *The Journal of Physical Chemistry C* **114,** 11127–11132 (2010).

98. Rostro-Kohanloo, B. C. *et al.* The stabilization and targeting of surfactant-synthesized gold nanorods. *Nanotechnology* **20,** 434005 (2009).

99. Zijlstra, P & Orrit, M. Single metal nanoparticles: optical detection, spectroscopy and applications. *Reports on Progress in Physics* **74,** 106401 (2011).

100. Huang, Y. & Kim, D.-H. Dark-field microscopy studies of polarization-dependent plasmonic resonance of single gold nanorods: rainbow nanoparticles. *Nanoscale* **3,** 3228–3232 (2011).

101. NÊŒEGom, M. *et al.* Single particle plasmon spectroscopy of silver nanowires and gold nanorods. *Nano Letters* **8,** 3200–3204 (2008).

102. Guiton, B. S. *et al.* Correlated optical measurements and plasmon mapping of silver nanorods. *Nano Letters* **11,** 3482–3488 (2011).

103. Imura, K., Nagahara, T. & Okamoto, H. Characteristic near-field spectra of single gold nanoparticles. *Chemical Physics Letters* **400,** 500–505 (2004).

104. Lim, J. K., Imura, K., Nagahara, T., Kim, S. K. & Okamoto, H. Imaging and dispersion relations of surface plasmon modes in silver nanorods by near-field spectroscopy. *Chemical Physics Letters* **412,** 41–45 (2005).

105. Jacobsen, V., Stoller, P., Brunner, C., Vogel, V. & Sandoghdar, V. Interferometric optical detection and tracking of very small gold nanoparticles at a water-glass interface. *Optics Express* **14,** 405–414 (2006).

ORIGINAL PAPERS

PI

NANOROD ORIENTATION CONTROL BY SWIFT HEAVY ION IRRADIATION

by

Spyridon Korkos, Ville Jantunen, Kai Arstila, Timo Sajavaara, Aleksi Leino, Kai Nordlund & Flyura Djurabekova

Nanorod orientation control by swift heavy ion irradiation

View Online   Export Citation   CrossMark

Spyridon Korkos,[1,2,a)] (iD) Ville Jantunen,[3] Kai Arstila,[1,2] (iD) Timo Sajavaara,[1,2] (iD) Aleksi Leino,[3] Kai Nordlund,[3] (iD) and Flyura Djurabekova[3] (iD)

AFFILIATIONS

[1]Accelerator Laboratory, Department of Physics, University of Jyvaskyla, P.O. Box 35, FI-40014 Jyvaskyla, Finland
[2]Nanoscience Center, Department of Physics, University of Jyvaskyla, P.O. Box 35, FI-40014 Jyvaskyla, Finland
[3]Department of Physics, University of Helsinki, P.O. Box 43, FI-00014 Helsinki, Finland

[a)]Author to whom correspondence should be addressed: spyridon.s.korkos@jyu.fi

ABSTRACT

Highly energetic ions have been previously used to modify the shape of metal nanoparticles embedded in an insulating matrix. In this work, we demonstrate that under suitable conditions, energetic ions can be used not only for shape modification but also for manipulation of nanorod orientation. This observation is made by imaging the same nanorod before and after swift heavy ion irradiation using a transmission electron microscope. Atomistic simulations reveal a complex mechanism of nanorod re-orientation by an incremental change in its shape from a rod to a spheroid and further back into a rod aligned with the beam.

Published under an exclusive license by AIP Publishing. https://doi.org/10.1063/5.0089028

Shape modification of metallic nanoparticles (NPs) has been studied for a long time as a tool for tuning the optical properties of nanocomposite materials. Spherical Au NPs have distinctive absorption peaks at visible light, which changes with size.[1] When the shape of the NPs is made cylindrical, there are two absorption peaks corresponding to transversal and longitudinal modes of surface plasmons.[1] This means that the ability to control the shapes of NPs allows for fine-tuning their response to light, making them ideal candidates for future nanoscale optical devices. Embedding the metal nanoparticles inside certain insulator materials, such as silica, allows keeping them protected from the environment and conserving whatever shape modifications have been achieved, including the orientation of the rods. While it may be difficult to access the NPs embedded inside the surrounding material with other methods, it is known that they can be modified using swift heavy ion (SHI) irradiation (i.e., using ions with energies $E \sim 1$ MeV/amu).[2–16]

Shape transformation of spherical metal NPs into nanorods aligned in the beam direction was initially reported by d'Orléans *et al.*[17] and confirmed in multiple studies later.[3,5–8,10–16] Several explanations, such as the overpressure model by d'Orléans *et al.*[17] and the ion hammering effect by Roorda *et al.*,[18] were suggested to explain the phenomenon. Although the ion hammering effect is expected to modify any size of NPs, SHI irradiation of NPs smaller than the track diameter did not cause the elongation effect.[12] On the other hand, the

overpressure model was supported by molecular dynamics simulations[3] that gave atomistic insight on expansion of molten nanoparticles into a softened and underdense track in silica.

Most studies on SHI irradiated NPs have focused on spherical NPs, while other shapes have received less attention. In this study, we focus on gold nanorods inside a silica matrix and how they react to SHI irradiation. We chose a 45° angle of incidence; however, this choice is arbitrary and does not affect the observed result. We use transmission electron microscope (TEM) window grids as substrates to keep track of individual nanorods before and after irradiation. To understand the shape modification mechanism, we use a multiscale molecular dynamics simulation model based on a two-temperature approach[3,5,19–22] to gain further insight into the details of this process. Our experiments and simulations consistently show that swift heavy ion irradiation can be used to orient nanorods into the beam direction even when they remain fully inside the insulating matrix. This allows the flexible manipulation of the nanorod orientation without a risk of chemical contamination.

A 50 nm thick SiO_2 film was grown using plasma-enhanced chemical vapor deposition (PECVD) at 200 °C (Plasmalab80Plus by Oxford Instruments, SiH_4 and N_2O as precursors) on top of a TEM grid with 20 nm thick Si_3N_4 windows. Chemically synthesized Au nanorods (Sigma-Aldrich, diameter 20–45 nm and length 30–90 nm) were dispersed on top of the film by dropcasting. The nanorods were

then embedded by means of an additional 50 nm PECVD-SiO$_2$ film. The total layer thickness of 120 nm fulfills the requirements of TEM imaging. Time-of-flight elastic recoil detection analysis (ToF-ERDA) with a 1.7 MV Pelletron accelerator and an 11.9 MeV ^{63}Cu^{6+} beam[23] was used to measure the elemental composition of the deposited films at the Accelerator Laboratory of University of Jyväskylä.

The samples were irradiated by the 50 MeV ^{127}I^{9+} ion beam at 45° incidence in the TAMIA 5 MV tandem accelerator at Helsinki Accelerator Laboratory (University of Helsinki). Irradiation was performed to the fluence of 10^{14} ions/cm^2 at room temperature. Imaging of the irradiated samples was performed with a JEOL-JEM 1400 TEM operated at 120 kV. The direction of an electron beam was chosen perpendicular to the ion beam direction used in the irradiation experiments. All the steps of this procedure are shown in Fig. 1.

To understand the re-orientation during irradiation, we used the classical molecular dynamics code PARCAS,[24] which was used earlier for elongation simulations of spherical nanoparticles.[3,16] We generated a rectangular box of the Au fcc lattice and cut out of it a nanorod of the required size. Since the size of the experimental nanorods is too large for efficient MD simulations, we reduced the size of the nanorods to 18 nm in length and 10 nm in width, while keeping the same aspect ratio as in the experimental one. The nanorods were embedded inside the amorphous SiO$_2$ matrix similar to Ref. 25. In brief, the nanorod is first compressed by 2%, a cavity in silica is created with the shape and size of the original NP, and the NP is then fit inside the cavity so that it will expand to the empty space when it relaxes. The nanorods were initially aligned perpendicular to the ion beam direction.

Since the shape modification occurs only after high ion irradiation fluence, we adopted a similar approach to simulate the SHI effects in MD as described in Ref. 3. We used the instant energy deposition profiles that were pre-calculated using the two-temperature i-TS model.[26] We used energy depositon profiles corresponding to both 50 MeV I and 164 MeV Au. We used the latter since it gave more efficient dynamics shape modification at higher irradiation energy, and hence, it was computationally more feasible to reach high fluences with the higher energy. Moreover, the melting point of the simulated silica is much higher compared to the experimentally observed values (3500 vs 1995 K in experiments). To compensate for this difference, we scaled the profile of the deposited energy in silica with the ratio of the melting points. The Au atoms were given a constant deposited energy of 0.5 eV/atom.[3] This energy was sufficient to melt the nanorod completely. The interatomic potentials were Watanabe–Samela[27,28] for interactions in silica, embedded atom model-like for Au–Au interactions,[29,30] and Ziegler–Biersack–Littmark (ZBL)[31] for Au–O and Au–Si interactions.

The system relaxation was done for 50 ps at pressure and temperature control[32] toward zero pressure and 300 K temperature. After the system was relaxed, radial energy deposition was added perpendicular to the major axis of the initial nanorod at random locations. The ion impact was then simulated for 100 ps in NVE. Berendsen temperature control[32] at 300 K was used within the thin boundary regions perpendicular to the ion direction to dampen oscillations from pressure waves and to emulate cooling provided by the bulk material in the experimental samples.

We note that the 100 ps simulation time, which we used for computational efficiency of MD simulations, was not enough to reach full recrystallization of the nanorods after the impact. However, recrystallization is a critical step in the shape modification process as reported by Leino et al.,[2] because the volume of the amorphized Au NP is too large to trigger the continuous material flow into opening ion tracks in subsequent simulations. The NP must shrink to nearly original volume (and density) during the cooldown stage for sufficient thermal expansion during the subsequent impact. Although we used a similar method as by Leino et al.[2] and Amekura et al.[16] to account for recrystallization, we verified this method by running an independent 1-ns long MD simulation of relaxation of a modified NP, which showed that the modified shape of the NP did not change even after much slow cooling (see the supplementary material).

In the analysis of the samples, the same nanoparticle was imaged before and after irradiation, as shown in Fig. 2, where the subfigures (a) and (b) show the same area of the sample before and after irradiation, respectively, with identical magnification. Moreover, the image shows that most nanorods are far from the others, which excludes possible interactions between them.

Since the ion beam induced shape modification of nanoparticles is sensitive to the matrix material properties,[33] at first we performed the elemental composition analysis of the grown films using ToF-ERDA measurements. The analysis confirmed the close-to-stoichiometric elemental ratio of the as-grown silicon dioxide (2.04 ± 0.02) and the extensive presence of hydrogen (>7 at. %), which is known to be released from the SiO$_2$ thin film during a SHI impact.[34] The depth profiles and detailed description of the ToF-ERDA analysis can be found in the supplementary material.

The analysis of a series of TEM images (totally 19) reveals that the nanorods within the diameter and length range from 20 to 31 nm and 32 to 63 nm, respectively, have changed their orientation to align
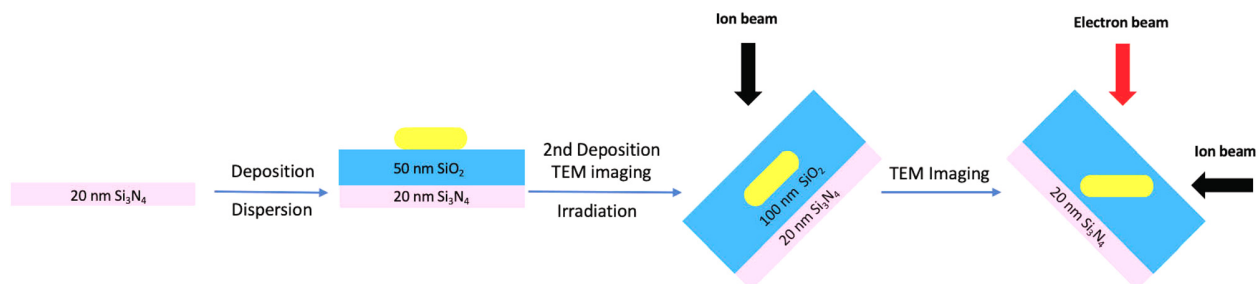

FIG. 1. Schematic representation of the experimental procedure. The sample during the second TEM stage (after irradiation) is placed in such a way that the TEM electron beam is directed perpendicular to the direction of the ion beam used during irradiation. By this way, the dimensions of the actual nanorod were imaged instead of its projection.
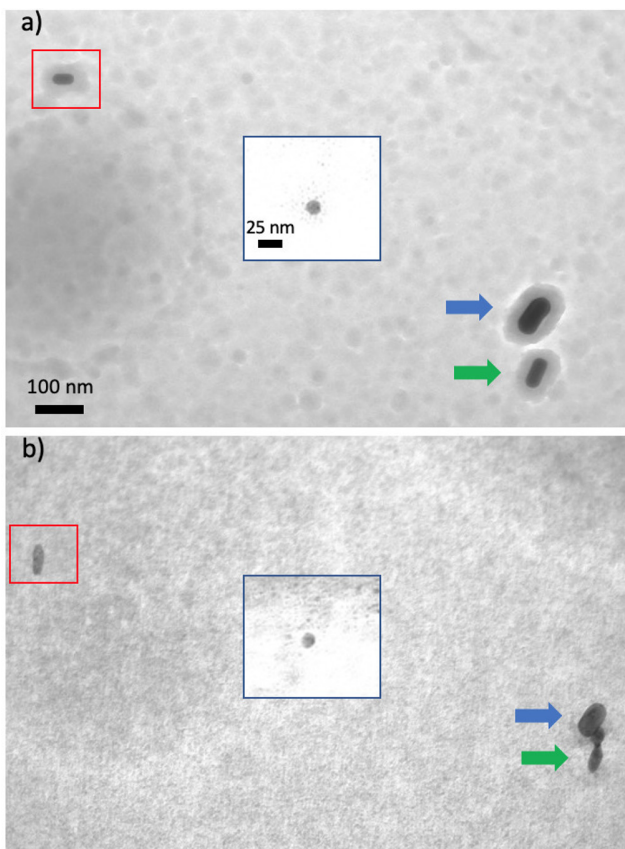
FIG. 2. TEM images of the 20 nm Si$_3$N$_4$/50 nm SiO$_2$/NRs/50 nm SiO$_2$ sample imaged (a) before and (b) after irradiation with ^{127}I at 10^{14} ions/cm^2. The images were taken (a) from the top and (b) perpendicular to the ion beam direction. (The red box outlines the nanorod, which re-orients along the ion beam direction.) The inset images in blue outline show a spherical nanoparticle (11.5 nm diameter) whose orientation did not change.

FIG. 3. TEM images of single nanorods sandwiched between two 50 nm PECVD SiO$_2$ layers with different initial size that re-orient along the ion beam direction after irradiation with ^{127}I at 10^{14} ions/cm^2. (a) Length $= 34.3$ nm and diameter $= 21.2$ nm, (b) length $= 38.5$ nm and diameter $= 20.3$ nm, and (c) length $= 53$ nm and diameter $= 32$ nm. (The left image is before, and the right is after irradiation.)

with the ion beam direction after the fluence of 10^{14} ions/cm^2 (see Fig. 3). This is a curious observation, since the nanorods were embedded in a homogeneous matrix, which remained intact throughout the experiment. Furthermore, the length along the major axes of the re-oriented nanorods has still visibly increased. We also note that the nanorods outside of the indicated size range have not been seen to change their orientation [compare a large nanorod indicated by a blue arrow in Figs. 2(a) and 2(b)], although the size has somewhat shrunk due to significant ion fluence. The behavior of a second large nanorod (green arrow), which is still beyond the above-mentioned range, is less clear. It is apparent that this nanorod was initially shrinking and only after its size reached the range of sizes that are seen to align with the beam, its re-orientation began. As shown in Fig. 2(b), the angle between the nanorods indicated by the blue and green arrows increased. The re-orientation, however, has not been completed, as the ion fluence received by this nanorod after its size was reduced was lower. We do not observe substantial changes in the nanorods and spherical nanoparticles that are below 15 nm in width, see the inset of Fig. 2. It is apparent that irradiation at such high ion fluences causes
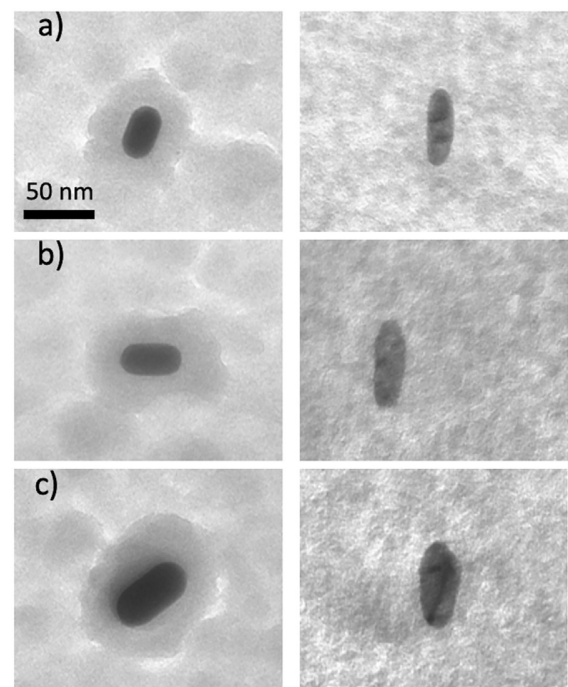
disintegration of the small nanoparticles and subsequent re-assembling within the track. These results are consistent with the previous work on nanospheres, which also were not found to change shape below a certain critical size.[3,13]

Furthermore, the TEM images of Fig. 3 reveal the polycrystallinity of the nanorods after irradiation. Rizza et al.[35] suggested that the presence of grains implies that the phase transition during the impact does not happen in the entire volume of the NP at once, but during each impact only a part of the NP melts. We, however, note here that polycrystallinity may result from fast quenching after the impact of the entirely molten NP, as shown in Ref. 3.

To understand the modification mechanism of the irradiated nanorods, we performed a series of simulations using the deposited energy profiles corresponding to 50 MeV ^{197}I and 164 MeV ^{197}Au ions. In these simulations, we saw that the first ion impacts induced formation of surface protrusions grown from the nanorods at the impact locations (see, e.g., the top left image in Fig. 4). Both deposited energy profiles gave similar results. Consecutive impacts add more localized protrusions, which gradually accumulate and cause shape transformation of the entire nanorod into at first, a spheroidal and then an elongated shape of a nanorod.

Since the dynamics of these modifications is faster under the impact of higher energy, we show in the left panel of Fig. 4 the evolution of shape modification of the nanorod irradiated by 164 MeV ^{197}Au. In comparison, similar images of the experimental nanorod are
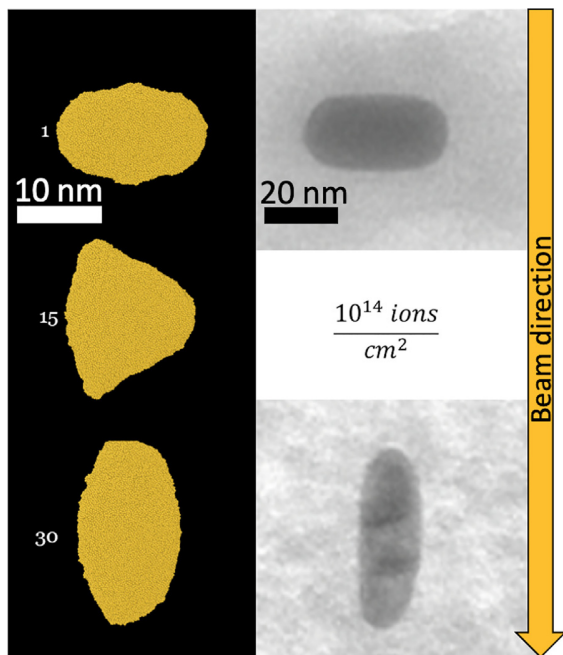
FIG. 4. Left: Nanoparticle shape after simulating 1, 15, and 30 impacts to random positions on the nanorod with 164 MeV ^{197}Au ion. Right: zoomed in of the same nanorod as in Fig. 3(b).

FIG. 5. Nanorod shape after 0, 25, 50, 75, and 100 simulated 50 MeV ^{127}I ion impacts to the center of the nanorod.

shown in the right panel. We follow the shape evolution by adding the ion tracks subsequently at random locations of the nanorod perpendicular to its major axis. Already after the first 15 impacts, the shape had incrementally changed to an asymmetrical spheroid, see the middle image in the left panel of Fig. 4, where the spheroid with a more elongated left side is shown. After the next 15 impacts, the shape is fully transformed into a rod in the beam direction, see the lowest image in the left panel of Fig. 4 and the corresponding experimental image on the lowest right. Although dimensions are different, the changes are proportional with similar elongation observed after irradiation in both simulation and experiment.

The simulations of ion impacts of 50 MeV ^{127}I on the same size of the nanorod are shown in Fig. 5. We see that under this energy, the shape of the nanorod changes much slower due to lower energy deposition. The results, however, are similar to those obtained for the 164 MeV ^{197}Au ions, i.e., small incremental changes transformed the nanorod oriented perpendicular to the beam into the nanorod oriented in the beam direction. Thus, we conclude that although the nanorod changes visibly its orientation, the change does not require the actual rotation within the solid matrix. The modification is guided by the dynamics of density changes in the matrix and material flow due to relaxing of the overpressured liquid phase of nanorods during the impact and fast quenching after it, as previously described for initially spherical systems.[3] The small incremental changes accumulate and result in growth in the beam direction and loss of length in others. This finally leads to a nanorod aligning in the beam direction.

We note that the irradiation conditions between the simulated and experimental nanorods are not identical. For instance, the
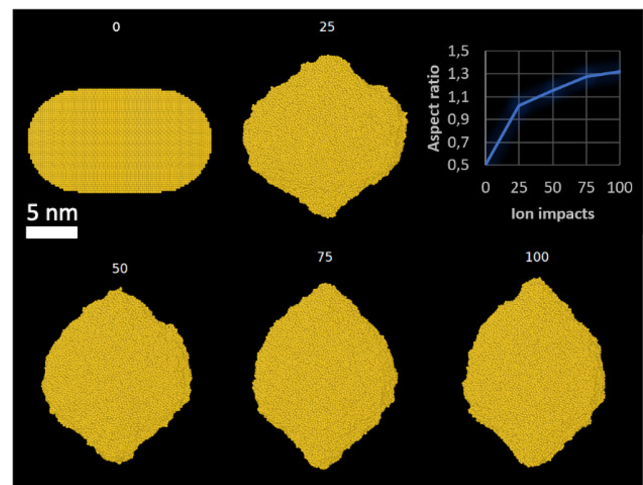
simulated nanorods are much smaller in size compared to those used in experiment. The numbers of ions needed to complete the re-orientation of the nanorod in simulations were 30 and 100 with the energies of 164 and 50 MeV, respectively. This corresponds to 2×10^{13} and 6.3×10^{13} ions/cm^2, i.e., the lower energy required a higher fluence to complete the re-orientation of the nanorod. The latter value of the fluence is close to the experimental fluence of 10^{14} ions/cm^2, where the ions with an energy of 50 MeV were used as well. This confirms that our MD simulations are consistent with experimental results. Moreover, a previous more detailed analysis of temperature evolution in embedded Au nanorods of different sizes due to swift heavy ion impacts further supports the presented results.[36] That work showed that the highest temperature in a nanoparticle always develops in the vicinity of ion impact, where the electron–phonon coupling is the strongest. In the nanorods of the size relevant to this study, this temperature is sufficient to cause substantial melting.

We still consider why the largest nanorods, such as the one marked with a blue arrow in Fig. 2, are not rotated. Previously, Rizza et al.[37] studied the size dependence of spherical nanoparticles on melting and concluded that large particles do not melt and are not deformed noticeably. In the recent study, we extended this model to nanorods including different possible interface effects on heat dynamics during the impact on a nanorod.[36] In these simulations, we saw that the energy deposited by a SHI in the large nanorods $(40 \times 80$ nm$^2)$ is not sufficient for melting even if all resistive effects for heat flow through the interface are taken into account.[36] Hence, no shape modification, including re-orientation, can be expected for very large nanorods.

In conclusion, using both experiments and simulations, we show how swift heavy ions with energies readily available in typical tandem accelerators can be used to re-orient nanorods, which are embedded in a solid amorphous matrix. In the experiments, we used TEM windows to track changes in individual nanorods. We observed that nanorods laid in a plane with a 45° angle to the beam direction re-oriented to align with the beam. By using a multiscale simulation model of the

effect of electronic excitations on atom dynamics, we explain the change in the nanorod orientation by an overpressure mechanism and show that the apparent re-orientation is a result of small incremental shape modifications rather than an actual rotation of the nanorod as a whole. Our results show that swift heavy ions even of relatively low energies can be used as a means to control the orientation of metal nanorods buried inside a protective insulating material.

See the supplementary material for the material analysis of as grown samples and the nanoparticle recrystallization in MD.

AUTHOR DECLARATIONS
Conflict of Interest

The authors have no conflicts to disclose.

Author Contributions

S.K. conducted the experiments and V.J. conceived the simulations. All authors discussed the results. S.K and V.J. wrote the manuscript, which was discussed and edited by all authors. S.K. and V.J. contributed equally to this work.

DATA AVAILABILITY

The data that support the findings of this study are available from the corresponding author upon reasonable request.

REFERENCES

[1]S. Link and M. A. El-Sayed, "Spectral properties and relaxation dynamics of surface plasmon electronic oscillations in gold and silver nanodots and nanorods," J. Phys. Chem. B **103**, 8410–8426 (1999).

[2]A. A. Leino, O. H. Pakarinen, F. Djurabekova, and K. Nordlund, "A study on the elongation of embedded au nanoclusters in SiO_2 by swift heavy ion irradiation using md simulations," Nucl. Instrum. Methods Phys. Res., Sect. B **282**, 76–80 (2012).

[3]A. A. Leino, O. Pakarinen, F. Djurabekova, K. Nordlund, P. Kluth, and M. C. Ridgway, "Swift heavy ion shape transformation of au nanocrystals mediated by molten material flow and recrystallization," Mater. Res. Lett. **2**, 37–42 (2014).

[4]E. Dawi, A. Vredenberg, G. Rizza, and M. Toulemonde, "Ion-induced elongation of gold nanoparticles in silica by irradiation with Ag and Cu swift heavy ions: Track radius and energy loss threshold," Nanotechnology **22**, 215607 (2011).

[5]O. Peña-Rodríguez, A. Prada, J. Olivares, A. Oliver, L. Rodríguez-Fernández, H. G. Silva-Pereyra, E. Bringa, J. M. Perlado, and A. Rivera, "Understanding the ion-induced elongation of silver nanoparticles embedded in silica," Sci. Rep. **7**, 922 (2017).

[6]C. d'Orleans, J. Stoquert, C. Estournes, J. Grob, D. Muller, J. Guille, M. Richard-Plouet, C. Cerruti, and F. Haas, "Elongated co nanoparticles induced by swift heavy ion irradiations," Nucl. Instrum. Methods Phys. Res., Sect. B **216**, 372–378 (2004).

[7]S. Klaumünzer, "Modification of nanostructures by high-energy ion beams," Nucl. Instrum. Methods Phys. Res., Sect. B **244**, 1–7 (2006).

[8]K. Awazu, X. Wang, M. Fujimaki, J. Tominaga, H. Aiba, Y. Ohki, and T. Komatsubara, "Elongation of gold nanoparticles in silica glass by irradiation with swift heavy ions," Phys. Rev. B **78**, 054102 (2008).

[9]K. Awazu, X. Wang, T. Komatsubara, J. Watanabe, Y. Matsumoto, S. Warisawa, and S. Ishihara, "The fabrication of aligned pairs of gold nanorods in SiO_2 films by ion irradiation," Nanotechnology **20**, 325303 (2009).

[10]E. Dawi, G. Rizza, M. Mink, A. Vredenberg, and F. Habraken, "Ion beam shaping of au nanoparticles in silica: Particle size and concentration dependence," J. Appl. Phys. **105**, 074305 (2009).

[11]P. Kluth, R. Giulian, D. Sprouster, C. Schnohr, A. Byrne, D. Cookson, and M. Ridgway, "Energy dependent saturation width of swift heavy ion shaped embedded au nanoparticles," Appl. Phys. Lett. **94**, 113107 (2009).

[12]D. Avasthi, Y. Mishra, F. Singh, and J. Stoquert, "Ion tracks in silica for engineering the embedded nanoparticles," Nucl. Instrum. Methods Phys. Res., Sect. B **268**, 3027–3034 (2010).

[13]M. C. Ridgway, R. Giulian, D. J. Sprouster, P. Kluth, L. L. Araújo, D. Llewellyn, A. Byrne, F. Kremer, P. F. P. Fichtner, G. Rizza et al., "Role of thermodynamics in the shape transformation of embedded metal nanoparticles induced by swift heavy-ion irradiation," Phys. Rev. Lett. **106**, 095505 (2011).

[14]H. Amekura, N. Ishikawa, N. Okubo, M. C. Ridgway, R. Giulian, K. Mitsuishi, Y. Nakayama, C. Buchal, S. Mantl, and N. Kishimoto, "Zn nanoparticles irradiated with swift heavy ions at low fluences: Optically-detected shape elongation induced by nonoverlapping ion tracks," Phys. Rev. B **83**, 205401 (2011).

[15]Y. Mishra, F. Singh, D. Avasthi, J. Pivin, D. Malinovska, and E. Pippel, "Synthesis of elongated au nanoparticles in silica matrix by ion irradiation," Appl. Phys. Lett. **91**, 063103 (2007).

[16]H. Amekura, P. Kluth, P. Mota-Santiago, I. Sahlberg, V. Jantunen, A. A. Leino, H. Vázquez, K. Nordlund, F. Djurabekova, N. Okubo et al., "Vaporlike phase of amorphous SiO_2 is not a prerequisite for the core/shell ion tracks or ion shaping," Phys. Rev. Mater. **2**, 096001 (2018).

[17]C. d'Orléans, J. Stoquert, C. Estournes, C. Cerruti, J. Grob, J. Guille, F. Haas, D. Muller, and M. Richard-Plouet, "Anisotropy of Co nanoparticles induced by swift heavy ions," Phys. Rev. B **67**, 220101 (2003).

[18]S. Roorda, T. van Dillen, A. Polman, C. Graf, A. van Blaaderen, and B. J. Kooi, "Aligned gold nanorods in silica made by ion irradiation of core–shell colloidal particles," Adv. Mater. **16**, 235–237 (2004).

[19]M. Toulemonde, W. Assmann, C. Dufour, A. Meftah, F. Studer, and C. Trautmann, "Experimental phenomena and thermal spike model description of ion tracks in amorphisable inorganic insulators," Mat. Fys. Med. **52**, 263–292 (2006).

[20]I. Lifshits, M. Kaganov, and L. Tanatarov, "On the theory of radiation-induced changes in metals," J. Nucl. Energy, Part A **12**, 69–78 (1960).

[21]S. Anisimov, B. Kapeliovich, T. Perelman et al., "Electron emission from metal surfaces exposed to ultrashort laser pulses," Zh. Eksp. Teor. Fiz. **66**, 375–377 (1974).

[22]A. Leino, S. Daraszewicz, O. H. Pakarinen, K. Nordlund, and F. Djurabekova, "Atomistic two-temperature modelling of ion track formation in silicon dioxide," Europhys. Lett. **110**, 16004 (2015).

[23]M. Laitinen, M. Rossi, J. Julin, and T. Sajavaara, "Time-of-flight—Energy spectrometer for elemental depth profiling—Jyväskylä design," Nucl. Instrum. Methods Phys. Res., Sect. B **337**, 55–61 (2014).

[24]PARCAS Computer code 1996–2021, available open source at https://gitlab.com/acclab/parcas/. The main principles of the molecular dynamics algorithms are presented by Nordlund et al. [K. Nordlund, M. Ghaly, R. Averback, M. Caturla, T. D. de La Rubia, and J. Tarus, "Defect production in collision cascades in elemental semiconductors and fcc metals," Phys. Rev. B **57**, 7556 (1998)] and Ghaly et al. [M. Ghaly, K. Nordlund, and R. S. Averback, "Molecular dynamics investigations of surface damage produced by kiloelectronvolt self-bombardment of solids," Philos. Mag. A **79**, 795–820 (1999)]. The adaptive time step and electronic stopping algorithms are the same as work by K. Nordlund ["Molecular dynamics simulation of ion ranges in the 1–100 keV energy range," Comput. Mater. Sci. **3**, 448–456 (1995)]. The 2016 version of the code is published in the supplementary material to F. Granberg, K. Nordlund, M. W. Ullah, K. Jin, C. Lu, H. Bei, L. Wang, F. Djurabekova, W. Weber, and Y. Zhang, "Mechanism of radiation damage reduction in equiatomic multicomponent single phase alloys," Phys. Rev. Lett. **116**, 135504 (2016).

[25]F. Djurabekova and K. Nordlund, "Atomistic simulation of the interface structure of Si nanocrystals embedded in amorphous silica," Phys. Rev. B **77**, 115325 (2008).

[26]M. Toulemonde, W. Assmann, C. Dufour, A. Meftah, F. Studer, and C. Trautmann, "Experimental phenomena and thermal spike model description of ion tracks in amorphisable inorganic insulators," Mat. Fys. Medd. **52**, 263–292 (2006).

[27]T. Watanabe, D. Yamasaki, K. Tatsumura, and I. Ohdomari, "Improved interatomic potential for stressed si, o mixed systems," Appl. Surf. Sci. **234**, 207–213 (2004).

[28]J. Samela, K. Nordlund, V. N. Popok, and E. E. Campbell, "Origin of complex impact craters on native oxide coated silicon surfaces," Phys. Rev. B **77**, 075309 (2008).

[29]S. Foiles, M. Baskes, and M. S. Daw, "Embedded-atom-method functions for the fcc metals Cu, Ag, Au, Ni, Pd, Pt, and their alloys," Phys. Rev. B **33**, 7983 (1986).

[30]S. Foiles, M. Baskes, and M. Daw, "Erratum: Embedded-atom-method functions for the fcc metals Cu, Ag, Au, Ni, Pd, Pt, and their alloys," Phys. Rev. B **37**, 10378 (1988).

[31]J. F. Ziegler and J. P. Biersack, "The stopping and range of ions in matter," in *Treatise on Heavy-Ion Science* (Springer, 1985), pp. 93–129.

[32]H. J. Berendsen, J. v. Postma, W. F. van Gunsteren, A. DiNola, and J. R. Haak, "Molecular dynamics with coupling to an external bath," J. Chem. Phys. **81**, 3684–3690 (1984).

[33]P. Mota-Santiago, F. Kremer, A. Nadzri, M. C. Ridgway, and P. Kluth, "Elongation of metallic nanoparticles at the interface of silicon dioxide and silicon nitride," Nucl. Instrum. Methods Phys. Res., Sect. B **409**, 328–332 (2017).

[34]F. Corni, A. Monelli, G. Ottaviani, R. Tonini, G. Queirolo, and L. Zanotti, "Radiation enhanced transport of hydrogen in SiO_2," J. Non-Cryst. Solids **216**, 71–76 (1997).

[35]G. Rizza, E. Dawi, A. Vredenberg, and I. Monnet, "Ion engineering of embedded nanostructures: From spherical to facetted nanoparticles," Appl. Phys. Lett. **95**, 043105 (2009).

[36]V. E. Jantunen, A. A. Leino, M. Veske, A. Kyritsakis, H. V. Muiños, K. Nordlund, and F. Djurabekova, "Interface effects on heat dynamics in embedded metal nanoparticles during swift heavy ion irradiation," J. Phys. D: Appl. Phys. **55**, 275301 (2022).

[37]G. Rizza, P. Coulon, V. Khomenkov, C. Dufour, I. Monnet, M. Toulemonde, S. Perruchas, T. Gacoin, D. Mailly, X. Lafosse *et al.*, "Rational description of the ion-beam shaping mechanism," Phys. Rev. B **86**, 035450 (2012).

SUPPLEMENTARY MATERIAL:Nanorod orientation control by swift heavy ion irradiation

Spyridon Korkos,[1,2] Ville Jantunen,[3] Kai Arstila,[1,2] Timo Sajavaara,[1,2] Aleksi Leino,[3] Kai Nordlund,[3] and Flyura Djurabekova[3]

[1)]*Accelerator Laboratory, Department of Physics, University of Jyvaskyla, P.O. Box 35, FI-40014 Jyvaskyla, Finland*

[2)]*Nanoscience Center, Department of Physics, University of Jyvaskyla, P.O. Box 35, FI-40014 Jyvaskyla, Finland*

[3)]*Department of Physics, University of Helsinki, P.O. Box 43, FI-00014 Helsinki, Finland*
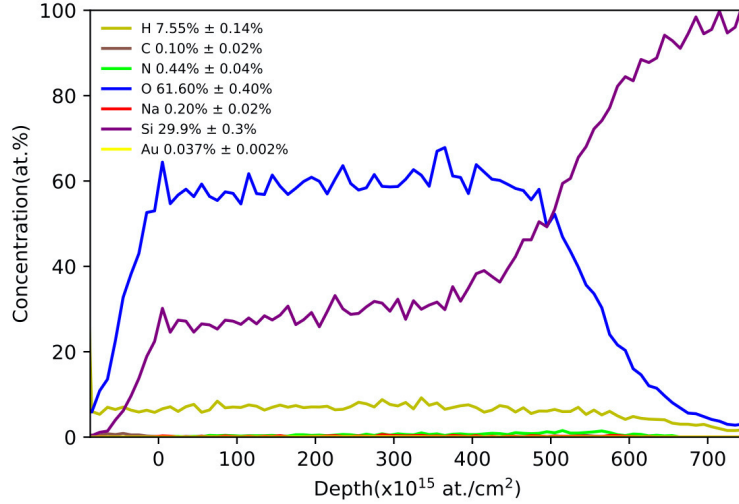
A. Elemental analysis of as grown samples

FIG. S1. ToF-ERDA depth profiles of Si-substrate/50 nm SiO_2/NRs/50 nm SiO_2 sample. At the left upper corner, the elemental concentrations are shown.

Since the elongation phenomenon may depend on the quality of the surrounding matrix[1], it is important to investigate the properties prior to irradiation. In the ToF-ERDA depth profiles (Fig. S1), we deduce that the elemental ratio O/Si was measured to be 2.04±0.02 which means that the as-grown silicon dioxide is very close to stoichiometric. Hydrogen and nitrogen impurities arise from the silane and nitrous oxide precursors, respectively, and sodium originates from the nanoparticles solution. All the other impurity concentrations are low (<0.5 at.%) except hydrogen. In our simulations, the system Au-SiO_2 is ideal where SiO_2 has the exact stoichiometry ratio (O/Si=2) and no impurities. Impurities are neglected in the simulations for practical reasons as inclusion of additional elements makes finding a working set of suitable potentials extremely difficult. Initial hydrogen concentration is fairly high (>7 at.%) but swift heavy ions are known to release some of it from silica[2]. However we note that MD simulations are not very sensitive and produce qualitatively similar results for different interatomic potentials and materials[3,4]. It is unlikely that hydrogen, even in this high concentrations, would change the conclusions.

B. Nanoparticle recrystallization in MD

To verify whether the modified shape of a nanoparticle retain during the slow cooling, with the cooling rate closer to the experimental value, we performed one independent simulation of
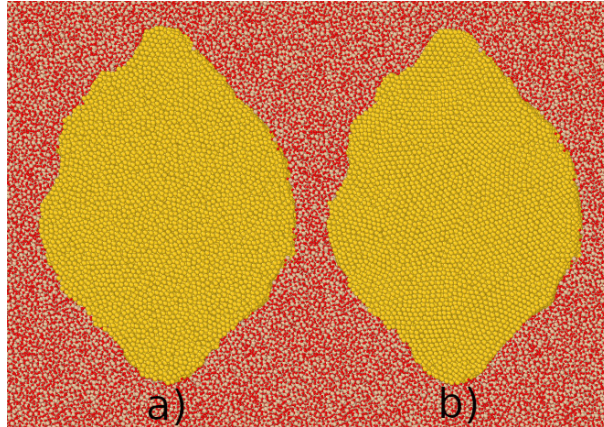
FIG. S2. a) Nanoparticle after irradiation in a molten state. b) Same nanoparticle as a) but after cooling down and allowing to crystallize.

nanoparticle relaxation after the impact. As can be seen in Fig. S2 embedded NPs conserve their shape almost perfectly when allowed to recrystallize in MD. This process took close to a nanosecond making it computationally $\sim$10 times as expensive as our method of running for 100 ps and extracting the shape and creating a new particle with the same shape.

Since recrystallization takes long time and results in strongly polycrystalline structure, we have adopted the same recrystallization model as in[4]. Namely, we extracted the shape of the nanorod after 100 ps simulation and scaled the volume while keeping the shape intact. Then we cut out a nanorod from the bulk fcc gold to the scaled shape to keep the same number of atoms. The recrystallized nanoparticle is then embedded to a pristine silica matrix using the same method as in the beginning of a new simulation. We use pristine silica matrix instead of the irradiated one since the ZBL potential used to describe the interactions in the interface may lead to formation of artificial gap between the nanorod and silica, since there is no attractive force in this potential. The gap might affect further development of shape modification and forcing the molten material fill in the empty gap around it. To overcome this problem in more realistic manner a better potential with some attractive interactions between the NP and silica must be used.

REFERENCES

[1]P. Mota-Santiago, F. Kremer, A. Nadzri, M. C. Ridgway, and P. Kluth, "Elongation of metallic nanoparticles at the interface of silicon dioxide and silicon nitride," Nuclear Instruments and

Methods in Physics Research Section B: Beam Interactions with Materials and Atoms **409**, 328–332 (2017).

[2]F. Corni, A. Monelli, G. Ottaviani, R. Tonini, G. Queirolo, and L. Zanotti, "Radiation enhanced transport of hydrogen in sio2," Journal of non-crystalline solids **216**, 71–76 (1997).

[3]H. Amekura, P. Kluth, P. Mota-Santiago, I. Sahlberg, V. Jantunen, A. Leino, H. Vazquez, K. Nordlund, and F. Djurabekova, "On the mechanism of the shape elongation of embedded nanoparticles," Nuclear Instruments and Methods in Physics Research Section B: Beam Interactions with Materials and Atoms **475**, 44–48 (2020).

[4]A. A. Leino, O. Pakarinen, F. Djurabekova, K. Nordlund, P. Kluth, and M. C. Ridgway, "Swift heavy ion shape transformation of au nanocrystals mediated by molten material flow and recrystallization," Materials Research Letters **2**, 37–42 (2014).

PII

SIZE DEPENDENT SWIFT HEAVY ION INDUCED Au NANOPARTICLE ELONGATION IN SiO$_2$ MATRIX

by

Spyridon Korkos, Kenichiro Mizohata, Sami Kinnunen, Timo Sajavaara & Kai Arstila

Size dependent swift heavy ion induced Au nanoparticle elongation in SiO$_2$ matrix

Spyridon Korkos,[1,2,a)] [ID] Kenichiro Mizohata,[3] [ID] Sami Kinnunen,[1,2] [ID] Timo Sajavaara,[1,2] [ID] and Kai Arstila[1,2] [ID]

AFFILIATIONS

[1]Accelerator Laboratory, Department of Physics, University of Jyvaskyla, P.O. Box 35, FI-40014 Jyvaskyla, Finland
[2]Nanoscience Center, Department of Physics, University of Jyvaskyla, P.O. Box 35, FI-40014 Jyvaskyla, Finland
[3]Department of Physics, University of Helsinki, P.O. Box 43, FI-00014 Helsinki, Finland

Note: This paper is part of the Special Topic on Radiation Effects in Materials.
[a)]**Author to whom correspondence should be addressed:** spyridon.s.korkos@jyu.fi

ABSTRACT

The elongation of spherical Au nanoparticles embedded in SiO$_2$ under swift heavy ion (SHI) irradiation is an extensively studied phenomenon. The use of a TEM grid as a substrate facilitates the identification of the same nanoparticle before and after the irradiation. Since the underdensification of SiO$_2$ inside the ion track plays a key role, the elongation is sensitive to the matrix material properties. Therefore, we studied the elongation process of SHI irradiated Au spherical nanoparticles of various diameters (5–80 nm) embedded either in atomic layer deposition (ALD) or plasma-enhanced chemical vapor deposition (PECVD) SiO$_2$. The results show that a different elongation ratio is achieved depending on the particle initial size, ion fluence, and a different SiO$_2$ deposition method. The embedded nanoparticles in ALD SiO$_2$ elongate roughly 100% more than the nanoparticles embedded in PECVD SiO$_2$ at the biggest applied fluence (5×10^{14} ions/cm^2). On the other hand, at fluences lower than 10^{14} ions/cm^2, nanoparticles elongate slightly more when they are embedded in PECVD SiO$_2$.

I. INTRODUCTION

The elongation of embedded metallic nanoparticles under swift heavy ion irradiation (SHII)[1] has attracted attention in nanoscience in the last few years. Compared to the standard nanofabrication techniques, such as electron beam lithography, ion implantation, or colloidal chemistry, with SHII, it is easy to fabricate precisely aligned nanorods.[2–10] The SHII method leads to the transformation of initially spherical nanoparticles to oriented nanorods as the ion beam shaping occurs in the form of elongation in the direction of the passing swift heavy ion.

The details of the exact mechanism behind this phenomenon as well as the different steps of the elongation process are under constant debate. A general description of the mechanism behind this phenomenon could be given in the following way. The ion forms a track in the host matrix, which leads to a decrease of density in the matrix (underdensification) above, below, and around the nanoparticle. After the passage of the ion through the nanoparticle, the nanoparticle melts and the molten metal flows to the track in the matrix, resulting in elongation after cooling and recrystallization.[11–13] Full elongation typically requires hundreds or

thousands of ion hits into the nanoparticle. Depending on the irradiation conditions (ion type, energy, flux, and fluence), the degree of elongation can be controlled.

One of the most promising applications for these elongated nanoparticles is in connection to their optical response.[14–17] The metallic nanostructures exhibit localized surface plasmon modes with a resonance frequency showing up a strong extinction peak in spectroscopic measurements. Within this resonance, the electric field near the nanoparticle is greatly enhanced, which yields many phenomena, such as surface-enhanced Raman scattering,[18] fluorescence,[19,20] or emission enhancement.[21] As a result, the elongated nanoparticles can act as "nanoantennas" and be used in various photonics applications,[22] such as photocatalysis, optical waveguides, and sensors.

Even if ion beam shaping has been intensively studied, the nanoparticle modification mechanism is not fully understood yet. Thus, monitoring of every step during this sample preparation procedure is needed in order to understand better this mechanism. So far, the experiments concerning the preparation of the samples have been limited to spherical metallic nanoparticles embedded in

only a few host matrices, including amorphous SiO_2,[1,3–5,7] amorphous Si_3N_4,[23–25] and sapphire (crystalline Al_2O_3).[15,26] The fabrication of the spherical nanoparticles has followed the standard techniques, i.e., electron beam lithography, ion implantation, and colloidal chemistry. Regarding the host matrices, the main deposition techniques include plasma-enhanced chemical vapor deposition (PECVD), sputtering, and thermal growth. During the irradiation, the samples are bombarded with swift heavy ions in the range of a few MeV until hundreds of MeV aiming at the elongation of the embedded nanoparticles. After the irradiation, the irradiated samples are then prepared for transmission electron microscopy (TEM) characterization in cross-sectional geometry by the standard focused ion beam (FIB) technique (TEM-lamella technique).

The TEM-lamella technique has the disadvantage that the same nanoparticle before and after the irradiation cannot be imaged. This leads to uncertainty if, for example, an elongated nanoparticle is the result of a single irradiated particle or several particles fused together when they are close to each other. In this study, this limitation of TEM lamella technology and the possibility to use a variation of nanoparticle sizes and shapes in one irradiation lead to the use of a 20 nm thick Si_3N_4 TEM window grid as a substrate. In addition, the required sample thickness for TEM imaging is limited to around 100 nm causing restrictions on the thickness of the host matrix. In the case of more than 100 nm sample thickness, a suitable etching technique, such as HF or precise RIE (reactive ion etching), can be applied to remove part of the matrix above the nanoparticles. Consequently, the comparison of the same nanoparticle before and after the irradiation can provide accurate information, necessary to the deeper understanding of the elongation process. In our very recent letter,[27] this approach was applied to study nanorod orientation due to ion irradiation.

Due to the requirement of matrix underdensification, it can be expected that the elongation is sensitive to the matrix material properties, including the composition, the density, and the concentration of impurities and nanoparticle coverage. Since the previous studies have shown that SiO_2 (gold nanoparticles in SiO_2 is the most studied system) ensures the biggest degree of elongation,[23,25] it is worth emphasizing that many SiO_2 fabrication techniques exist. For example, an atomic layer deposition (ALD) technique, which produces high quality films (uniform and conformal) with high precision of thickness, has not been investigated in connection with SHI irradiation. Since both PECVD and ALD belong to the category of depositions based on chemical reactions, it is worth investigating their different response on the SHI irradiation. Both deposition techniques are very widely used both in research and industry and, therefore, are readily available.

In this study, spherical Au nanoparticles of several diameters were embedded in SiO_2 deposited by ALD[28,29] or alternatively in SiO_2 deposited by PECVD[30] made on Si_3N_4 TEM window grids as substrates. The samples were irradiated by energetic heavy ion beams using several fluences. The purpose of this work was to study in detail the elongation of spherical nanoparticles under heavy ion irradiation in connection to their initial size and ion fluence. The effect of ALD deposited SiO_2 was compared to SiO_2 deposited by PECVD.

II. EXPERIMENTAL METHODS

A. Sample preparation

Two types of samples with SiO_2 films were fabricated using different deposition techniques. In the first type, the 50 nm of an SiO_2 film was first deposited using ALD at 200 °C on top of a TEM grid, with nine windows of 20 nm thick Si_3N_4. The ALD film was deposited with a Beneq TFS 200 cross-flow reactor using 150 Pa as the base pressure during the deposition. Nitrogen from an Inmatec PN 1150 nitrogen generator (99.999% purity) was used as a carrier gas as well as for purging between the precursor pulses. One ALD cycle consisted of subsequent pulses of (3-aminopropyl)-triethoxy-silane (APTES) (Sigma-Aldrich, 99%), de-ionized water, and O_3, which were used as precursors for the deposition. APTES was heated to 95 °C in order to provide sufficient vapor pressure while H_2O was kept at room temperature, and O_3 was produced with a BMT 803 N ozone generator from O_2.[28] One ALD cycle consisted of 1.25, 0.75, and 0.9 s pulses of APTES, H_2O, and O_3, respectively. Exposure time after each pulse was 20, 18, and 15 s, and purging times were 20, 15, and 15 s, respectively. In order to grow 50 nm thick SiO_2 films, one deposition consisted of 1250 cycles (36 h). The dispersion of the chemically synthesized Au spherical nanoparticles (manufactured by Sigma-Aldrich) was accomplished on top of the layer by dropcasting. The nanoparticles were mixed from different solutions (containing different sizes) into one, and then, they were deposited from one single dispersion. The nanoparticle diameter varied between 5 and 80 nm, with a 5 nm step. In order to embed the nanoparticles, another 50 nm SiO_2 thin film was deposited using ALD with the same parameters.

In the second type of samples, SiO_2 films were deposited using PECVD at 200 °C. A Plasmalab80Plus system, manufactured by Oxford Instruments, was used to deposit SiO_2 with silane (SiH_4 in Ar) and nitrous oxide (N_2O) as precursors. The chamber was pre-heated and purged with N_2 for 2 min. The working pressure during the process was 133 Pa. The growth rate of the deposited film was 50 nm/min.

Summarizing the structure of the samples, the total thickness was 120 nm, which fulfilled the requirements for TEM imaging. A set of samples were fabricated with an additional step of post-deposition annealing at 900 °C for 30 min with N_2 flow at a conventional furnace since the thermal treatment (annealing) is known to improve the SiO_2 film properties.[31,32] For comparison, Fig. 1 presents a macroscopic view of a TEM grid as well as optical microscope images of this grid.
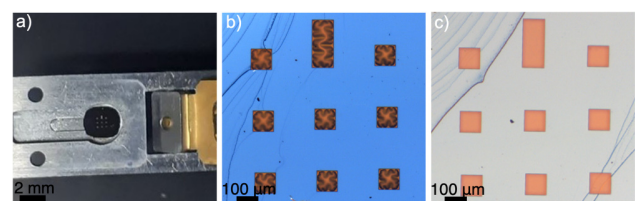

FIG. 1. (a) Photo of a TEM grid and optical microscope images of a TEM grid with SiO_2 deposited (b) by PECVD and (c) by ALD.
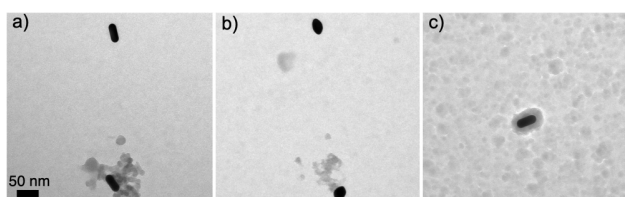
FIG. 2. TEM images of gold nanorods (a) before embedding them inside SiO_2 and (b) after embedding them inside SiO_2 deposited at 300 °C and the etching part of SiO_2. (c) TEM image of a gold nanorod after SiO_2 deposition at 200 °C.
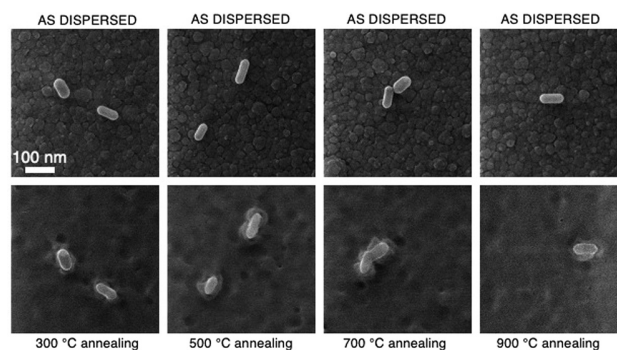

FIG. 3. Helium ion microscope (HIM) images of nanorods embedded in PECVD SiO_2 before and after annealing at various temperatures. The top images show nanorods before the deposition of the second layer on the top, and the bottom images show the same nanorods after annealing and etching of the excessive layer by RIE.

Additional Si substrate was present in the depositions in order to investigate the properties of grown SiO_2 films. Several material characterization techniques can be applied to study these properties as discussed later.

The selection of an SiO_2 deposition temperature depends on the temperature induced shape change of not embedded gold nanoparticles. Gold nanoparticles are observed to modify at 300 °C, leading to the conclusion of choosing a lower deposition temperature than 300 °C. Figures 2(a) and 2(b) show the shape change of the nanorods after SiO_2 deposition at 300 °C. As a result, lower deposition temperatures were tested, and deposition at 200 °C showed that nanorods do not significantly change shape [Fig. 2(c)].

The effect of the post-deposition annealing on the embedded nanoparticles was investigated as well. As seen in Fig. 3, in which gold nanorods on a bulk Si substrate are imaged before and after annealing at 900 °C and etching of top SiO_2, there is no significant change even after annealing at 900 °C.

B. Sample irradiation

The heavy ion irradiation of the samples was performed with 50 MeV $^{127}I^{9+}$ ions at the TAMIA 5 MV tandem accelerator at the Helsinki Accelerator Laboratory (University of Helsinki). The angle of incidence was 45°, and several fluences from 10^{13} to 5×10^{14} ions/cm^2 were applied at room temperature. During the irradiation, the beam was raster scanned over a 2×2 cm^2 area by magnetic deflectors, and the beam current was measured by a beam profilometer placed in front of the sample. The TEM grids were mounted on silver plates using a conductive carbon paste to avoid any damage by overheating during the irradiation. All of the nine windows in a TEM grid were covered by the beam spot area of 1 cm^2. However, at high enough fluences, there is a risk for the windows to break.

Similar experiments had been performed initially where SiO_2 films were so thick that the etching part of the SiO_2 layer was essential. On top of a TEM grid with nine windows of 20 nm thick Si_3N_4, a 30 nm PECVD SiO_2 film was the first deposited at 200 °C. Then, chemically synthesized Au spherical nanoparticles with diameter varying from 5 to 80 nm were dispersed on top of the film. Finally, another SiO_2 film with 200 nm thickness was deposited in order to embed the nanoparticles. For these samples with a thicker SiO_2 film, heavy ion irradiation was performed with a 383 MeV $^{84}Kr^{16+}$ beam from the K-130 cyclotron at the Jyväskylä

Accelerator Laboratory (University of Jyväskylä) in 45° incidence with several fluences at room temperature.

C. Sample characterization

The samples were imaged with a JEOL-JEM 1400 TEM operated at 120 kV. Before the irradiation, the samples were imaged from the top without tilting the TEM stage, but after the irradiation, the electron beam direction should be perpendicular to the ion beam direction to get the full information from an elongated nanoparticle.

Prior to irradiation of the samples with a Kr beam, the TEM imaging took place before the deposition of the second SiO_2 film. After the irradiation, around 150 nm of SiO_2 were etched by RIE to accomplish the TEM imaging. In Fig. 4, TEM images from a sample irradiated at the highest applied fluence (2×10^{14} ions/cm^2) are shown.
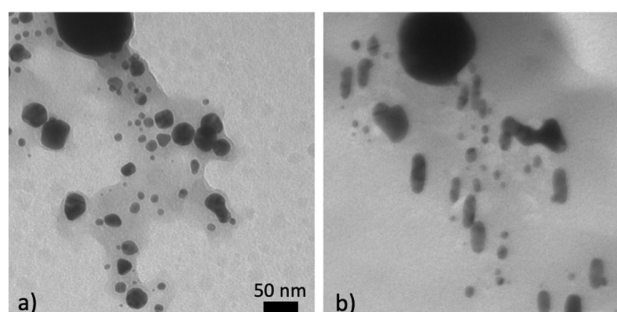

FIG. 4. TEM images of a 20 nm Si_3N_4/30 nm PECVD SiO_2/NPs/200 nm PECVD SiO_2 sample irradiated at 2×10^{14} ions/cm^2 fluence with 383 MeV ^{84}Kr ions. The images were taken (a) from the top before the irradiation and (b) perpendicular to the ion beam direction.
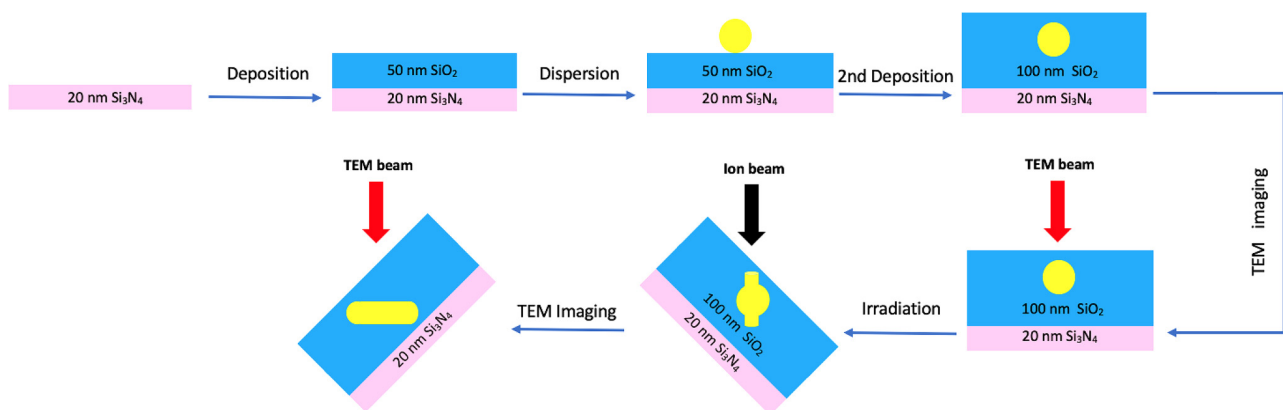
FIG. 5. Schematic representation of sample preparation, irradiation, and imaging using TEM.

It is obvious that there is information missing if this procedure is followed, such as how the nanoparticles are enclosed by the SiO_2 layer and the impact of the ion beam on the film since most of that has been removed. Consequently, these reasons and the fact that the additional film thickness does not affect significantly the elongation process led to the production of the samples with thickness thin enough to allow the TEM imaging without an etching step. All the steps of the procedure, where samples were irradiated with a ^{127}I beam, are shown in Fig. 5.

An image segmentation code was written with Python to measure the dimensions of the nanoparticles before and after the irradiation (Fig. 6).

A more detailed analysis of the film properties can be reached by means of advanced material characterization techniques,

FIG. 6. TEM images of the 900 °C annealed 20 nm Si_3N_4/50 nm ALD SiO_2/NPs/50 nm ALD SiO_2 sample irradiated with a 50 MeV ^{127}I beam at 5×10^{14} ions/cm^2 fluence, which were taken (a) from the top before the irradiation and (b) perpendicular to the ion beam direction. Corresponding segmented images (c) and (d).

including time-of-flight elastic recoil detection analysis (ToF-ERDA) and x-ray reflectivity (XRR). ToF-ERDA is an ion beam analysis technique capable of determining the composition of a thin film. ToF-ERDA measurements were accomplished with the use of a 1.7 MV Pelletron accelerator.[33] In measurements, a ^{63}Cu^{6+} beam of 11.9 MeV energy was used. The analysis of the measurements was done using the Potku software.[34]

XRR measurements were performed in order to reveal information about the thickness, density, and roughness of the SiO_2 films. A PANalytical X'Pert Pro Alpha 1 MPD x-ray powder diffractometer setup to x-ray reflectivity was used with a Cu Kα_1 x-ray source ($\lambda = 0.154\,056$ nm, V = 45 kV, I = 40 mA). The analysis of the samples was done with GenX open software. The experimental data are reproduced by changing simulation parameters, from which the values of the thickness, density, and roughness of the SiO_2 film were extracted.

III. RESULTS

A. Properties of SiO_2 films grown using PECVD and ALD

Already, the optical microscope images in Fig. 1 show a clear difference between TEM grids with ALD and PECVD SiO_2 coatings. ALD SiO_2 has a smooth surface, but in PECVD SiO_2, surface tensions appear. Another basic difference is the way nanoparticles are enclosed by the films. In Fig. 7, two images of nanoparticles embedded either in PECVD or in ALD before irradiation are shown. We observe that around the nanoparticles, an area of darker contrast has been formed, and possible explanation could be that the nanoparticles act as nucleation sites for the growth of SiO_2. These regions are much more pronounced in PECVD SiO_2, in which grains could be observed,[35] compared to more uniform ALD SiO_2.

The elemental composition of the samples was extracted from coincidence time-of-flight and energy data (Fig. 8). ToF-ERDA depth profiles are shown for annealed and as-deposited PECVD (Fig. 9) and ALD (Fig. 10) samples. Depth profiles for the as-deposited PECVD sample [Fig. 9(a)] show that the SiO_2 is
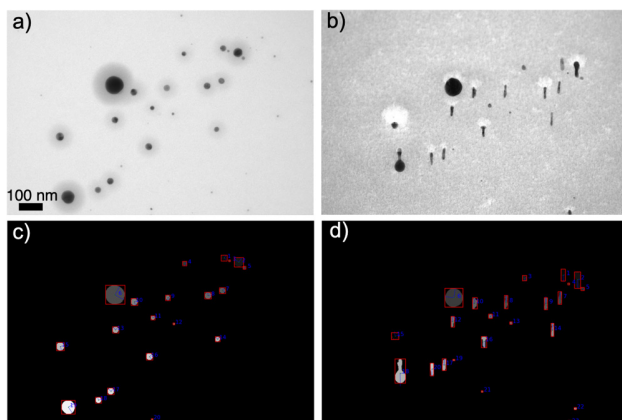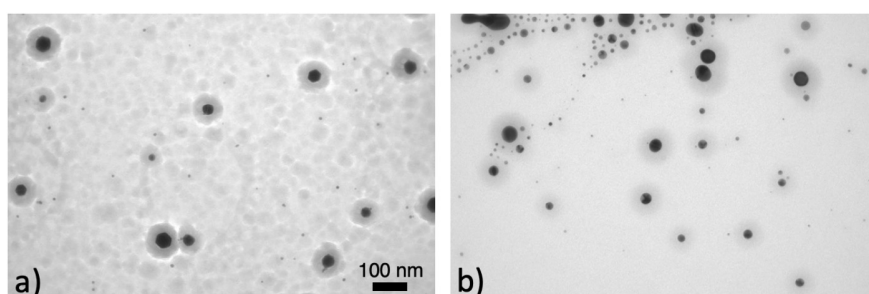
FIG. 7. TEM images of nanoparticles embedded in SiO₂ grown using (a) PECVD and (b) ALD.

stoichiometric with elemental ratio O/Si = 2.06 ± 0.02. Apart from silicon and oxygen, the film contains a significant amount of hydrogen impurity (7.6 at. %), which most probably originates from the silane precursor, and a small amount of other impurities, such as nitrogen (originated most likely from the nitrous oxide precursor), carbon, and sodium [coming from the phosphate buffer solution (PBS) of nanoparticles]. Gold can be detected as well because of the gold nanoparticles embedded inside. Depth profiles of an annealed PECVD sample [Fig. 9(b)] show that SiO₂ is oxygen poor with elemental ratio O/Si = 1.88 ± 0.02. Additionally, it contains a small amount of the same impurities as the as-deposited SiO₂, but hydrogen concentration has reduced significantly (<0.1 at. %).

The same behavior is visible in as-deposited and annealed ALD samples as well. Depth profiles for an as-deposited ALD sample [Fig. 10(a)] show that SiO₂ is nearly stoichiometric with elemental ratio O/Si = 2.07 ± 0.02. Regarding impurities, the film contains a significant amount of hydrogen (6.5 at. %) originating from APTES and

water precursors and a small amount of other impurities (less than 1 at. %), including nitrogen (originating from the APTES) and carbon. Gold is again visible in the film. Depth profiles of an annealed ALD sample [Fig. 10(b)] show that SiO₂ is stoichiometric with elemental ratio O/Si = 1.97 ± 0.02. It contains a small amount of the same impurities than as-deposited SiO₂, but hydrogen concentration has again dropped (<0.2 at. %). The number of gold nanoparticles embedded in SiO₂ (1.4×10^7–1.1×10^8 nanoparticles/cm²) was
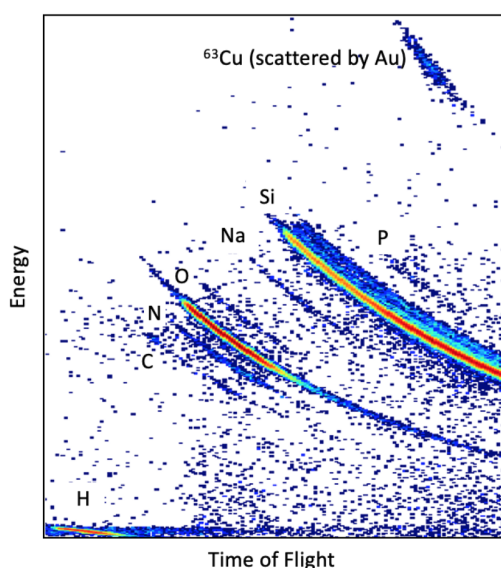

FIG. 8. Coincidence time-of-flight and an energy histogram of a ToF-ERDA measurement from an Si/50 nm PECVD SiO₂/NPs/50 nm PECVD SiO₂ as-deposited sample.
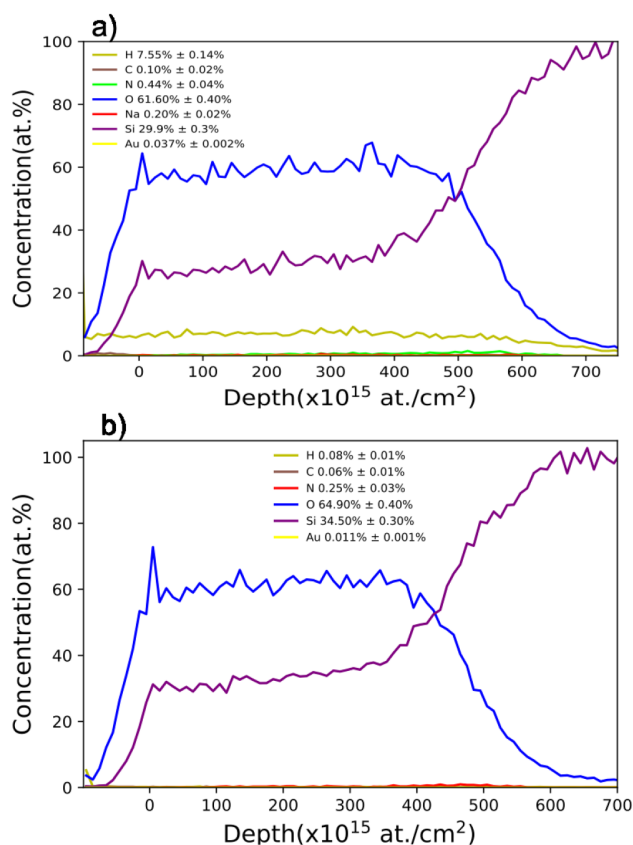

FIG. 9. ToF-ERDA depth profiles of an Si/50 nm PECVD SiO₂/NPs/50 nm PECVD SiO₂ (a) as-deposited sample and (b) annealed sample.
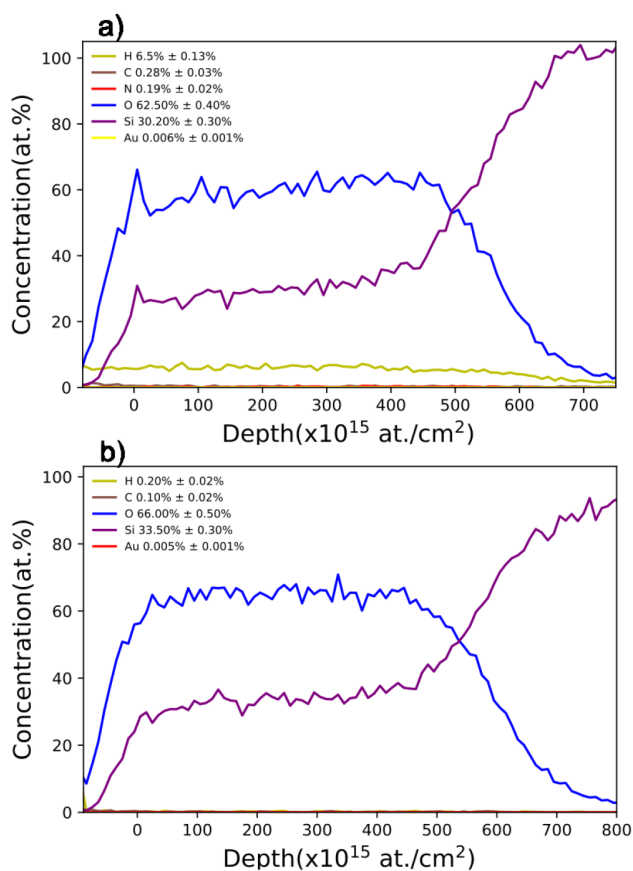
FIG. 10. ToF-ERDA depth profiles of an Si/50 nm ALD SiO$_2$/NPs/50 nm ALD SiO$_2$ (a) as-deposited sample and (b) annealed sample.
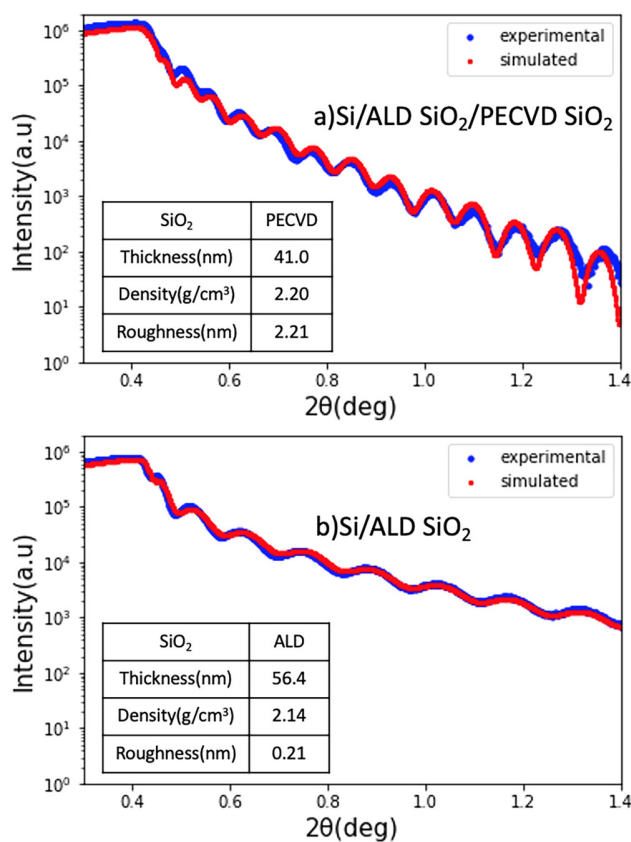

FIG. 11. Measured and simulated XRR curves of (a) an Si/50 nm ALD SiO$_2$/50 nm PECVD SiO$_2$ as-deposited sample and (b) an Si/50 nm ALD SiO$_2$ as-deposited sample. In each graph, there is a table with the measured quantities for each film.

calculated from atomic concentrations of gold for all the samples. This result tells that nanoparticles have a low average areal density covering less than 0.1% of the area.

In Fig. 11(a), the experimental and simulated curves from XRR data are shown for an Si/50 nm ALD SiO$_2$/50 nm PECVD SiO$_2$ sample. The density of PECVD SiO$_2$ was measured to be 2.20 $\pm$ 0.06 g/cm^3 and the roughness 2.21 $\pm$ 0.10 nm. The measured thickness was 41.0 $\pm$ 0.9 nm. In Fig. 11(b), the experimental and simulated curves obtained by XRR are shown for an Si/50 nm ALD SiO$_2$ sample. The density of ALD SiO$_2$ was measured to be 2.14 $\pm$ 0.05 g/cm^3 and the roughness 0.21 $\pm$ 0.09 nm. The measured thickness of the film was 56.4 $\pm$ 0.7 nm, which is close to the goal thickness. In order to get the information for the PECVD layer, we used the extracted parameters from the ALD-only fit and then we fit the PECVD layer.

B. Irradiation with a 50 MeV ^{127}I^{9+} beam

Several fluences between 10^{13} and 5×10^{14} ions/cm^2 were applied to investigate the evolution of the elongation of

nanoparticles embedded in SiO$_2$ deposited either by ALD or PECVD. Additionally, the annealing process before the irradiation was carried out in order to see if the change in the matrix properties has any impact on the irradiation results. In Fig. 12, the average elongation ratio (length/width) vs the initial nanoparticle diameter is presented for all the samples.

Initially, spherical nanoparticle diameters varied between 5 and 80 nm. During the images analysis, they were classified in the ranges of 5 nm, i.e., 5–10, 10–15, 15–20 nm, etc. The experimental results show that there is a variation in the nanoparticle shape change for the same initial size, which is in accordance with the earlier study.[25] The elongation ratio with uncertainties is shown in Tables I (PECVD SiO$_2$) and II (ALD SiO$_2$). A standard deviation of the measured variable was used to express the variation of the ratio from its mean value. The number of particles in different size ranges varied between 10 and 100. Figures 13–19 show nanoparticles with the highest elongation ratio in each range before and after irradiation.

Single nanoparticles irradiated at lower fluences ($\leq 10^{14}$ ions/cm^2) are shown either from the as-deposited samples
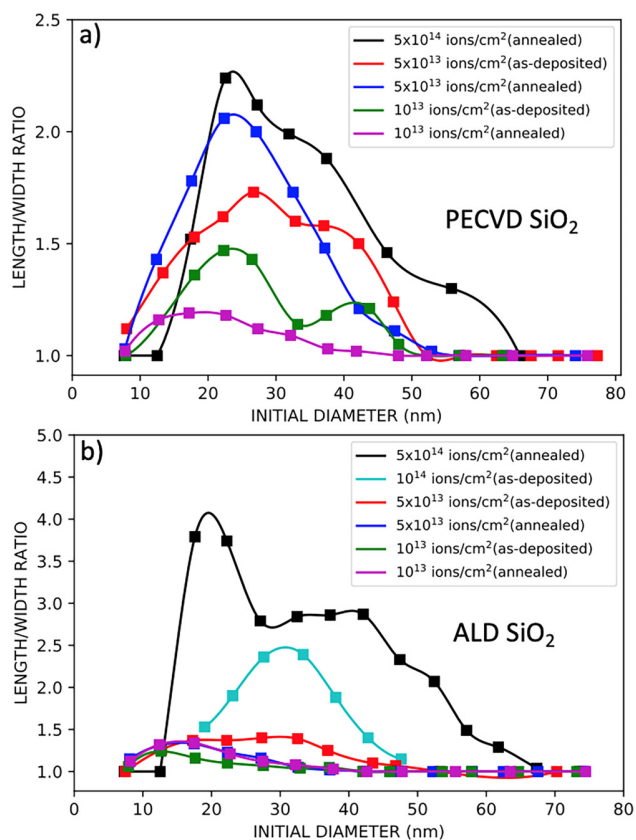
FIG. 12. Representation of the average ratio (length/width) vs the initial diameter of the elongated nanoparticles after 50 MeV ^{127}I irradiation at fluences between 10^{13} and 5×10^{14} ions/cm^2. The nanoparticles are embedded in (a) PECVD SiO$_2$ and (b) ALD SiO$_2$. The uncertainties are left out from the image for clarity.

or from the annealed samples in Figs. 13–17. Comparing the annealed and as-deposited samples at the same fluence, the elongation ratio is similar. Moreover, regarding the different deposition techniques, elongated nanoparticles in PECVD samples present a slightly higher elongation ratio for fluences $\leq 5 \times 10^{13}$ ions/cm^2.

The as-deposited PECVD and ALD samples did not withstand irradiation for the highest fluence at 5×10^{14} ions/cm^2, and most of the windows broke during the irradiation. The same problem appeared also for the annealed PECVD sample as we were able to track only a few nanoparticles after irradiation. As a result, images were collected from nanoparticles that had not been imaged before the irradiation. For the pre-imaged nanoparticles, the volume was almost the same before and after irradiation. In case the original nanoparticle was not imaged, we assumed the volume of the elongated nanoparticles as a cylinder and compared it with their spherical volume before the irradiation in order to find their initial diameter. As for the annealed ALD sample, it had intact windows with plenty of same nanoparticles imaged before and after the irradiation with TEM.

In Figs. 18 and 19, those nanoparticles with the highest elongation ratio in each range are shown. For the PECVD sample, only a few nanoparticles before the irradiation are shown. Comparing the different deposition techniques, the highest elongation ratio is achieved for ALD samples. However, the nanorods embedded in ALD SiO$_2$ elongate so much that some of them become unstable and tend to break up into smaller fragments, which has also been reported before[36] and is related to the inverse Ostwald ripening.[37–40]

Particularly, some of the biggest elongated nanoparticles in ALD SiO$_2$ (after 35 nm initial diameter) present unconventional morphologies. Between 35 and 45 nm initial diameter, the irradiated nanoparticles have obtained a shape resembling nanorod. One nanoparticle (35–40 nm) is bigger in the sides than in the middle, while the other is bigger in one side. Subsequently, for nanoparticles with diameters between 45 and 65 nm, the irradiation causes only part of them to elongate.

By increasing the fluence, the elongation ratio of the nanoparticles (Fig. 20) increases and the biggest nanoparticles also change.

TABLE I. Elongation (length/width) ratio for nanoparticles embedded in annealed (ann.) and as-deposited (as-dep.) PECVD SiO$_2$ samples regarding the initial diameter and fluence.

(nm)	10^{13} (ann.)	10^{13} (as-dep.)	5×10^{13} (ann.)	5×10^{13} (as-dep.)	5×10^{14} (ann.)
5–10	1.02 ± 0.02	1.00 ± 0.00	1.03 ± 0.03	1.12 ± 0.12	1.0 ± 0.0
10–15	1.16 ± 0.12	...	1.43 ± 0.22	1.37 ± 0.29	1.0 ± 0.0
15–20	1.19 ± 0.09	1.36 ± 0.32	1.78 ± 0.38	1.53 ± 0.30	1.52 ± 0.52
20–25	1.18 ± 0.10	1.47 ± 0.45	2.06 ± 0.35	1.62 ± 0.38	2.24 ± 0.70
25–30	1.12 ± 0.06	1.43 ± 0.38	2.00 ± 0.38	1.73 ± 0.32	2.12 ± 0.32
30–35	1.09 ± 0.07	1.14 ± 0.14	1.73 ± 0.34	1.60 ± 0.29	1.99 ± 0.54
35–40	1.03 ± 0.03	1.18 ± 0.18	1.48 ± 0.17	1.58 ± 0.26	1.88 ± 0.43
40–45	1.02 ± 0.02	1.21 ± 0.20	1.21 ± 0.13	1.50 ± 0.39	...
45–50	1.05 ± 0.05	1.0 ± 0.0	1.11 ± 0.11	1.24 ± 0.20	1.46 ± 0.05
50–60	1.0 ± 0.0	1.0 ± 0.0	1.0 ± 0.0	1.0 ± 0.0	1.30 ± 0.30
60–70	1.0 ± 0.0	1.0 ± 0.0	1.0 ± 0.0	1.0 ± 0.0	1.0 ± 0.0
70–80	1.0 ± 0.0	...	1.0 ± 0.0	1.0 ± 0.0	...

TABLE II. Elongation (length/width) ratio for nanoparticles embedded in annealed (ann.) and as-deposited (as-dep.) ALD SiO$_2$ samples regarding the initial diameter and fluence.

(nm)	10^{13} (ann.)	10^{13} (as-dep.)	5×10^{13} (ann.)	5×10^{13} (as-dep.)	10^{14} (as-dep.)	5×10^{14} (ann.)
5–10	1.12 ± 0.12	1.06 ± 0.06	1.15 ± 0.15	1.0 ± 0.0	…	1.0 ± 0.0
10–15	1.32 ± 0.14	1.24 ± 0.12	1.31 ± 0.24	1.26 ± 0.20	…	1.0 ± 0.0
15–20	1.34 ± 0.19	1.16 ± 0.09	1.33 ± 0.15	1.37 ± 0.21	1.53 ± 0.0	3.79 ± 1.82
20–25	1.21 ± 0.11	1.10 ± 0.08	1.23 ± 0.14	1.37 ± 0.23	1.90 ± 0.05	3.74 ± 1.61
25–30	1.12 ± 0.10	1.07 ± 0.07	1.16 ± 0.08	1.40 ± 0.17	2.36 ± 0.17	2.84 ± 1.03
30–35	1.08 ± 0.07	1.04 ± 0.04	1.05 ± 0.05	1.39 ± 0.12	2.39 ± 0.26	2.86 ± 1.25
35–40	1.03 ± 0.03	1.05 ± 0.05	1.03 ± 0.03	1.25 ± 0.18	1.88 ± 0.05	2.86 ± 1.25
40–45	1.0 ± 0.0	1.0 ± 0.0	1.0 ± 0.0	1.10 ± 0.05	1.40 ± 0.25	2.87 ± 0.89
45–50	1.0 ± 0.0	1.0 ± 0.0	1.0 ± 0.0	1.07 ± 0.07	1.15 ± 0.04	2.33 ± 0.53
50–55	1.0 ± 0.0	1.0 ± 0.0	1.0 ± 0.0	1.0 ± 0.0	…	2.07 ± 0.74
55–60	1.0 ± 0.0	1.0 ± 0.0	1.0 ± 0.0	1.0 ± 0.0	…	1.49 ± 0.49
60–65	1.0 ± 0.0	1.0 ± 0.0	1.0 ± 0.0	1.0 ± 0.0	…	1.29 ± 0.26
65–70	1.0 ± 0.0	1.0 ± 0.0	1.0 ± 0.0	1.0 ± 0.0	…	1.04 ± 0.04
70–80	1.0 ± 0.0	1.0 ± 0.0	1.0 ± 0.0	1.0 ± 0.0	…	1.0 ± 0.0

The threshold fluence for larger elongation is higher for ALD samples than PECVD. Additionally, smaller nanoparticles elongate slightly more in both cases.

IV. DISCUSSION

A. Dependence of elongation on fluence and nanoparticle initial size

The results show that the elongation depends strongly on the irradiation fluence and the nanoparticle initial size. The lower fluences ($\leq 5 \times 10^{13}$ ions/cm^2) favor the elongation of the smallest nanoparticles, smaller than 50 nm, because the deposited energy is not high enough to elongate the larger ones. On the other hand, for higher fluences ($\geq 10^{14}$ ions/cm^2), the deposited energy by the ion irradiation is high enough to elongate bigger nanoparticles as well. However, when the smallest nanoparticles (<15 nm), which have already started elongating, reach the higher fluences, they start to shrink and reshape back toward a spherical shape or they can disintegrate completely. This significant volume change can be explained by the fact that the irradiation fluence is too high and prevent them from elongation. According to Peña-Rodríguez et al.,[41] the constituent atoms of the disintegrated nanoparticles are absorbed by the larger ones (Ostwald ripening) or form new particles, but there is no experimental evidence of that in the present study. In the case of nanoparticles with a diameter smaller than 10 nm, there is basically no elongation and only a few nanoparticles show a small shape change.

The last observation can be related to the value of the ion track diameter. If the nanoparticle has a diameter less than the ion track diameter, it cannot elongate or elongate much less than the bigger ones.[42] The track diameter limits as well the minimum width that an elongated nanoparticle can reach. According to Mota-Santiago et al.,[25] the diameter of an ion track formed in SiO$_2$
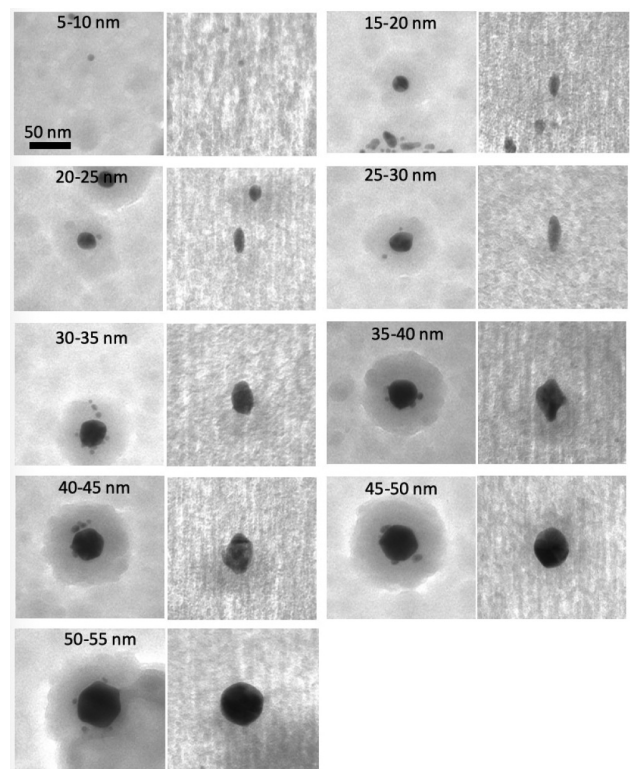

FIG. 13. TEM images of nanoparticles sandwiched between two 50 nm PECVD SiO$_2$ layers (as-deposited). The samples were irradiated with ^{127}I at a fluence of 10^{13} ions/cm^2 and imaged before (left) and after (right) the irradiation.
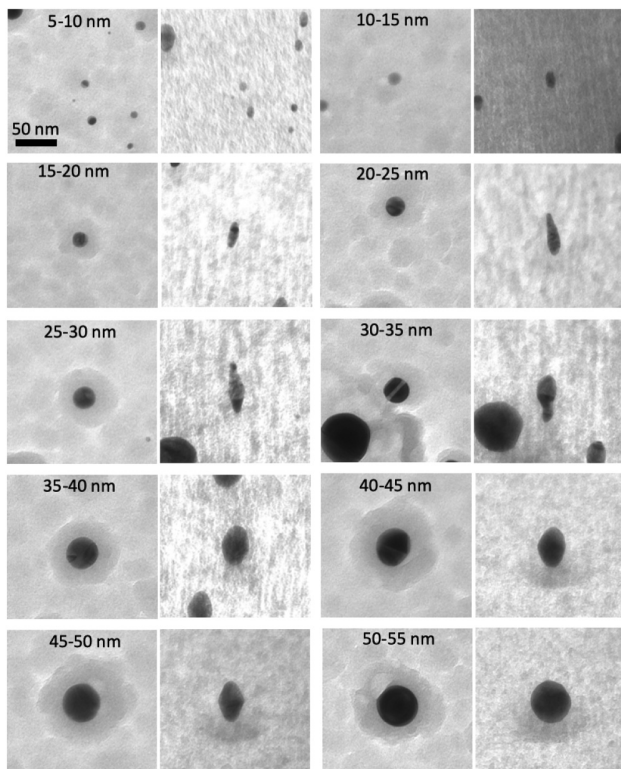
FIG. 14. TEM images of nanoparticles sandwiched between two 50 nm PECVD SiO$_2$ layers (annealed after the deposition). The samples were irradiated with ^{127}I at a fluence of 5×10^{13} ions/cm^2 before (left) and after (right) the irradiation.

FIG. 15. TEM images of nanoparticles sandwiched between two 50 nm ALD SiO$_2$ layers (annealed after deposition). The samples were irradiated with ^{127}I at a fluence of 10^{13} ions/cm^2 before (left) and after (right) the irradiation.

irradiated with a 185 MeV Au beam was measured to be 10.8 nm by SAXS (small angle x-ray scattering) measurements. In this study, nanoparticles of diameter between 7 and 8 nm are the smallest that can elongate and minimum elongation width was found to have approximately the same value. This observation, in combination with the smaller deposited energy in these experiments, implies that the ion track diameter for 50 MeV ^{127}I is less than the 10.8 nm reported in the literature. Additionally, their small size and consequently a small possibility of a significant amount of ions hitting them (8–40 ion hits/10^{13}–5×10^{13} ions/cm^2) affect the elongation.

Elongation results can give additional information about the correlation between the initial particle size and the particle deformation path in the SiO$_2$ matrix.[7] At the highest applied fluence, nanoparticles of diameter less than 15 nm disintegrate either completely and disappear or disintegrate partially and remain spherical. At range from a 15 to 45 nm diameter, they melt completely during the ion impact and transform to nanorods along the ion beam direction after multiple impacts. At range from 45 to 65 nm, they are partially molten and the elongation occurs as an elongated part attached to a sphere. Finally, for larger nanoparticles
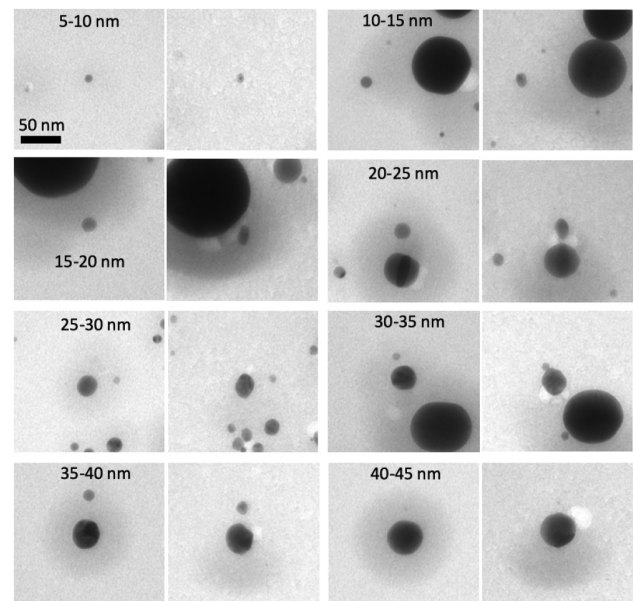
(>65 nm), there is negligible deformation because the ion energy is not high enough to melt them. Comparing these results with Rizza's work,[7] nanoparticles of diameter up to 30 nm are completely molten, while in our case, nanoparticles of diameter up to 45 nm melt completely. This difference arises from the composition of the matrix and the irradiation conditions. In this kind of studies, SiO$_2$ thickness does not need to be hundreds of nanometers like in previous studies,[7,17,23,25] but 100 nm thickness is enough.

B. Effect of the SiO$_2$ deposition technique

It is clear that the elongation is affected by the deposition technique of SiO$_2$. At the highest applied fluence, ALD SiO$_2$ offers a higher elongation ratio than PECVD SiO$_2$. At lower fluences, the opposite happens. This could be at least partially explained by the fact that PECVD SiO$_2$ has a slightly higher density than the ALD SiO$_2$ and the presence of grains in PECVD SiO$_2$. When an irradiated material is denser, bigger energy loss occurs, resulting in greater deposited energy in the material and consequently greater elongation. Apart from the difference in the overall density between the two types of SiO$_2$, the dark halos surrounding the nanoparticles can be interpreted as regions with a higher density. Since these regions are much more distinct in PECVD SiO$_2$ than in ALD SiO$_2$, we assume that this layer has such a density, which enables the nanoparticle to elongate more in PECVD SiO$_2$. As a result, the underdensification happens faster in PECVD SiO$_2$ than in ALD SiO$_2$ until the fluence of 5×10^{13}. However, the elongation of nanoparticles embedded in PECVD SiO$_2$ saturates faster: for

FIG. 16. TEM images of nanoparticles sandwiched between two 50 nm ALD SiO_2 layers (as-deposited). The samples were irradiated with ^{127}I at a fluence of 5×10^{13} ions/cm^2 before (left) and after (right) the irradiation.
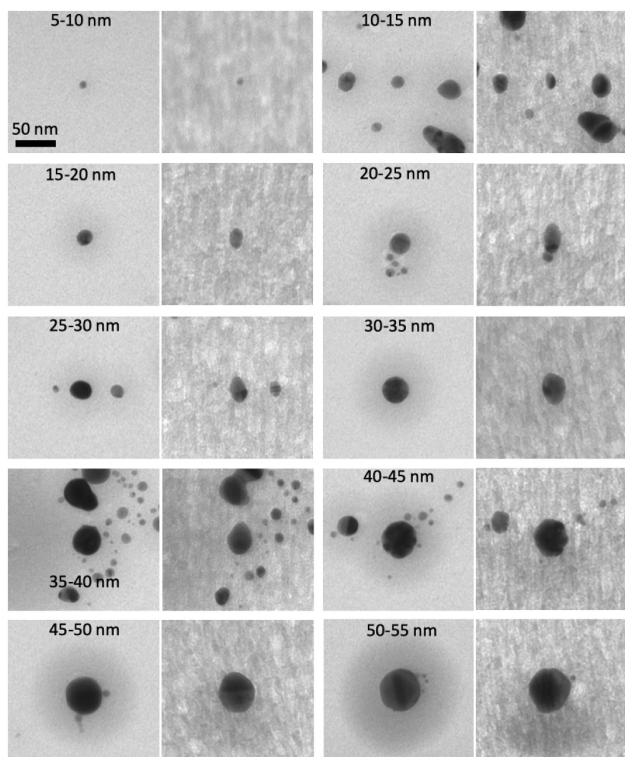

FIG. 17. TEM images of nanoparticles sandwiched between two 50 nm ALD SiO_2 layers (as-deposited). The samples were irradiated with ^{127}I at 10^{14} ions/cm^2 before (left) and after (right) the irradiation.

5×10^{14} ions/cm^2 fluence, there is only a small increase in the elongation ratio compared to 5×10^{13} ions/cm^2 fluence. On the other hand, for ALD, the elongation ratio is significantly higher at 5×10^{14} ions/cm^2 fluence compared to 10^{14} ions/cm^2 fluence and to a PECVD sample at 5×10^{14} ions/cm^2 fluence. These findings imply that in the range between 5×10^{13} and 5×10^{14} ions/cm^2, the underdensification happens faster within the ALD type. The dark halos surrounding the nanoparticles in a PECVD type in combination with the grains appearing in this make the nanoparticles elongate less in PECVD type than in ALD, and the underdensification happens slower at the higher fluences.

C. Effect of annealing

Finally, regarding the effect of the annealing prior to irradiation, there is no significant difference in the elongation ratio at lower fluences. The biggest difference is observed at the highest applied fluence where the as-deposited sample seems not to withstand irradiation as almost all the windows were broken after the irradiation. The reason could be that annealing makes the material sustain more easily the plastic deformation during the irradiation and not break. The annealing step makes the SiO_2 coated TEM grids more durable.
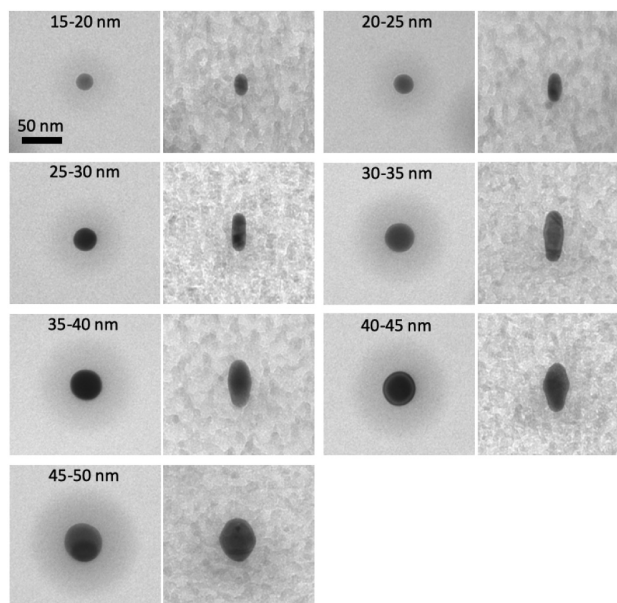

FIG. 18. TEM images of nanoparticles sandwiched between two 50 nm PECVD SiO_2 layers (annealed after the deposition). The samples were irradiated with ^{127}I at a fluence of 5×10^{14} ions/cm^2 before and after the irradiation. The red outline includes either a pair of nanoparticles before (left) and after (right) the irradiation or only nanoparticles after the irradiation.
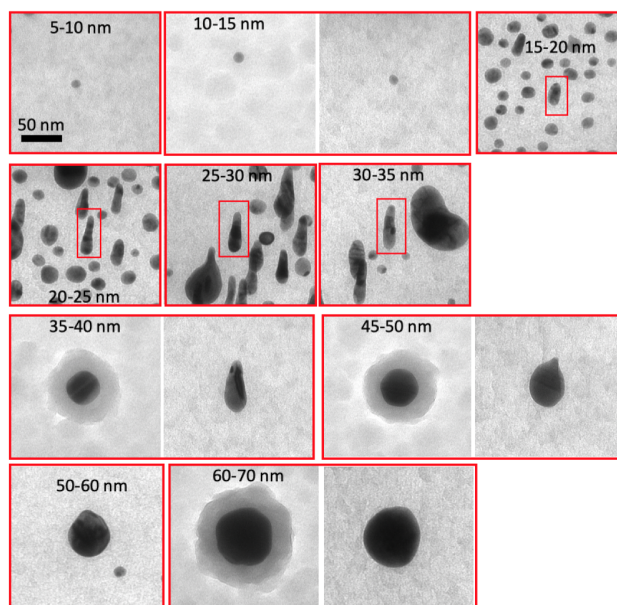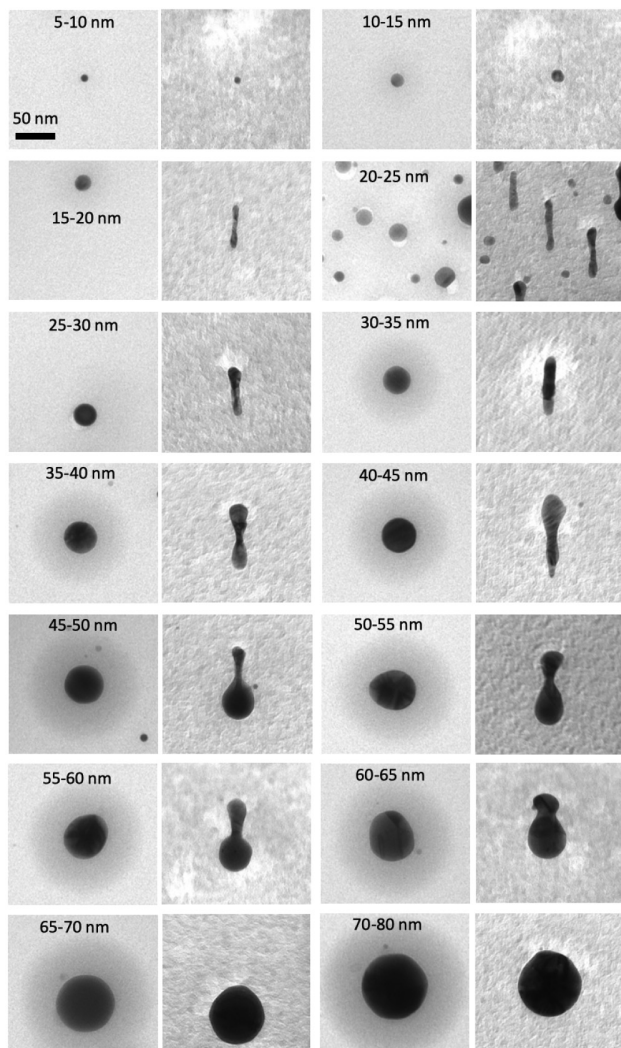
FIG. 19. TEM images of nanoparticles sandwiched between two 50 nm ALD SiO$_2$ layers (annealed after the deposition). The samples were irradiated with ^{127}I at a fluence of 5×10^{14} ions/cm^2 before (left) and after (right) the irradiation.

FIG. 20. Evolution of the elongation ratio with increasing fluence for two different nanoparticle sizes in (a) PECVD SiO$_2$ and (b) ALD SiO$_2$.

V. CONCLUSIONS

In this work, we investigated in detail the elongation of spherical gold nanoparticles of various diameters by imaging the same nanoparticles before and after the SHI irradiation. The deposition of SiO$_2$ by two techniques (ALD and PECVD) in combination with post-deposition annealing showed that the impact of the irradiation on nanoparticles depends on the deposition process of the samples, the quality of the SiO$_2$, and the size of the nanoparticles. Furthermore, the use of 20 nm Si$_3$N$_4$ TEM windows as a substrate makes it easier to 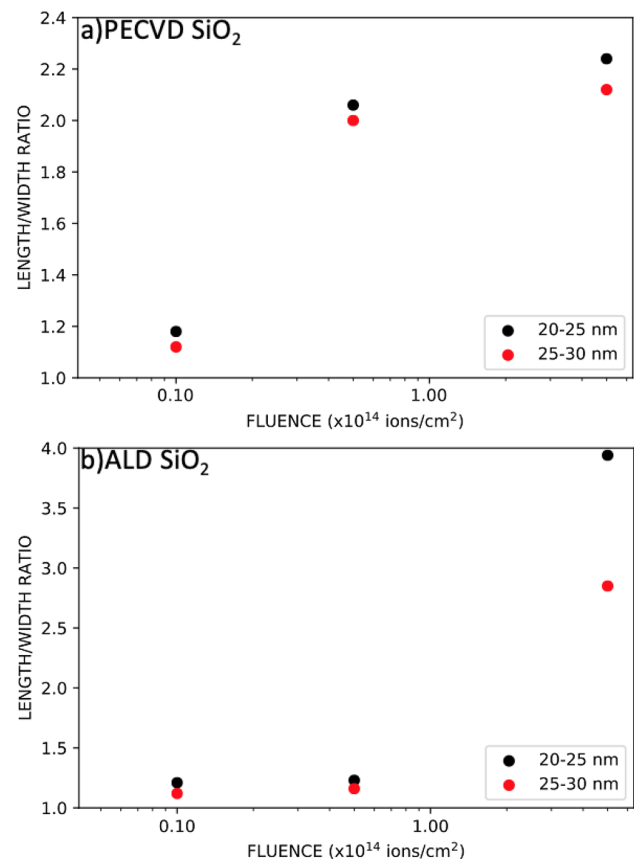study in detail the irradiation effect on nanostructures. Nanostructures of various sizes and shapes can be fabricated and imaged within the same sample in different phases of the processing, and their evolution can be followed.

ACKNOWLEDGMENTS

AUTHOR DECLARATIONS

Conflict of Interest

The authors have no conflicts to disclose.

Author Contributions

Spyridon Korkos: Conceptualization (lead); Investigation (lead); Methodology (lead); Software (lead); Validation (lead); Visualization (lead); Writing – original draft (lead).

Kenichiro Mizohata: Investigation (supporting). **Sami Kinnunen:** Investigation (supporting). **Timo Sajavaara:** Writing – review and editing (supporting). **Kai Arstila:** Conceptualization (equal); Investigation (equal).

DATA AVAILABILITY

REFERENCES

[1]C. d'Orléans, J. Stoquert, C. Estournes, C. Cerruti, J. Grob, J. Guille, F. Haas, D. Muller, and M. Richard-Plouet, "Anisotropy of Co nanoparticles induced by swift heavy ions," Phys. Rev. B **67**, 220101 (2003).

[2]S. Roorda, T. van Dillen, A. Polman, C. Graf, A. van Blaaderen, and B. J. Kooi, "Aligned gold nanorods in silica made by ion irradiation of core–shell colloidal particles," Adv. Mater. **16**, 235–237 (2004).

[3]Y. Mishra, F. Singh, D. Avasthi, J. Pivin, D. Malinovska, and E. Pippel, "Synthesis of elongated Au nanoparticles in silica matrix by ion irradiation," Appl. Phys. Lett. **91**, 063103 (2007).

[4]R. Giulian, P. Kluth, L. Araujo, D. Sprouster, A. Byrne, D. Cookson, and M. C. Ridgway, "Shape transformation of Pt nanoparticles induced by swift heavy-ion irradiation," Phys. Rev. B **78**, 125413 (2008).

[5]K. Awazu, X. Wang, M. Fujimaki, J. Tominaga, H. Aiba, Y. Ohki, and T. Komatsubara, "Synthesis of elongated Au nanoparticles in silica matrix by ion irradiation," Phys. Rev. B **78**, 054102 (2008).

[6]E. Dawi, A. Vredenberg, G. Rizza, and M. Toulemonde, "Ion-induced elongation of gold nanoparticles in silica by irradiation with Ag and Cu swift heavy ions: Track radius and energy loss threshold," Nanotechnology **22**, 215607 (2011).

[7]G. Rizza, P. E. Coulon, V. Khomenkov, C. Dufour, I. Monnet, M. Toulemonde, S. Perruchas, T. Gacoin, D. Mailly, X. Lafosse, C. Ulysse, and E. A. Dawi, "Rational description of the ion-beam shaping mechanism," Phys. Rev. B **86**, 035450 (2012).

[8]H. Amekura, S. Mohapatra, U. Singh, S. Khan, P. Kulriya, N. Ishikawa, N. Okubo, and D. Avasthi, "Shape elongation of Zn nanoparticles in silica irradiated with swift heavy ions of different species and energies: Scaling law and some insights on the elongation mechanism," Nanotechnology **25**, 435301 (2014).

[9]P.-E. Coulon, J. Amici, M.-C. Clochard, V. Khomenkov, C. Dufour, I. Monnet, C. Grygiel, S. Perruchas, C. Ulysse, L. Largeau, and G. Rizza, "Ion-shaping of embedded gold hollow nanoshells into vertically aligned prolate morphologies," Sci. Rep. **6**, 1 (2016).

[10]R. Li, K. Narumi, A. Chiba, Y. Hirano, D. Tsuya, S. Yamamoto, Y. Saitoh, N. Okubo, N. Ishikawa, C. Pang, F. Chen, and H. Amekura, "Matrix-material dependence on the elongation of embedded gold nanoparticles induced by 4 MeV C60 and 200 MeV Xe ion irradiation," Nanotechnology **31**, 265606 (2020).

[11]A. A. Leino, O. Pakarinen, F. Djurabekova, K. Nordlund, P. Kluth, and M. C. Ridgway, "Swift heavy ion shape transformation of Au nanocrystals mediated by molten material flow and recrystallization," Mater. Res. Lett. **2**, 37–42 (2014).

[12]T. Vu, C. Dufour, V. Khomenkov, A. Leino, F. Djurabekova, K. Nordlund, P.-E. Coulon, G. Rizza, and M. Hayoun, "Elongation mechanism of the ion shaping of embedded gold nanoparticles under swift heavy ion irradiation," Nucl. Instrum. Methods Phys. Res., Sect. B **451**, 42–48 (2019).

[13]H. Amekura, P. Kluth, P. Mota-Santiago, I. Sahlberg, V. Jantunen, A. Leino, H. Vazquez, K. Nordlund, and F. Djurabekova, "On the mechanism of the shape elongation of embedded nanoparticles," Nucl. Instrum. Methods Phys. Res., Sect. B **475**, 44–48 (2020).

[14]H. Amekura, N. Ishikawa, N. Okubo, M. C. Ridgway, R. Giulian, K. Mitsuishi, Y. Nakayama, C. Buchal, S. Mantl, and N. Kishimoto, "Zn nanoparticles irradiated with swift heavy ions at low fluences: Optically-detected shape elongation induced by nonoverlapping ion tracks," Phys. Rev. B **83**, 205401 (2011).

[15]O. Sánchez-Dena, P. Mota-Santiago, L. Tamayo-Rivera, E. García-Ramírez, A. Crespo-Sosa, A. Oliver, and J.-A. Reyes-Esqueda, "Size-and shape-dependent nonlinear optical response of Au nanoparticles embedded in sapphire," Opt. Mater. Express **4**, 92–100 (2014).

[16]A. Slablab, T. J. Isotalo, J. Mäkitalo, L. Turquet, P.-E. Coulon, T. Niemi, C. Ulysse, M. Kociak, D. Mailly, G. Rizza, and M. Kauranen, "Fabrication of ion-shaped anisotropic nanoparticles and their orientational imaging by second-harmonic generation microscopy," Sci. Rep. **6**, 37469 (2016).

[17]H. Amekura, K. Narumi, A. Chiba, Y. Hirano, K. Yamada, D. Tsuya, S. Yamamoto, N. Okubo, N. Ishikawa, and Y. Saitoh, "C_{60} ions of 1 MeV are slow but elongate nanoparticles like swift heavy ions of hundreds MeV," Sci. Rep. **9**, 14980 (2019).

[18]S. Schlücker, "Surface-enhanced Raman spectroscopy: Concepts and chemical applications," Angew. Chem. Int. Ed. **53**, 4756–4795 (2014).

[19]F. Tam, G. P. Goodrich, B. R. Johnson, and N. J. Halas, "Plasmonic enhancement of molecular fluorescence," Nano Lett. **7**, 496–501 (2007).

[20]P. Bharadwaj, B. Deutsch, and L. Novotny, "Optical antennas," Adv. Opt. Photonics **1**, 438–483 (2009).

[21]C. Clavero, "Plasmon-induced hot-electron generation at nanoparticle/metal-oxide interfaces for photovoltaic and photocatalytic devices," Nat. Photonics **8**, 95 (2014).

[22]R. Li, C. Pang, Z. Li, and F. Chen, "Plasmonic nanoparticles in dielectrics synthesized by ion beams: Optical properties and photonic applications," Adv. Opt. Mater. **8**, 1902087 (2020).

[23]P. Mota-Santiago, F. Kremer, A. Nadzri, M. C. Ridgway, and P. Kluth, "Elongation of metallic nanoparticles at the interface of silicon dioxide and silicon nitride," Nucl. Instrum. Methods Phys. Res., Sect. B **409**, 328–332 (2017).

[24]E. Dawi, W. ArnoldBik, R. Ackermann, and F. Habraken, "Shaping of Au nanoparticles embedded in various layered structures by swift heavy ion beam irradiation," Nucl. Instrum. Methods Phys. Res., Sect. B **384**, 86–92 (2016).

[25]P. Mota-Santiago, F. Kremer, G. Rizza, C. Dufour, V. Khomenkov, C. Notthoff, A. Hadley, and P. Kluth, "Ion shaping of single-layer Au nanoparticles in amorphous silicon dioxide, in silicon nitride, and at their interface," Phys. Rev. Mater. **4**, 096002 (2020).

[26]P.-E. Mota-Santiago, A. Crespo-Sosa, J.-L. Jiménez-Hernández, H.-G. Silva-Pereyra, J.-A. Reyes-Esqueda, and A. Oliver, "Size characterisation of noble-metal nano-crystals formed in sapphire by ion irradiation and subsequent thermal annealing," Appl. Surf. Sci. **259**, 574–581 (2012).

[27]S. Korkos, V. Jantunen, K. Arstila, T. Sajavaara, A. Leino, K. Nordlund, and F. Djurabekova, "Nanorod orientation control by swift heavy ion irradiation," Appl. Phys. Lett. **120**, 171602 (2022).

[28]J. Bachmann, R. Zierold, Y. T. Chong, R. Hauert, C. Sturm, R. Schmidt-Grund, B. Rheinländer, M. Grundmann, U. Gösele, and K. Nielsch, "A practical, self-catalytic, atomic layer deposition of silicon dioxide," Angew. Chem. Int. Ed. **47**, 6177–6179 (2008).

[29]D. Hiller, R. Zierold, J. Bachmann, M. Alexe, Y. Yang, J. W. Gerlach, A. Stesmans, M. Jivanescu, U. Müller, J. Vogt, H. Hilmer, P. Löper, M. Künle, F. Munnik, K. Nielsch, and M. Zacharias, "Low temperature silicon dioxide by thermal atomic layer deposition: Investigation of material properties," J. Appl. Phys. **107**, 064314 (2010).

[30]M. Zarchi, S. Ahangarani, and M. Z. Sanjari, "Properties of silicon dioxide film deposited by PECVD at low temperature/pressure," Metall. Mater. Eng. **20**, 89–96 (2014).

[31]X. Chen, Y. Lu, L. Tang, Y. Wu, B. J. Cho, X. Xu, J. Dong, and W. Song, "Annealing and oxidation of silicon oxide films prepared by plasma-enhanced chemical vapor deposition," J. Appl. Phys. **97**, 014913 (2005).

[32]J. Fu, H. Shang, Z. Li, W. Wang, and D. Chen, "Thermal annealing effects on the stress stability in silicon dioxide films grown by plasma-enhanced chemical vapor deposition," Microsyst. Technol. **23**, 2753–2757 (2017).

[33] M. Laitinen, M. Rossi, J. Julin, and T. Sajavaara, "Time-of-flight–energy spectrometer for elemental depth profiling–Jyväskylä design," Nucl. Instrum. Methods Phys. Res., Sect. B **337**, 55–61 (2014).

[34] K. Arstila, J. Julin, M. I. Laitinen, J. Aalto, T. Konu, S. Kärkkäinen, S. Rahkonen, M. Raunio, J. Itkonen, J.-P. Santanen, T. Tuovinen, and T. Sajavaara, "Potku–new analysis software for heavy ion elastic recoil detection analysis," Nucl. Instrum. Methods Phys. Res., Sect. B **331**, 34–41 (2014).

[35] M. R. Amirzada, A. Tatzel, V. Viereck, and H. Hillmer, "Surface roughness analysis of SiO_2 for PECVD, PVD and IBD on different substrates," Appl. Nanosci. **6**, 215–222 (2016).

[36] M. Kobylko, P.-E. Coulon, A. Slablab, A. Fafin, J. Cardin, C. Dufour, A. Losquin, M. Kociak, I. Monnet, D. Mailly, X. Lafosse, C. Ulysse, E. Garcia-Caurel, and G. Rizza, "Localized plasmonic resonances of prolate nanoparticles in a symmetric environment: Experimental verification of the accuracy of numerical and analytical models," Phys. Rev. Appl. **9**, 064038 (2018).

[37] A. Krasheninnikov and K. Nordlund, "Ion and electron irradiation-induced effects in nanostructured materials," J. Appl. Phys. **107**, 3 (2010).

[38] K. Heinig, T. Müller, B. Schmidt, M. Strobel, and W. Möller, "Interfaces under ion irradiation: Growth and taming of nanostructures," Appl. Phys. A **77**, 17–25 (2003).

[39] P. Kluth, B. Johannessen, G. J. Foran, D. Cookson, S. Kluth, and M. C. Ridgway, "Disorder and cluster formation during ion irradiation of Au nanoparticles in SiO_2," Phys. Rev. B **74**, 014202 (2006).

[40] G. Rizza, H. Cheverry, T. Gacoin, A. Lamasson, and S. Henry, "Ion beam irradiation of embedded nanoparticles: Toward an *in situ* control of size and spatial distribution," J. Appl. Phys. **101**, 014321 (2007).

[41] O. Peña-Rodríguez, A. Prada, J. Olivares, A. Oliver, L. Rodríguez-Fernández, H. G. Silva-Pereyra, E. Bringa, J. M. Perlado, and A. Rivera, "Understanding the ion-induced elongation of silver nanoparticles embedded in silica," Sci. Rep. **7**, 1 (2017).

[42] P. Kluth, R. Giulian, D. Sprouster, C. Schnohr, A. Byrne, D. Cookson, and M. Ridgway, "Energy dependent saturation width of swift heavy ion shaped embedded Au nanoparticles," Appl. Phys. Lett. **94**, 113107 (2009).

PIII

ELONGATION AND PLASMONIC ACTIVITY OF EMBEDDED METAL NANOPARTICLES FOLLOWING HEAVY ION IRRADIATION

by

Spyridon Korkos, Kai Arstila, Kosti Tapio, Sami Kinnunen, J. Jussi Toppari & Timo Sajavaara

Elongation and plasmonic activity of embedded metal nanoparticles following heavy ion irradiation†

Spyridon Korkos, [ID] *[ab] Kai Arstila,[ab] Kosti Tapio,[b] Sami Kinnunen,[ab] J. Jussi Toppari [ID] [b] and Timo Sajavaara [ID] [ab]

Shape modification of embedded nanoparticles by swift heavy ion (SHI) irradiation is an effective way to produce nanostructures with controlled size, shape, and orientation. In this study, randomly oriented gold nanorods embedded in SiO_2 are shown to re-orient along the ion beam direction. The degree of orientation depends on the irradiation conditions and the nanorod's initial size. SHI irradiation was also applied to modify spherical metallic nanoparticles embedded in Al_2O_3. The results showed that they elongate due to the irradiation comparably to those embedded in SiO_2. Metallic nanostructures embedded in dielectric matrices can exhibit localized surface plasmon (LSP) modes. The elongated nanoparticles investigated by means of dark-field spectroscopy showed two discrete peaks which correspond to longitudinal and transverse modes.

1   Introduction

The optical properties of embedded metallic nanostructures in dielectric materials are of particular interest because they originate from the localized surface plasmon (LSP) modes.[1–7] These modes show a strong extinction peak at the localized surface plasmon resonance (LSPR) frequency. The LSPR peak arises from the collective oscillations of the conduction electrons confined within the volume of the nanoparticle. Moreover, at the resonance the electric field near the nanoparticle can be greatly enhanced due to the excess electric near-field created by the oscillating electrons of the plasmonic excitation. This near-field enhancement can lead to numerous applications, such as surface enhanced Raman spectroscopy,[8] fluorescent or emission enhancement,[2,9] photovoltaic and photocatalytic devices,[10] optical waveguides,[11] and nanolasers.[12] Since these phenomena depend mainly on the surrounding material and the material and shape of nanostructures, the nanofabrication of this metal-dielectric system is of the greatest interest.

The most challenging part is the fabrication of the nanostructures as the optical response can depend not only on their material, shape, and size but their orientation as well. Instead

of the standard nanofabrication techniques (colloidal chemistry, electron beam lithography or ion implantation), swift heavy ion (SHI) irradiation can modify the shape of embedded nanostructures (gold nanostructures embedded in SiO_2 is the most studied system) in order to produce perfectly aligned nanorods along the ion beam direction.[13–21] Especially, colloidal chemistry permits the synthesis of metallic nanoparticles of various shapes in liquid solutions, but with random orientations after the dispersion on a surface. In the case of electron beam lithography, the creation of well separated and aligned nanorods is time consuming for larger areas. During this process, known as ion beam shaping, the ion first forms a track in the host matrix leading to a decrease of density in the matrix (under densification). When the energy from the ions is transferred to the electrons of the metallic nanoparticle, the energy diffuses rapidly outward to the surface. As the energy reaches the metal/matrix boundary and is transferred to the electrons of the surrounding matrix, the temperature increases at the boundary due to the stronger electron–phonon coupling of the surrounding dielectric matrix. However, the surrounding matrix prevents the energy diffusion because of the lower thermal conductivity. Consequently, the electronic energy is transformed to heat and diffuses back toward the center of the nanoparticle resulting in full or partial melting.[17] Finally, the molten metal flows into the track leading in elongation after cooling and recrystallization.[19,22] This is not the only candidate mechanism as ion hammering effect has been proposed as well.[23–25] However, Amekura *et al.*[26] have shown that the latter mechanism is inconsistent with the experimental results.

[a]Accelerator Laboratory, Department of Physics, University of Jyväskylä, P. O. Box 35, FI-40014 Jyvaskyla, Finland. E-mail: spyridon.s.korkos@jyu.fi; kai.arstila@jyu.fi; sami.a.kinnunen@jyu.fi; timo.sajavaara@jyu.fi

[b]Nanoscience Center and Department of Physics, University of Jyväskylä, P. O. Box 35, FI-40014 Jyvaskyla, Finland. E-mail: kosti.t.o.tapio@jyu.fi; j.jussi.toppari@jyu.fi

The anisotropic nanorod shape offers two discrete LSPR peaks corresponding to longitudinal and transverse oscillation of the electrons. A suitable way to detect these two modes in a single nanoparticle is by applying dark-field optical microscopic spectroscopy. Dark-field spectroscopy is a well-established scattering technique for measuring the LSPR spectrum of single nanoparticles.[27–29] The use of a broadband non-coherent low intensity light source does not cause deformation of the particles during imaging, which could lead to different plasmonic properties. However, the limitation on detection arise from the fact that scattering cross-section depends mainly on nanoparticle radius[30] and as a result, nanoparticles with diameters less than 30 nm are difficult to detect and hence cannot be separated from their surrounding environment even with the very sensitive setup utilized in this work.[31]

Earlier studies have shown that the elongation of the nanoparticles along the ion beam direction strongly depends on the initial size of the nanoparticles and the applied fluence.[15,17,22,32] However, this dependence on the initial size has not been extended for nanoparticles embedded to other material matrices apart from SiO_2 in contrast to the great variety of metallic species used.[4,14–17,21,33,34] Moreover, there is a shortage of studies regarding the nanoparticles shape other than spherical.

In a previous study,[35] we showed that SHI irradiated gold nanorods, which are embedded in SiO_2 and laid in a plane with a 45° angle to the ion beam direction, re-oriented to align with the beam. However, the impact of different fluences on the nanorods was not investigated experimentally. In addition, Atomic Layer Deposition (ALD) was used to deposit SiO_2 which offered greater elongation in nanoparticles embedded inside that than in Plasma-Enhanced Chemical Vapor Deposition (PECVD) SiO_2.[32] The ALD can be used easily for the deposition of other films as well, such as amorphous Al_2O_3, TiO_2, ZnO, *etc.* These have not been investigated in connection with SHI irradiation of embedded nanoparticles.

In this study, Au and Ag nanoparticles of various size and shape were embedded in amorphous SiO_2 and amorphous Al_2O_3 deposited on top of Si_3N_4 TEM windows grid. The samples were irradiated by energetic ions using various fluences. Apart from chemically synthesized spherical nanoparticles, focused ion beam (FIB) lithography was used as well to create nanorods prior to irradiation. Within this technique, the desired nanostructure shape, size, and orientation on the surface of a film can be created using the capabilities of a Helium Ion Microscope (HIM) equipped with a Ne^+ beam. By this way, the modification of nanorods inside SiO_2 and spherical nanoparticles inside Al_2O_3 following heavy ion irradiation was investigated in detail depending on their initial size and fluence. The nanoplasmonic activity of irradiated nanoparticles was studied by applying dark-field spectroscopy to collect the spectra from individual nanoparticles. The obtained new information about the elongation process can be used to design and conduct new experiments and devices utilizing this method.

2 Experimental section

2.1 Sample preparation

Two types of samples were fabricated depending on the different matrix material and the shape of nanoparticles embedded inside them. Both were created on top of a TEM grid with nine windows of 20 nm thick Si_3N_4.

2.1.1 Nanorods in SiO_2. During the fabrication of the first type of the samples, 50 nm of ALD SiO_2 were initially deposited. Then, Au nanorods made by HIM nanolithography were fabricated on top. In order to embed the nanorods inside SiO_2, another 50 nm of SiO_2 was deposited by ALD.[32]

The fabrication of Au nanorods was made as following: a thin layer of gold (15–20 nm thickness) was first deposited using Ultra High Vacuum (UHV) evaporator. The next step was the milling of a selected area by 30 keV Ne^+ beam in HIM. The Ne^+ beam was used to mill away the gold layer from a rectangular area leaving to the center a nanorod of desired size and orientation as shown in Fig. 1. One of the three dimensions of the nanorods made by nanolithography was limited to 15–20 nm due to the original Au film thickness.

Additionally, samples with chemically synthesized gold nanorods embedded in SiO_2 deposited by Plasma-Enhanced Chemical Vapor Deposition (PECVD) were created as described in ref. 35. On top of a TEM grid, 50 nm of PECVD SiO_2 was firstly deposited and then chemically synthesized gold nanorods were dispersed on top. Finally, another 50 nm of PECVD SiO_2 was deposited in order to encapsulate the nanorods inside SiO_2.

2.1.2 Spherical nanoparticles in Al_2O_3. The second type of the samples consisted of 50 nm of Al_2O_3 deposited by ALD on which chemically synthesized spherical Au (5–60 nm diameter) and Ag (10–25 nm diameter) nanoparticles were dispersed on top. The embedding of the nanoparticles was achieved by depositing another 50 nm of Al_2O_3.

2.1.3 Thin film deposition and characterization. A Beneq TFS 200 cross flow reactor was used to deposit the thin films by ALD working at 100–200 Pa base pressure during the deposition. The depositions temperature was 200 °C. Nitrogen from Inmatec PN 1150 nitrogen generator (99.999% purity) was used as a carrier gas as well as for purging between the precursor pulses. For the deposition of SiO_2,[32,36] (3-aminopropyl)-
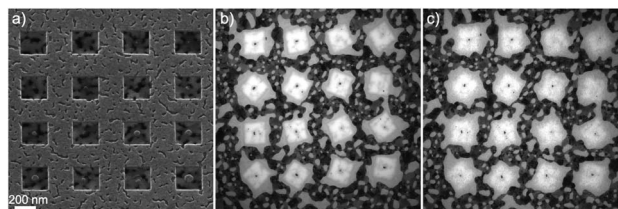

Fig. 1 (a) HIM image after the patterning of nanostructures with a Ne^+ beam, each rectangular area has slightly different processing parameters, (b) TEM image of patterned nanostructures different from (a) after embedding them in SiO_2 prior to irradiation, and (c) TEM image of the same nanostructures as in (b) after the irradiation. The scale is the same in all the three images.

triethoxysilane (APTES) (Sigma Aldrich, 99%), deionized water, and O_3 were used as precursors. The growth of 50 nm SiO_2 corresponded to 1250 cycles (36 h). For the deposition of Al_2O_3, trimethylaluminium (TMA) (Strem Chemicals, >98%) and deionised water were used as precursors.[37,38] In order to deposit 50 nm Al_2O_3, 460 cycles (50 min) were applied.

For the deposition of SiO_2 at 200 °C by PECVD, a Plasma-lab80Plus (Oxford Instruments) machine was utilized using silane (SiH_4 in Ar) and nitrous oxide (N_2O) as precursors.[32,39] The working pressure during the deposition was 133 Pa and the chamber was purged with N_2 for 2 min before the deposition. The growth rate of the deposited film was approximately 50 nm min^{-1}.

The properties of the grown films were investigated from films grown on Si substrate. The thicknesses and the refractive indexes of the deposited films were measured by spectroscopic ellipsometry (SOPRA GES 5E) equipped with a Xe lamp (75 W). The measured total thickness of the SiO_2 films was 107.5 ± 0.5 nm, while Al_2O_3 film had 100.4 ± 0.6 nm thickness. Their refractive indexes were measured to be 1.52 and 1.66, respectively. Detailed composition analysis performed by Time-of-Flight Elastic Recoil Detection Analysis (ToF-ERDA)[40] for films deposited using identical process is found in ref. 32 for SiO_2 and ref. 38 for Al_2O_3. ALD-SiO_2 and PECVD-SiO_2 films are nearly stoichiometric with O/Si elemental ratios 2.07 ± 0.02 and 2.06 ± 0.02, respectively. Except silicon and oxygen, the film contain a significant amount of hydrogen (6.5 and 7.6 at%, respectively) as well as negligible amounts of carbon and nitrogen (less than 1 at%). ALD-Al_2O_3 film is almost stoichiometric with elemental ratio O/Al $= 1.56 \pm 0.03$ and the contained impurities are hydrogen (2.8 at%) and carbon (less than 0.5 at%).

2.2 Sample irradiation and imaging

The samples fabricated on TEM grid were irradiated with 50 MeV $^{127}I^{9+}$ ions at the TAMIA 5 MV tandem accelerator at Helsinki accelerator laboratory (University of Helsinki) as described in ref. 32. The angle of incidence was 45° and several fluences from 5×10^{13} ions per cm^2 to 2×10^{14} ions per cm^2 were applied at room temperature. Since the samples had such a thickness allowing the TEM imaging (120 nm totally), they were imaged with a JEOL-JEM 1400 TEM operated at 120 kV before and after the irradiation in order to track changes in the same nanoparticles. The shown TEM images prior to irradiation were taken from the top without tilting the TEM stage. However, the TEM images of the same nanoparticles after the irradiation were taken with the electron beam direction perpendicular to the ion beam direction in order to acquire the full information from the nanoparticles.

2.3 Optical characterization after the irradiation

The optical characterization of the samples after the irradiation was made by dark-field optical microscopy.[41] A brief description of the polarization dependent dark-field measurements is provided here (see ESI† for more details). An Olympus BX51TRF-microscope was used with Olympus 100 W halogen lamp. In order to investigate the plasmonic activity of the
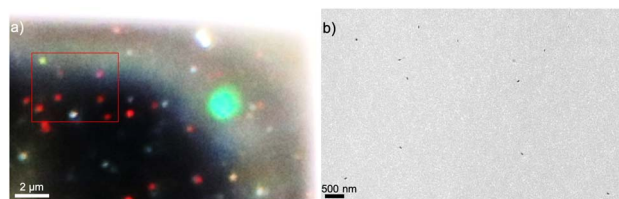

Fig. 2 (a)A dark-field optical image from a sample containing nanostructures and (b) TEM image from the same sample containing the nanostructures located at the red rectangle in dark-field optical image. The bigger green circle denotes the fiber position and aperture size.

embedded nanostructures to determine LSPR peaks, the scattering spectra were measured at different polarization angles using an Olympus U-AN360-3 analyzer with Thorlabs linear polarizer (LPVISE200-A 2). The analyzer in combination with the polarizer was used to calibrate the polarization angle of the analyzer in respect to the sample surface. The scattered light from each individual nanostructure was collected by an optical fiber (core size 300 µm) placed to the image plane of the selected area. The spectra were recorded by a spectrograph (Princeton Instruments SP2150 (Acton)) equipped with a charge-coupled device (CCD) camera (Andor iVac DR-324B-FI), which was controlled using Andor Solis (version 4.18) software. Fig. 2 shows the same area with nanoparticles imaged both by TEM and dark-field optical microscopy.

The Finite Difference Time Domain (FDTD) simulations of the embedded and elongated nanoparticles were done using FDTD method in Ansys Lumerical software (FDTD, 2021 version 8.26.2834).[42] During the simulations, we used two models to simulate the plasmonic scattering of the embbeded nanoparticle. Initially, we considered a model, where nanoparticles are surrounded by 100 nm thick medium (silicon dioxide or aluminum oxide) on top of a 20 nm thick silicon nitride window. There is an oil layer on top of the medium and air under the silicon nitride window. The incident light was injected from the oil side and characterized using scattering monitor. Polarization angles along the primary axis (transverse and longitudinal axis) were considered and the refractive indexes of 1.52 and 1.66 were used for SiO_2 and Al_2O_3, respectively. Additionally, a simplified, infinite medium model was tested, where the particles were placed in an infinite medium and the refractive index of the medium was altered to match the measured and simulated LSPR peaks (see Fig. S2 and S3 in the ESI†). In this case, the refractive indexes of 1.38 and 1.55 for SiO_2 and Al_2O_3 matched the two data.

3 Results and discussion

3.1 Irradiated Au nanorods embedded in SiO_2

Three fluences were used for the irradiation of the fabricated nanorods embedded in ALD-SiO_2. After 5×10^{13} ions per cm^2 fluence, the shape changes were observed to depend on the size of the nanorods. Fig. 3 and 4 present nanorods of different sizes and orientations, before and after the irradiation. The nanorods in Fig. 3 were reshaped and elongated along the ion beam
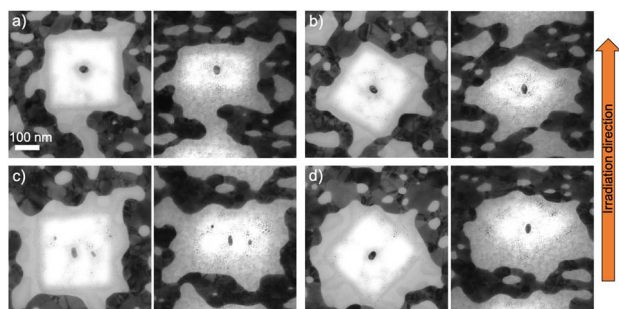
Fig. 3 TEM images of fabricated nanorods with different orientations embedded in 100 nm ALD-SiO$_2$ and irradiated with 50 MeV ^{127}I at 5 × 10^{13} ions per cm^2 before (left) and after (right) the irradiation. The TEM images prior to irradiation were taken from the top without tilting the TEM stage, while after the irradiation they were taken with the electron beam direction perpendicular to the ion beam direction. (a) Length = 39.2 nm and diameter = 29.5 nm, (b) length = 36.7 nm and diameter = 21.3 nm, (c) length = 38.6 nm and diameter = 20.9 nm, and (d) length = 36.4 nm and diameter = 26.5 nm. These nanorods re-oriented along the ion beam direction after the irradiation.

direction, while Fig. 4 presents nanorods, which were not elongated along the beam, but only slightly reshaped. In Fig. 4a and b, the nanorods have already started shrinking in the dimension perpendicular to the ion beam direction and elongating along the ion beam direction, but the applied fluence was not high enough to fully elongate them. Instead they turned to spheroids. The same effect can be observed as well in Fig. 4c in which the nanorod has started to incrementally reshape before its transformation to spheroid. In Fig. 4d, there is no change in the shape of this bigger nanorod comparing to others, but it is reduced in size due to the ion beam irradiation.

After 10^{14} ions per cm^2 fluence, the same reshaping effect occurred, *i.e.* nanorods with different orientation aligned along the ion beam direction (Fig. 5). The smallest nanorods elongate more than lower fluence, while bigger nanorods of the similar size as in Fig. 4c and d managed to also elongate along the ion beam direction (Fig. 5e). However, slightly bigger nanorod in Fig. 5f does not elongate along the ion beam direction.
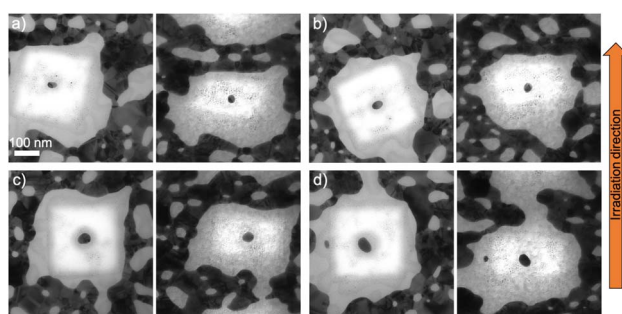

Fig. 4 TEM images of fabricated nanorods with different orientations embedded in 100 nm ALD-SiO$_2$ and irradiated with 50 MeV ^{127}I at 5 × 10^{13} ions per cm^2 before (left) and after (right) the irradiation. (a) Length = 35.9 nm and diameter = 24.0 nm, (b) length = 42.1 nm and diameter = 29.9 nm, (c) length = 51.9 nm and diameter = 37.1 nm, and (d) length = 58.2 nm and diameter = 36.0 nm. These nanorods did not manage to re-orient along the ion beam direction.
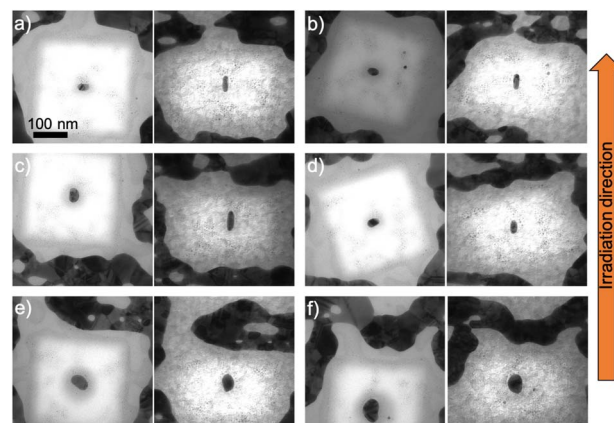

Fig. 5 TEM images of fabricated nanorods with different orientations embedded in 100 nm ALD-SiO$_2$ and irradiated with 50 MeV ^{127}I at 10^{14} ions per cm^2 before (left) and after (right) the irradiation. (a) Length = 34.0 nm and diameter = 19.9 nm, (b) length = 32.0 nm and diameter = 22.3 nm, (c) length = 42.6 nm and diameter = 23.4 nm and (d) length = 34.0 nm and diameter = 19.9 nm, (e) length = 50.4 nm and diameter = 31.2 nm, and (f) length = 70.4 nm and diameter = 42.3 nm.

Chemically synthesized nanorods of similar size as in Fig. 5f and embedded in PECVD SiO$_2$ were irradiated at 10^{14} ions per cm^2 fluence as well. Some nanorods still cannot elongate (Fig. 6a), but the formation of random protrusions/spikes on several nanorods was observed as well (Fig. 6b and c).

After the highest applied fluence (2 × 10^{14} ions per cm^2), the smallest nanorods elongated along the ion beam direction (Fig. 7a–c) but not more than after lower fluences. The high irradiation fluence prevents them from greater elongation and forces them to shrink. This happens because of the size of a nanoparticle which is a basic parameter whether it will keep growing or starting disintegrate after significant ion fluence. The fact that the third dimension of the nanorod is always originally close to 15 nm can lead to the disintegration since nanoparticles below that critical size can start to disintegrate as shown in ref. 32. A bigger nanorod of the similar size as in Fig. 4c and d elongates along the ion beam direction in this highest fluence (Fig. 7d).

The modification of the nanorods can be explained[35] as small incremental shape changes caused by highly energetic ions resulting in growth in the beam direction and loss of length in the other directions. The first ion impacts form protrusions onto the nanorods (as shown in Fig. 4c) and when more impacts take place, they transform the nanorod to a spheroid (as shown in Fig. 4a and b) and then to a nanorod
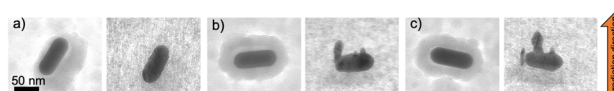

Fig. 6 TEM images of chemically synthesized nanorods embedded in 100 nm PECVD SiO$_2$ and irradiated with 50 MeV ^{127}I at 10^{14} ions per cm^2 before (left) and after (right) the irradiation. (a) Length = 86.0 nm and diameter = 35.0 nm, (b) length = 81.5 nm and diameter = 32.4 nm, and (c) length = 82.2 nm and diameter = 33.0 nm.
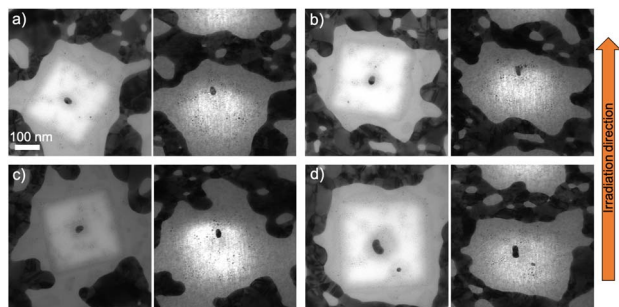
Fig. 7 TEM images of fabricated nanorods with different orientations embedded in 100 nm ALD–SiO$_2$ and irradiated with 50 MeV ^{127}I at 2 × 10^{14} ions per cm^2 before (left) and after (right) the irradiation. (a) Length = 33.2 nm and diameter = 22.6 nm, (b) length = 37.1 nm and diameter = 25.1 nm, (c) length = 35.0 nm and diameter = 24.4 nm, and (d) length = 62.8 nm and diameter = 29.2 nm before (left) and after (right) irradiation.

Fig. 9 TEM images of elongated Au nanoparticles sandwiched between two 50 nm ALD–Al$_2$O$_3$ layers and irradiated with 50 MeV ^{127}I at 2 × 10^{14} ions per cm^2 before (left) and after (right) the irradiation.

aligned with the beam (as shown in Fig. 3). However, even if the theoretical studies have shown that large nanorods cannot be modified because of the interface effects,[43] the formation of protrusions/spikes on them takes place along the ion beam direction at high enough fluences (≥10^{14} ions per cm^2).

3.2 Irradiated nanoparticles embedded in ALD-Al$_2$O$_3$

Spherical Au and Ag nanoparticles embedded in ALD-Al$_2$O$_3$ were irradiated the same way as the SiO$_2$ samples. In Fig. 8 and 9, the elongation of spherical Au nanoparticles is shown for 5 × 10^{13} and 2 × 10^{14} ions per cm^2 fluences, respectively. As the fluence increases, the elongation ratio increases as well (Al$_2$O$_3$ curves in Fig. 10). For both fluences, the maximum elongation ratio is observed for nanoparticles of 25–30 nm diameter.

Before the irradiation, the nanoparticles (spherical and nanorods) are surrounded by a dark spot which indicates an area with a higher density.[32] However, after the irradiation, these spots have been disappeared resulting in a more homogeneous matrix.

Comparing these results with ALD-SiO$_2$ (Fig. 10) after 5 × 10^{13} ions per cm^2 fluence,[32] Al$_2$O$_3$ samples exhibit slightly higher elongation ratio than SiO$_2$ samples only for initial size
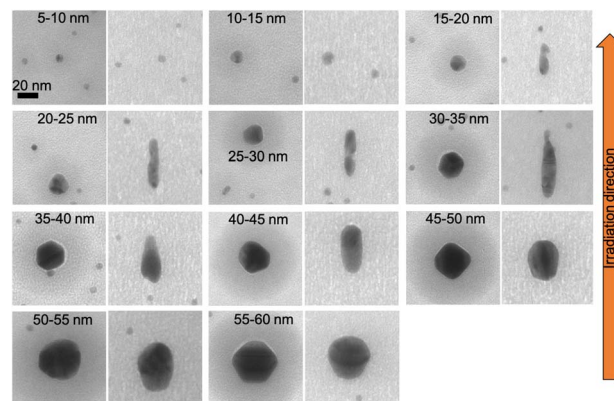
from 15 to 30 nm. At higher fluences, there cannot be absolute comparison since SiO$_2$ samples are irradiated with a double fluence (5 × 10^{14} ions per cm^2). With this difference in the fluence, for nanoparticles with initial size from 15 to 25 nm, the elongation is almost doubled if embedded in SiO$_2$ compared to Al$_2$O$_3$. For the rest of the nanoparticles, the difference in ratio is smaller.

These results show that Au nanoparticles embedded in Al$_2$O$_3$ can sufficiently elongate with comparable ratio as in SiO$_2$. According to Mota-Santiago et al.,[21] the electron–phonon coupling and the thermal conductivity of the host matrix cause the different nanoparticles elongation between two host materials (SiO$_2$ and Si$_3$N$_4$ in that case). On the one hand, the higher electron–phonon coupling of SiO$_2$ ($g_{SiO_2} = 1.25 \times 10^{19}$ W m^{-3} K^{-1}, $g_{Si_3N_4} = 0.52 \times 10^{19}$ W m^{-3} K^{-1}) implies greater energy transfer from the electronic subsystem to the lattice. On the other hand, the smaller thermal conductivity of SiO$_2$ ($k_{SiO_2} = 3$ W$_{Al_2O_3}$ m^{-1} K^{-1}, $k_{Si_3N_4} = 11$ W m^{-1} K^{-1}) leads to slower cooling resulting in more material flow into the ion track. Consequently, Au nanoparticles elongate more in SiO$_2$ than in Si$_3$N$_4$.
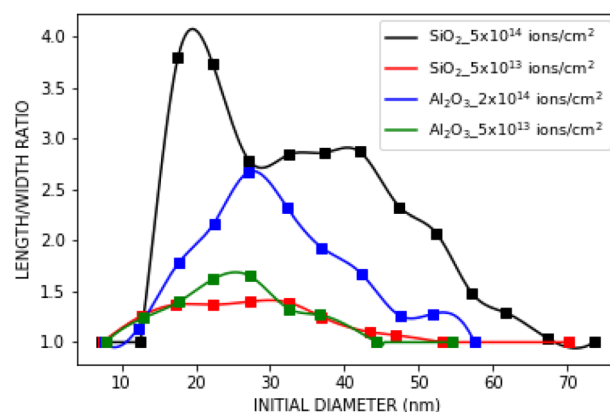

Fig. 8 TEM images of elongated Au nanoparticles sandwiched between two 50 nm ALD–Al$_2$O$_3$ layers and irradiated with 50 MeV ^{127}I at 5 × 10^{13} ions per cm^2 before (left) and after (right) the irradiation.

Fig. 10 Comparison of the elongation ratio vs. initial diameter for the nanoparticles embedded in ALD-SiO$_2$ (ref. 32) and ALD-Al$_2$O$_3$. The uncertainties are left out from the image for clarity.
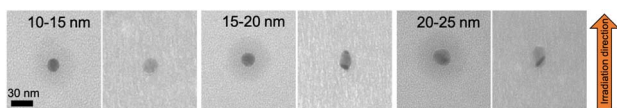
Fig. 11 TEM images of elongated Ag nanoparticles sandwiched between two 50 nm ALD-Al$_2$O$_3$ layers irradiated with 50 MeV ^{127}I at 2 × 10^{14} ions per cm^2 before (left) and after (right) the irradiation.

In our case, Al$_2$O$_3$ has lower electron–phonon coupling ($g = 0.48$ × 10^{19} W m^{-2} K^{-1}) and higher thermal conductivity ($k_{\mathrm{Al_2O_3}} =$ 30 W m^{-1} K^{-1}) than SiO$_2$. Nevertheless, there is no much difference in nanoparticles elongation ratio between them.

Furthermore, Ag nanoparticles exhibited smaller elongation ratio than Au nanoparticles. As shown in Fig. 11, the Ag nanoparticles irradiated at 2 × 10^{14} ions per cm^2 fluence achieve in average only half the elongation ratio compared to the Au nanoparticles at the same fluence. This is consistent with previous experiments in which Au nanoparticles embedded in SiO$_2$ elongate more than Ag nanoparticles.[15,17]

3.3 Optical characterization of irradiated nanoparticles embedded in SiO$_2$ and Al$_2$O$_3$

The determination of localized surface plasmon resonance (LSPR) peaks of the embedded nanostructures after the irradiation was achieved by dark-field optical microscopic spectroscopy which allowed to locate and measure the scattering spectra of individual nanostructures.[41,44] Some limitations appeared during the experiments preventing the collection of spectra for each size of nanostructures. The distance between two nanostructures as well as the size of the fiber spot (approximately 1–2 μm diameter) made the distinction between the nanoparticles many times difficult. Moreover, only elongated nanoparticles with width more than 30 nm could be imaged.[31,45,46] The reason is that the absorption is dominating for sizes less than 30 nm resulting in weak scattering, which even in an ideal case could be lost in the background scattering signal.[31] In our case, the background scattering is increased further due to transparent, uneven substrate with several interfaces that scatter light. In addition, the fact that the nanoparticles are embedded inside a material and not lying on a surface worsens the resolution.

The spectra with the corresponding nanostructures are shown in Fig. 12. To determine the origin of the LSPR peaks, we ran FDTD simulations using Ansys Lumerical. The simulated spectra were extracted using the simplified model to reduce the simulation time. The spherical nanoparticle in Fig. 12c exhibits one (dipolar) plasmon mode, while the elongated nanoparticles in Fig. 12a, b and d exhibit two plasmon modes. The main peak corresponds to the longitudinal mode of the elongated nanostructure while the second, smaller peak corresponds to the transverse mode. The splits between the two LSPR modes in the case of Al$_2$O$_3$ are 71 nm and 46 nm in the Fig. 12a and b because of the different widths of the nanoparticles. For SiO$_2$ the split is 48 nm in Fig. 12d. The transverse LSP mode in experimental spectrum of the elongated nanoparticle in Fig. 12d is very weak because the width of the nanoparticle reaches the limit of the
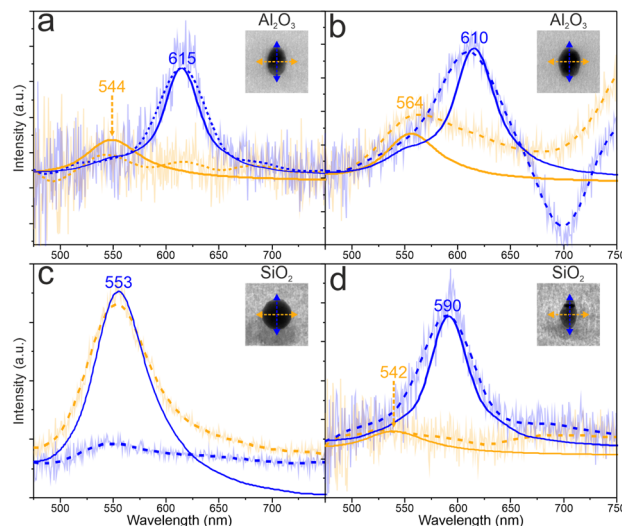

Fig. 12 Dark-field scattering spectra of two elongated nanoparticles embedded in Al$_2$O$_3$ (a and b), one spherical nanoparticle embedded in SiO$_2$ (c) and one elongated nanoparticle embedded in SiO$_2$ (d). The solid line is the result from the FDTD simulation and the dashed line the averaged measurement, with original data shown as a lighter line. The blue and the yellow spectra correspond to the longitudinal and transverse modes, respectively. The inset TEM images show the measured particles with LSP polarizations marked. The size of the TEM images is 110 nm × 110 nm. The lengths and the widths of the particles in (a) and (b) are 51.3 nm and 32.5 nm and 51.9 nm and 39.9 nm, respectively. The diameter of the particle in (c) is 53.6 nm and the length and the width of the particle in (d) are 52.5 nm and 31.9 nm, respectively.

size detection.[47] The measured main LSPR peak is more red shifted in the case of Al$_2$O$_3$ compared to SiO$_2$ due to higher refractive index of the surrounding medium.

The LSPR peaks of embedded nanoparticles inside SiO$_2$, which have been irradiated with SHI, have already been investigated with the electron energy loss spectroscopy in scanning transmission electron microscope (STEM EELS).[4,7] According to Kobylko et al.,[7] the LSPR peak of an unirradiated spherical Au nanoparticle of around 22 nm diameter is located at 558 nm. Comparing this with our results, there is a slight shift of the LSPR peak to lower wavelength. In our case, the spherical nanoparticle is bigger and measured after the irradiation, which has caused structural changes in the surrounding material. Peña-Rodríguez et al.[48] have demonstrated that the irradiation causes density changes in the surrounding material resulting to the change of the refractive index, which affects the LSPR peaks. In addition, an elongated nanoparticle of 61.6 nm length and 31.4 nm (aspect ratio 1.94) width has a longitudinal LSPR peak at 652 nm and a transverse peak at 532 nm. In our measurements, the elongated nanoparticle has length 52.5 nm and width 31.4 nm (aspect ratio 1.64). The transverse peak is located at 542 nm which differs slightly from Kobylko's result because the width in both cases is almost the same and there is a difference in irradiation conditions. On the other hand the longitudinal peak is located at 590 nm which differs significantly from Kobylko's because there is 9.1 nm difference in length.

4 Conclusions

In this work, we investigated the impact of SHI irradiation on embedded nanorods and showed that the irradiation modifies them in different ways depending on their initial size and applied fluence. As a result, the smallest ones with length less than 40 nm and diameter less than 30 nm are reshaped to nanorods aligned with the ion beam direction after any fluence applied. Nanorods with length between 40 and 50 nm and diameter between 30 and 40 nm irradiated with the lowest fluence only manage to turn to spheroids, while after higher fluences, they are reshaped along the ion beam direction. However, the largest ones with length between 70 and 86 nm and diameter between 30 and 45 nm either retain their shape or random protrusions/spikes are formed on them. Additionally, we studied the elongation of spherical gold and silver nanoparticles embedded in Al_2O_3. The results showed that gold nanoparticles can elongate similarly as in SiO_2 even if they have different electron–phonon coupling and thermal conductivity. On the other hand, the silver nanoparticles elongate less than gold ones. Apart from these, the investigation of their nanoplasmonic activity showed that the elongated nanoparticles both in SiO_2 and Al_2O_3 exhibit two discrete LSP modes (longitudinal and transverse) which make them potential candidates for photonics applications.

Author contributions

Spyridon Korkos conceptualized the project, performed the experiments, analyzed and visualized the data, and wrote the original draft. Kai Arstila conceptualized the project and performed the experiments. Kosti Tapio performed the experiments, analyzed and visualized the data, and wrote the original draft. Sami Kinnunen performed the experiments. J. Jussi Toppari reviewed and edited the manuscript. Timo Sajavaara reviewed and edited the manuscript.

Conflicts of interest

There are no conflicts to declare.

Acknowledgements

References

1 S. A. Maier et al., *Plasmonics: Fundamentals and Applications*, Springer, 2007, vol. 1.

2 P. Bharadwaj, B. Deutsch and L. Novotny, *Adv. Opt. Photonics*, 2009, **1**, 438–483.

3 O. Sánchez-Dena, P. Mota-Santiago, L. Tamayo-Rivera, E. García-Ramírez, A. Crespo-Sosa, A. Oliver and J.-A. Reyes-Esqueda, *Opt. Mater. Express*, 2014, **4**, 92–100.

4 A. Slablab, T. J. Isotalo, J. Mäkitalo, L. Turquet, P.-E. Coulon, T. Niemi, C. Ulysse, M. Kociak, D. Mailly, G. Rizza, et al., *Sci. Rep.*, 2016, **6**, 37469.

5 O. Peña-Rodríguez, A. Prada, J. Olivares, A. Oliver, L. Rodríguez-Fernández, H. G. Silva-Pereyra, E. Bringa, J. M. Perlado and A. Rivera, *Sci. Rep.*, 2017, **7**, 922.

6 S. Wolf, J. Rensberg, A. Johannes, R. Thomae, F. Smit, R. Neveling, M. Moodley, T. Bierschenk, M. Rodriguez, B. Afra, et al., *Nanotechnology*, 2016, **27**, 145202.

7 M. Kobylko, P.-E. Coulon, A. Slablab, A. Fafin, J. Cardin, C. Dufour, A. Losquin, M. Kociak, I. Monnet, D. Mailly, et al., *Phys. Rev. Appl.*, 2018, **9**, 064038.

8 S. Schlücker, *Angew. Chem., Int. Ed.*, 2014, **53**, 4756–4795.

9 F. Tam, G. P. Goodrich, B. R. Johnson and N. J. Halas, *Nano Lett.*, 2007, **7**, 496–501.

10 C. Clavero, *Nat. Photonics*, 2014, **8**, 95.

11 R. Li, C. Pang, Z. Li and F. Chen, *Adv. Opt. Mater.*, 2020, **8**, 1902087.

12 C. Pang, R. Li, Z. Li, N. Dong, C. Cheng, W. Nie, R. Böttger, S. Zhou, J. Wang and F. Chen, *Adv. Opt. Mater.*, 2018, **6**, 1800357.

13 C. d'Orléans, J. Stoquert, C. Estournes, C. Cerruti, J. Grob, J. Guille, F. Haas, D. Muller and M. Richard-Plouet, *Phys. Rev. B: Condens. Matter Mater. Phys.*, 2003, **67**, 220101.

14 Y. Mishra, F. Singh, D. Avasthi, J. Pivin, D. Malinovska and E. Pippel, *Appl. Phys. Lett.*, 2007, **91**, 063103.

15 K. Awazu, X. Wang, M. Fujimaki, J. Tominaga, H. Aiba, Y. Ohki and T. Komatsubara, *Phys. Rev. B: Condens. Matter Mater. Phys.*, 2008, **78**, 054102.

16 R. Giulian, P. Kluth, L. Araujo, D. Sprouster, A. Byrne, D. Cookson and M. C. Ridgway, *Phys. Rev. B: Condens. Matter Mater. Phys.*, 2008, **78**, 125413.

17 G. Rizza, P. Coulon, V. Khomenkov, C. Dufour, I. Monnet, M. Toulemonde, S. Perruchas, T. Gacoin, D. Mailly, X. Lafosse, et al., *Phys. Rev. B: Condens. Matter Mater. Phys.*, 2012, **86**, 035450.

18 P.-E. Mota-Santiago, A. Crespo-Sosa, J.-L. Jiménez-Hernández, H.-G. Silva-Pereyra, J.-A. Reyes-Esqueda and A. Oliver, *Appl. Surf. Sci.*, 2012, **259**, 574–581.

19 A. A. Leino, O. Pakarinen, F. Djurabekova, K. Nordlund, P. Kluth and M. C. Ridgway, *Mater. Res. Lett.*, 2014, **2**, 37–42.

20 H. Amekura, K. Narumi, A. Chiba, Y. Hirano, K. Yamada, D. Tsuya, S. Yamamoto, N. Okubo, N. Ishikawa and Y. Saitoh, *Sci. Rep.*, 2019, **9**, 1–10.

21 P. Mota-Santiago, F. Kremer, G. Rizza, C. Dufour, V. Khomenkov, C. Notthoff, A. Hadley and P. Kluth, *Phys. Rev. Mater.*, 2020, **4**, 096002.

22 T. Vu, C. Dufour, V. Khomenkov, A. Leino, F. Djurabekova, K. Nordlund, P.-E. Coulon, G. Rizza and M. Hayoun, *Nucl. Instrum. Methods Phys. Res., Sect. B*, 2019, **451**, 42–48.

23 S. Roorda, T. van Dillen, A. Polman, C. Graf, A. van Blaaderen and B. J. Kooi, *Adv. Mater.*, 2004, **16**, 235–237.

24 S. Klaumünzer, *Nucl. Instrum. Methods Phys. Res., Sect. B*, 2006, **244**, 1–7.

25 C. H. Kerboua, J.-M. Lamarre, M. Chicoine, L. Martinu and S. Roorda, *Thin Solid Films*, 2013, **527**, 186–192.

26 H. Amekura, P. Kluth, P. Mota-Santiago, I. Sahlberg, V. Jantunen, A. Leino, H. Vazquez, K. Nordlund and F. Djurabekova, *Nucl. Instrum. Methods Phys. Res., Sect. B*, 2020, **475**, 44–48.

27 M. Hu, C. Novo, A. Funston, H. Wang, H. Staleva, S. Zou, P. Mulvaney, Y. Xia and G. V. Hartland, *J. Mater. Chem.*, 2008, **18**, 1949–1960.

28 Y. Song, P. D. Nallathamby, T. Huang, H. E. Elsayed-Ali and X.-H. N. Xu, *J. Phys. Chem. C*, 2010, **114**, 74–81.

29 L. Guo, X. Zhou and D.-H. Kim, *Biosens. Bioelectron.*, 2011, **26**, 2246–2251.

30 H. C. Hulst and H. C. van de Hulst, *Light scattering by small particles*, Courier Corporation, 1981.

31 P. Zijlstra and M. Orrit, *Rep. Prog. Phys.*, 2011, **74**, 106401.

32 S. Korkos, K. Mizohata, S. Kinnunen, T. Sajavaara and K. Arstila, *J. Appl. Phys.*, 2022, **132**, 045901.

33 H. Amekura, N. Ishikawa, N. Okubo, M. C. Ridgway, R. Giulian, K. Mitsuishi, Y. Nakayama, C. Buchal, S. Mantl and N. Kishimoto, *Phys. Rev. B: Condens. Matter Mater. Phys.*, 2011, **83**, 205401.

34 E. Dawi, T. Ommar, R. Ackermann and A. Karar, *Int. J. Smart Nano Mater.*, 2020, **11**, 147–158.

35 S. Korkos, V. Jantunen, K. Arstila, T. Sajavaara, A. Leino, K. Nordlund and F. Djurabekova, *Appl. Phys. Lett.*, 2022, **120**, 171602.

36 J. Bachmann, R. Zierold, Y. T. Chong, R. Hauert, C. Sturm, R. Schmidt-Grund, B. Rheinländer, M. Grundmann, U. Gösele and K. Nielsch, *Angew. Chem., Int. Ed.*, 2008, **47**, 6177–6179.

37 E. Lakomaa, A. Root and T. Suntola, *Appl. Surf. Sci.*, 1996, **107**, 107–115.

38 S. Kinnunen, K. Arstila and T. Sajavaara, *Appl. Surf. Sci.*, 2021, **546**, 148909.

39 M. Zarchi, S. Ahangarani and M. Z. Sanjari, *Metall. Mater. Eng.*, 2014, **20**, 89–96.

40 M. Laitinen, M. Rossi, J. Julin and T. Sajavaara, *Nucl. Instrum. Methods Phys. Res., Sect. B*, 2014, **337**, 55–61.

41 B. Shen, V. Linko, K. Tapio, S. Pikker, T. Lemma, A. Gopinath, K. V. Gothelf, M. A. Kostiainen and J. J. Toppari, *Sci. Adv.*, 2018, **4**, eaap8978.

42 Lumerical Inc, 2021.

43 V. Jantunen, A. Leino, M. Veske, A. Kyritsakis, H. V. Muiños, K. Nordlund and F. Djurabekova, *J. Phys. D: Appl. Phys.*, 2022, **55**, 275301.

44 K. Tapio, S. Dongkai, S. Auer, J. Tuppurainen, M. Ahlskog, V. Hytönen and J. Toppari, *Nanoscale*, 2018, **10**, 19297–19309.

45 L. J. Anderson, K. M. Mayer, R. D. Fraleigh, Y. Yang, S. Lee and J. H. Hafner, *J. Phys. Chem. C*, 2010, **114**, 11127–11132.

46 B. C. Rostro-Kohanloo, L. R. Bickford, C. M. Payne, E. S. Day, L. J. Anderson, M. Zhong, S. Lee, K. M. Mayer, T. Zal, L. Adam, et al., *Nanotechnology*, 2009, **20**, 434005.

47 Y. Huang and D.-H. Kim, *Nanoscale*, 2011, **3**, 3228–3232.

48 O. Peña-Rodríguez, M. Crespillo, P. Díaz-Núñez, J. Perlado, A. Rivera and J. Olivares, *Opt. Mater. Express*, 2016, **6**, 734–742.

Supplementary Information: Elongation and plasmonic activity of embedded metal nanoparticles following heavy ion irradiation

Spyridon Korkos,[ab] Kai Arstila,[ab] Kosti Tapio,[b] Sami Kinnunen,[ab] J. Jussi Toppari,[b] and Timo Sajavaara[ab]

[a] Accelerator Laboratory, Department of Physics, University of Jyväskylä, P.O. Box 35, FI-40014 Jyvaskyla, Finland
[b] Nanoscience Center and Department of Physics, University of Jyväskylä, P.O. Box 35, FI-40014 Jyvaskyla, Finland

1 Polarization dependent dark-field measurements

Olympus BX51TRF microscope equipped with EOS 6D camera and coupled to Andor SP2150i spectrograph via a fiber (Thorlabs UM22-300-custom; core size, 300 μm) was used to measure the dark-field spectra [1, 2]. Andor IVAC DR-324-FI EMCCD camera was attached to the spectrograph and used to record the DF spectra. Olympus MPLANFL N 100x objective was utilized during the recording. IR-halogen lamp (100W, spectrum) was used to illuminate the samples in transmission mode. The microscope also included an analyzer (Olympus U-AN360-3) to filter the different light polarization coming from the sample.

Initially, the analyzer angle in respect to the optical camera view was calibrated: a thin metal wire was stretched and fixed on top of a polarizer (Thorlabs LPVISE200-A 2) and along the polarization axis of the polarizer. The polarizer was placed in the microscope and the wire was aligned along the vertical axis of the camera view. The analyzer was pushed in and we recorded the spectra originating from the polarizer while rotating the analyzer. The signal minimum (the perpendicular axis to the polarizer and the wire) and the maximum signal (the parallel axis to the polarizer) were noted and marked. We used these axes as the reference points, where the perpendicular axis was assigned as 0° and 180° due to 2-fold symmetry.

We removed the polarizer and placed a clean microscope slide in the microscope. The slide was washed first with detergent, then flushed with Milli-Q water and isopropanol, and finally dried using N_2 flow. A dark-field condenser (Olympus U-DCW) was placed underneath the slide and drop of oil was added to the condenser. The condenser and the slide were brought in contact so that there was thin oil layer between them. A small drop of oil was placed on top of the slide and excess oil was removed using a lens paper, until there was a thin layer of oil left. The sample was placed on top of the oil drop, so that the membrane window was touching the oil. If it seemed, that the sample was floating on top of the oil, we used a lens paper to remove oil around the sample, until the sample was immobile. During this process, reflected light (U-LH75XEAPO 75W Xenon lamp) was used to place the sample on the oil and this lamp was switched off during the measurements.

TEM reference images were used to find the correct window and the particles (Figure S1). The position of the fiber in the camera view was visualized by illuminating light from the spectrograph end using a green LED (Thorlabs M530L3). The polarization measurements were carried out by placing the fiber spot so that only the target particle was inside fiber spot, then the fiber was placed back to the spectrograph and desired polarization angle was selected (starting from the

angle 0°). The spectrum was recorded and we then selected an empty area next to the particle for the background (BG) measurements. The next polarization angle was selected and the spectra were recorded similarly for the particle and the background as before. This process was repeated for 0°, 45°, 90°, 135°, and 180° angles. After all the necessary particle spectra were recorded, we removed the sample and the condenser and recorded the lamp spectrum and the dark current (DC). The final particle intensity I was calculated from equation 1.

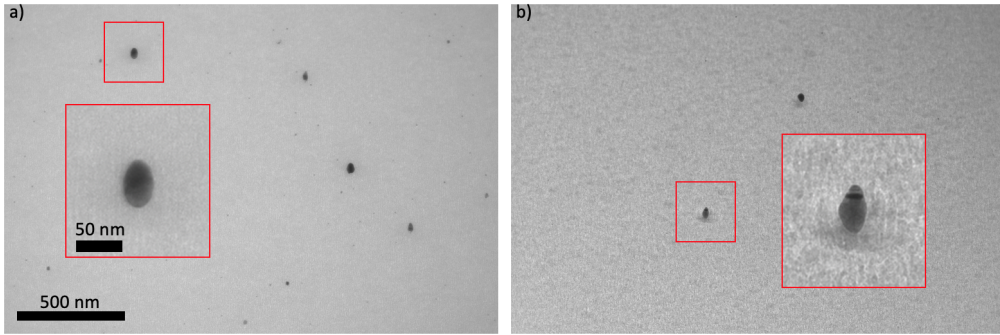$$I = \frac{I_{AuNP} - I_{BG}}{I_{lamp} - I_{DC}}. \tag{1}$$

Figure S1: TEM images of nanoparticles embedded in (a) Al_2O_3, where the inset image in big red outline is the magnified image of the same nanoparticle in small red outline and (b) SiO_2, where similar images as in a) are presented.

2 FDTD simulations of elongated and embedded gold nanoparticles

The finite-difference time domain (FDTD) simulations were performed using Lumerical FDTD Solutions software 2021 version 8.26.2834. The simulations were done in two-fold: the initial model with the air-medium-silicon nitride interface was utilized, which was compared to infinite medium approximation that was then used to simulate all the results. The schematic view of the initial model is shown in Figure S2. The dimensions of the gold nanoparticles were taken from the TEM images such as in Figure S1, where it was assumed that the elongated nanoparticles are

3

ellipsoids with two equal length short axes and one long axis. The refractive index (R.I.) of Au was taken from Johnson and Christy [3].

Initially, we considered the air-oil-medium-silicon nitride-air interface, where the particles are embedded in the medium (either silicon dioxide SiO_2 or aluminum oxide Al_2O_3). We ran the simulation with the initial model for the particle shown in Figure S2 (the solid green curve), which matched the measured LSPR peaks of the same particle (the dashed blue and yellow curves). Here, the refractive indexes of SiO_2 and Al_2O_3 were 1.52 and 1.66, respectively. We then assumed an infinite medium approximation and fitted the simulated LSPR peaks to the experimental ones by changing the R.I. of the new infinite medium. For SiO_2 and Al_2O_3, the new refractive indexes were 1.38 and 1.55, respectively, and the data fits the measured data and the initial model (the solid blue and yellow curves in Figure S2). Here, the interpretation is that the new refractive indexes are averaged, distance weighted values between air, medium and silicon nitride, so that the system can be simplified to an infinite medium approximation and the simulation can be performed faster. The simulation for other particles (see Figure 12 in the main article) shows that the simulated peaks fit the data using this approximation. A mesh of 1 nm was used around the particles and an overall mesh of 20 nm was defined throughout the rest of simulated area. The refractive index of air was 1.00027. Different polarization angles were initially considered, but since our ellipsoid has only two main LSPR modes (the short axis and the long axis) only two polarization directions were considered corresponding to these modes (Figure S3), since the other polarization directions were superpositions of these two modes.
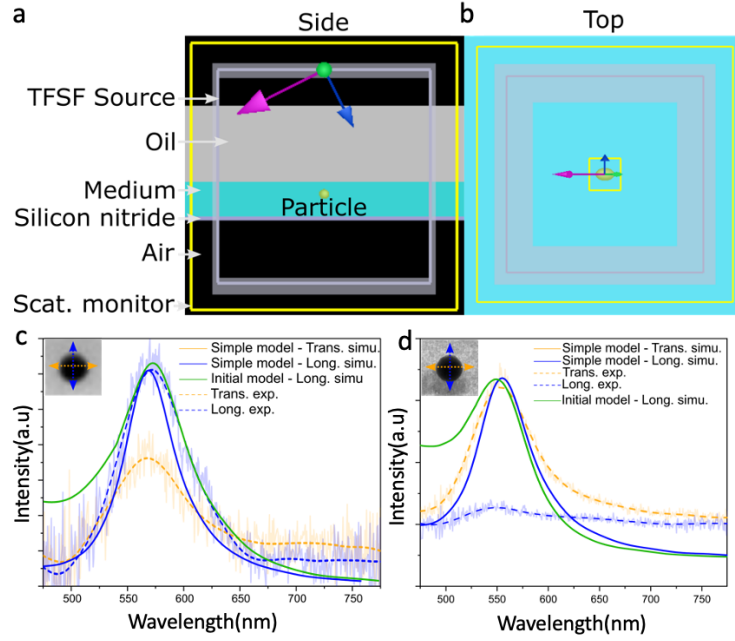
4

Figure S2: (a)-(b) The side and the top view of the initial FDTD model of the elongated and embedded particles in Al_2O_3 medium. (c) Comparison between the initial model and the simplified model for particle embedded in Al_2O_3. The solid green curve depicts the fit using the initial model, where as the solid blue and yellow curves depict the simplified model. The dashed curves show the corresponding measured data. (d) Comparison between the initial model and the simplified model for particle embedded in SiO_2. The solid green curve depicts the fit using the initial model, where as the solid blue and yellow curves depict the simplified model. The dashed curves show the corresponding measured data. The size of the TEM images is 110 nm×110 nm.
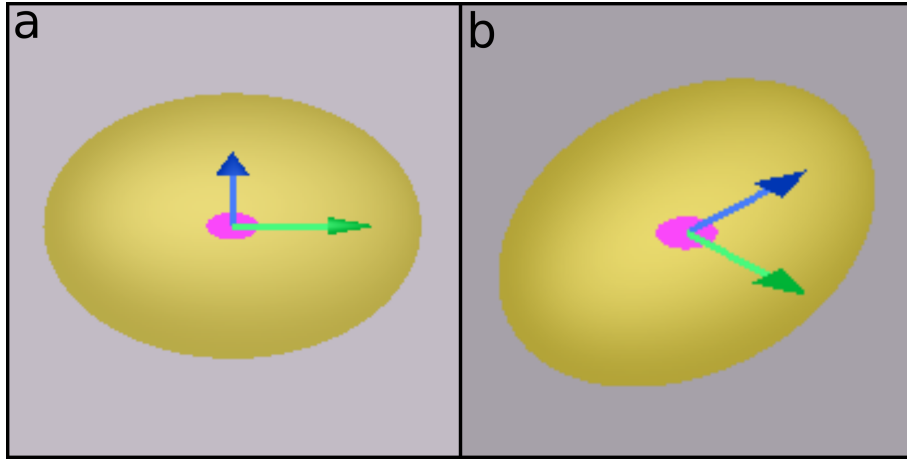
Figure S3: (a), (b) The two polarization angles considered in the simplified simulations.

References

[1] B. Shen, V. Linko, K. Tapio, S. Pikker, T. Lemma, A. Gopinath, K. V. Gothelf, M. A. Kostiainen and J. J. Toppari, *Science Advances*, 2018, **4**, eaap8978.

[2] K. Tapio, S. Dongkai, S. Auer, J. Tuppurainen, M. Ahlskog, V. Hytönen and J. Toppari, *Nanoscale*, 2018, **10**, 19297–19309.

[3] P. Johnson and R. Christy, *Physical Review B*, 1972, **6**, 4370–4379.